UNIVERSITY OF OKLAHOMA

GRADUATE COLLEGE

ANALYSIS OF THE DYNAMICS AND MICROPHYSICS OF A WET DOWNBURST CASE USING DUAL-POLARIZATION RADAR DATA

A DISSERTATION

SUBMITTED TO THE GRADUATE FACULTY

in partial fulfillment of the requirements for the

Degree of

DOCTOR OF PHILOSOPHY

By

VIVEK NARAYAN MAHALE
Norman, Oklahoma
2019

Downloaded from SHAREOK. Persistent Handle URL: https://hdl.handle.net/11244/319368

ANALYSIS OF THE DYNAMICS AND MICROPHYSICS OF A WET DOWNBURST CASE USING DUAL-POLARIZATION RADAR DATA

A DISSERTATION APPROVED FOR THE
SCHOOL OF METEOROLOGY

BY

Dr. Guifu Zhang, Chair

Dr. Ming Xue, Co-Chair

Dr. Howard Bluestein

Dr. Youngsun Jung

Dr. Yan Zhang

© Copyright by VIVEK NARAYAN MAHALE 2019
All Rights Reserved.

This dissertation is dedicated to my parents, Narayan and Hema Mahale, and brother, Dilip.

Your unwavering love and support have been vital to my success!

Acknowledgements

It was 25 years ago (25 April 1994) that I became interested in meteorology when a tornado went through my neighborhood in DeSoto, Texas. Ever since then, I've been fascinated by the weather. I feel incredibly fortunate that I was able to study severe storms as this dissertation is a culmination of nearly a lifetime of interest. Without the support of family, friends, teachers, professors, colleagues, administrative assistants, and others this achievement would not be possible!

First and foremost, I would like to thank my advisors, Drs. Guifu Zhang and Ming Xue, for their support during my doctoral research. Their commitment through the countless hours they spent on providing guidance, attending meetings, reviewing manuscripts, etc. cannot be overstated. I also appreciate their patience to work around my shiftwork at the National Weather Service (NWS). I also wish to thank my committee members Dr. Howard Bluestein, Dr. Youngsun Jung, Dr. Yan Zhang, and former member, Dr. Jerry Brotzge, for taking the time to serve on my committee. I am especially thankful for Drs. Howard Bluestein and Jerry Bortzge for serving as advisors during my master's degree. They set the foundation for my success in the doctoral program!

I am also grateful for Jeff Snyder and Andrew Pazmany for collecting the RaXPol data used in this dissertation. Jeff Snyder also provided technical assistance in the installation and use of radar analysis software. I am also appreciative of Robin Tanamachi for providing insight, photography, and video of the downburst event. Jidong Gao and Heather Reeves provided feedback to significantly improve the chapter on the variational retrieval method.

Also, thank you to the administrative assistants and staff of the School of Meteorology (SoM), Advanced Radar Research Center (ARRC), and Center for Analysis and Prediction of

Storms (CAPS) that have provided support over the last several years. Debbie Barnhill, Krysta Bruehl, Nancy Campbell, Debra Farmer, Eileen Hasselwander, Ashley Hill, Celia Jones, Jo Ann Mehl, Marcia Pallutto, Becky Steely, Christie Upchurch, and Lauren White all provided some assistance over the last several years.

I am appreciative of all my friends and colleagues that I met while at SoM. Several fellow (former) classmates are close friends, and I want thank all of them for their friendship through my undergraduate and/or graduate school career. Not only did we work hard to succeed in classes and research together, but we also had some awesome and memorable times outside of school. Daniel Betten, Tim Bonin, Brandon Lawson, Jim Kurdzo, Jennifer Newman, Bryan Putnam, Brett Roberts, Chris Schwarz, and Derek Stratman have all been great friends over the last several years! Other supportive colleagues are my former officemates: Jana Houser, Mike French, Dylan Reif, Kyle Thiem, and Zach Wienhoff.

I also appreciate the strong support I received from the NWS Norman, Oklahoma, management and staff. David Andra (MIC), Rick Smith (WCM), and Todd Lindley (SOO) have been supportive in my goal to finish my doctoral degree while working fulltime as a shift worker at the NWS. I am appreciative of my coworkers' flexibility to allow me to attend advisor meetings and conduct research during some quiet weather days. Marc Austin, Ryan Barnes, Randy Bowers, Kevin Brown, Scott Curl, Matthew Day, Jon Kurtz, Erin Maxwell, Forrest Mitchell, John Pike, Wayne Ruff, Michael Scotten, Cheryl Sharpe, Doug Speheger, Jennifer Thompson, Bruce Thoren, Phil Ware, and Alex Zwink have all been incredibly supportive colleagues! I also appreciate the strong support from Jami Boettcher, Mike Foster, Suzanne Jenkins, and Chris Sohl from my NWS family (some of whom have retired).

I would also like to thank professors and teachers in my past that provided the foundation necessary for me to be successful in my educational endeavors. Many of these individuals encouraged me to study meteorology because of my passion for it. It would be impossible for me to name every teacher, but Mike Carney and Bryan Yockers played an important role as my AP Environmental Science and AP Physics teachers at Jenks High School. They have both been extremely supportive from high school to the present. Mr. Carney even found me an opportunity to job shadow at the NWS in Tulsa, Oklahoma, my junior year of high school, which I am grateful for!

Finally, the love and support of my family has been unwavering and cannot be overstated. My parents, Narayan and Hema Mahale, and my brother, Dilip, have been supportive in many ways and it would be difficult to list everything they have done for me. The bottom line—without them, I would not be where I am today!

Financial support during the early part of this research came from NSF grant AGS-1046171, "Advanced Study of Precipitation Microphysics with Multi-frequency Polarimetric Radar Observations and Data Assimilation".

Substantial portions of this dissertation are from three of my lead-author publications that are either published, conditionally accepted, or in-preparation:

Mahale, V. N., G. Zhang, and M. Xue, 2016: Characterization of the 14 June 2011 Norman, Oklahoma, downburst through dual-polarization radar observations and hydrometeor classification. *J. Appl. Meteor. Clim.*, **55,** 2635–2655.

Mahale, V. N., G. Zhang, M. Xue, J. Gao, and H. D. Reeves, 2019: Variational retrieval of rain microphysics and related parameters from polarimetric radar data with a parameterized operator. *J. Atmos. Oceanic Technol.*, conditionally accepted.

Mahale, V. N., G. Zhang, M. Xue, H. B. Bluestein, and J. C. Snyder, 2019: Rapid-scan dual-polarization radar observations of the 14 June 2011 Norman, Oklahoma, downburst and associated gust front and rotor, in-preparation.[1]

The publication(s) that correspond to each chapter are acknowledged as a footnote at the beginning of each chapter. The publication in the *Journal of Applied Meteorology and Climatology* is © Copyright 2016 American Meteorological Society (AMS). Additional details (including the full copyright notice) are provided in the AMS Copyright Policy statement, available on the AMS website (http://www.ametsoc.org/CopyrightInformation). The AMS grants permission to use any portion of the author's work in works of the author's own, provided that the AMS citation and notice of the AMS copyright are included.

[1]Title and year for the publication is subject to change.

Table of Contents

Acknowledgements v

Table of Contents ix

List of Figures xii

Abstract xxi

Chapter 1 : Introduction 1

Chapter 2 : Review of Downbursts 4

2.1 Overview of Downbursts 4

2.2 Structure of Downbursts and Associated Features 6

2.3 Mechanisms Driving Downbursts 11

2.4 Radar Observations of Downbursts 16

2.5 Summary 19

Chapter 3 : Observation Tools 20

3.1 KOUN WSR-88D 20

3.2 KTLX WSR-88D 21

3.3 RaXPol 21

3.4 Mesonet 23

3.5 Observation Locations 24

Chapter 4 : Downburst Overview, Environment, and Surface Observations 25

4.1 Event Overview 25

4.2 Mesoscale and Thermodynamic Environment 27
4.3 1-Min Mesonet Observations of the Downburst 31
4.4 Quantitative Estimate of the Downward Acceleration Due to Buoyancy 36
Chapter 5 : WSR-88D Dual-Pol Observations, HCA, and Analysis 38
5.1 HCA Overview 38
5.2 Polarimetric radar observations and HCA 41
5.3 Dual-Doppler Analyses 53
5.4 Quantitative Estimate of Surface Mesohigh 55
5.5 Conceptual Model 56
5.6 Summary 59
Chapter 6 : RaXPol Dual-Pol Observations and Analysis 61
6.1 Horizontal Evolution and Structure of the Downburst 61
6.2 Vertical Structure and Evolution of the Downburst 71
6.3 Comparison to 1-min Mesonet Data 80
6.4 Summary 83
Chapter 7 : Dual-Frequency Comparison 86
7.1 S-Band and X-band Differences in PRD 86
7.2 Comparison PPI Scans 90
7.3 Comparison Methodology 91
7.4 Dual-Frequency Comparison 94

7.5 Summary 98

Chapter 8 : Variational Retrieval with a Parameterized Operator 99

8.1 Introduction to Observation-Based Retrievals 99

8.2. Derivation of Parameterized Polarimetric Radar Forward Observation Operators 101

8.3 Variational Retrieval Method 107

8.4 Variational Retrieval on Downburst Case 112

8.5. K_{DP} Calculated by Least-squares Fit vs. Analysis 117

8.6. Summary 118

Appendix: Testing the Variational Retrieval on DSD Data and Single Azimuth Radar Data 119

a. OI vs. Nonlinear 120

b. Nonlinear without Φ_{DP} vs. Nonlinear with Φ_{DP} 123

c. Simulated Observations 125

d. Summary of 2DVD Experiments 127

e. Single-azimuth Radar Experiment 127

Chapter 9 : Summary, Conclusions, and Future Work 132

9.1 Summary and Conclusions 132

9.2 Broader Impacts and Future Work 135

References 137

List of Figures

Fig. 2.1. A painting of a downburst based on Fujita's sketches of the downburst associated with the 1985 of Delta Flight 191 at the Dallas-Fort Worth (Texas) airport. From Fujita (1986). 4

Fig. 2.2. Schematic diagram illustrating the impact of a downburst on an aircraft's performance during takeoff. The aircraft first encounters a headwind during takeoff, which results in enhanced lift. This is followed by a decreasing headwind component, a downdraft, and finally a strong tailwind. Overcompensation during the period of enhanced lift may result in stalling and an impact with the ground. Composite drawing based on numerous studies of aircraft accidents by Fujita and Caracena (1977), Fujita and Byers (1977), and Fujita (1978, 1985, 1986). From (Wakimoto 2001). 5

Fig. 2.3. Three-dimensional visualization of a downburst. From Wakimoto (2001), which was adapted from Fujita (1985). 7

Fig. 2.4. A vertical cross section and horizontal view of the Delta Flight 191 microburst at 1806 CDT on August 2, 1985. This microburst, approximately 16,000' (3.5 km or 1.9 n.m.) in diameter, is characterized by three major Vortices 1, 2, and 3, which are surrounded by an older vortex encircling the overall microburst. From Fujita (1986). 8

Fig. 2.5. A sequence of photos showing the curling features of dust clouds (i.e., rotors or horizontal vortices) behind the leading edge of a microburst outflow on 15 July 1982 during the JAWS field operation. Photos by Brian Waranauskas. From Fujita (1985). 9

Fig. 2.6. Schematic of a vertical cross section through a mature thunderstorm outflow. From Droegemeier and Wilhelmson (1987); based on previous work from Charba (1974), Goff (1976), Wakimoto (1982), and Koch (1984). 10

Fig. 2.7. Results of a one-dimensional time dependent nonhydrostatic cloud model of a downdraft. Plotted numbers are vertical air velocity (m s^{-1}) at a level 3.7 km below the top of the downdraft (~850 hPa) as a function of the lapse rate in the environment and total liquid water mixing ratio at the top of the downdraft. Numbers on top scale indicate the radar reflectivity and rain rate at the top of the downdraft. Curved dotted line separates downbursts (<20 m s^{-1}) from less intense downdrafts. It was found that as the environmental lapse rate decreases (increases), higher (lower) water content is needed for a downburst. From Srivastava (1985)..... 15

Fig. 2.8. Horizontal radar reflectivity factor (Z_H) and radial velocity (V_R) from KOUN on 15 June 2011 at 0022 UTC. The characteristic low-level radial divergence signature associated with the downburst is seen. Plotted using GR2Analyst. 17

Fig. 2.9. Vertical cross section showing dual-polarization Doppler radar measurements obtained in a thunderstorm in northern Alabama during the MIST project. Note the presence of a Z_{DR} hole within the main precipitation core within a microburst-producing downdraft, which indicates the presence of melting hail. Reflectivity data are presented in contours of dBZ. Z_{DR} are shown in dB units. Arrow indicates location of the center of a surface microburst. From Wakimoto and Bringi (1988). 18

Fig. 3.1. Photo of RaXPol collecting data from the downburst in Norman, Oklahoma, on 14 June 2011. Note that the wet downburst is seen in the background. Photo courtesy Robin Tanamachi. 23

Fig. 3.2. Map of RaXPol, KOUN, and the Norman, Oklahoma, Mesonet locations during data collection. KOUN was located approximately 256 m to the southeast of RaXPol. The Norman Mesonet station was located approximately 221 m to the southwest of RaXPol. Plotted using Google Earth. 24

Fig. 4.1. Official storm reports and event narrative for the Norman, Oklahoma, downburst from the National Centers for Environmental Information (NCEI) Storm Events Database. The table abbreviations are: St. is state; T.Z. is time zone; Mag is magnitude; Dth is deaths; Inj is injuries; PrD is property damage estimate; and CrD is crop damage estimate. From NOAA/NCDC (2011). 26

Fig. 4.2. Map of wind damage reports (courtesy National Weather Service Norman, Oklahoma), (b) photo of the downburst from north Norman, and (c) photo of damage at Max Westheimer Airport. Photos courtesy Robin Tanamachi. 27

Fig. 4.3. Upper-air sounding and hodograph from Norman, Oklahoma (KOUN) at 0000 UTC 15 June 2011. Temperature is denoted by the red line and dew point by the green line. The purple line is the virtual temperature correction, and the turquoise line represents the parcel path for surface-based parcel. Plotted using The Universal Rawinsonde Observation (RAOB) program. 29

Fig. 4.4. KTLX radar reflectivity (dBZ) and Oklahoma Mesonet surface observations valid at (a) 2315, (b) 2345, and (c) 0005 UTC. Surface temperature (°C), dew point (°C), and wind barbs (full barb ≡ 5 m s^{-1}; half barb ≡ 2.5 m s^{-1}) are plotted. The white circle highlights the storm that would produce the downburst. The dashed blue line is the approximate location of the cold front. The location of the Norman and Minco Mesonet stations are indicated. Plotted using WeatherScope from the Oklahoma Climate Survey. 31

Fig. 4.5. 1-min Oklahoma Mesonet data at Norman, Oklahoma, of (a) surface pressure (hPa) and rain rate (mm hr^{-1}), (b) 2 m temperature (°C) and 2 m relative humidity (%), and (c) 10 m maximum wind gust (m s^{-1}) and wind direction (degrees) valid from 2330 to 0130 UTC. The

times of the gust front passage, downburst start, and downburst end are noted by the dashed lines. 33

Fig. 4.6. Time evolution of surface observations as the downburst passed over the Oklahoma Mesonet station at Norman, Oklahoma. Time relative maximum and minimum surface pressure are noted by “H” and “L”, respectively. Gust front passage is noted by cold front symbol. Schematic is based upon 1-min data from Figure 4.5. 36

Fig. 5.1. Reconstructed range height indicator (RHI) analyses from KOUN. Horizontal radar reflectivity factor (Z_H), co-polar correlation coefficient (ρ_{hv}), and differential reflectivity (Z_{DR}) are shown at (a) 2333-2337 UTC, (b) 2338-2342 UTC, (c) 2243-2347 UTC, and (d) 2348-2352 UTC volume scans. Axes are labeled relative to KOUN. RHI azimuth angle and noteworthy storm features are denoted. 43

Fig. 5.2. Reconstructed range height indicator (RHI) analyses from KOUN. Radial velocity (V_R) and hydrometeor classification algorithm (HCA) are shown at (a) 2333-2337 UTC, (b) 2338-2342 UTC, (c) 2243-2347 UTC, and (d) 2348-2352 UTC volume scans. The classifications on the right panel are: 1) ground clutter and anomalous propagation (GC/AP); 2) biological scatterers (BS); 3) dry aggregated snow (DS); 4) wet snow (WS); 5) crystals (CR); 6) graupel (GR); 7) big drops (BD); 8) light and moderate rain (RA); 9) heavy rain (HR); and 10) a mixture of rain and hail (RH). Axes are labeled relative to KOUN. RHI azimuth angle and noteworthy storm features are denoted. 44

Fig. 5.3. Same panels as Figure 5.1, but at (a) 2353-2357 UTC, (b) 2358-0002 UTC, (c) 0003-0007 UTC, and (d) 0008-0012 UTC volume scans. 46

Fig. 5.4. Same panels as Figure 5.2, but at (a) 2353-2357 UTC, (b) 2358-0002 UTC, (c) 0003-0007 UTC, and (d) 0008-0012 UTC volume scans. 47

Fig. 5.5. Same panels as Figure 5.1, but at (a) 0013-0017 UTC, (b) 0018-0022 UTC, and (c) 0023-0027 UTC volume scans..... 50

Fig. 5.6. Same panels as Figure 5.2, but at (a) 0013-0017 UTC, (b) 0018-0022 UTC, and (c) 0023-0027 UTC volume scans..... 51

Fig. 5.7. Dual-Doppler analysis at (a) 0018 UTC and (b) 0023 UTC with KOUN 1.45° radar reflectivity and hydrometeor classification algorithm (HCA). Dual-Doppler analysis includes horizontal velocity vectors and vertical velocity contours. Contours are plotted in 5 m s^{-1} intervals in white on the radar reflectivity panels and in black on the HCA panels. The location of Newcastle, Oklahoma, is indicated on panel (a). 54

Fig. 5.8. Schematics of the microphysical evolution of hydrometeors during the Norman, Oklahoma, downburst as observed by polarimetric radar data (PRD) and the applied hydrometeor classification algorithm (HCA). The schematics depict raindrops, snow, graupel, hail, and melting hail. Increasing water coating on the melting hailstones is depicted by the increasing line width of the hailstones. The 0 °C level is depicted by the dotted yellow line. Local Z_{DR} maxima (e.g., Z_{DR} columns) are depicted by the dashed red line. Local Z_{DR} minima are depicted by the dashed green line. The updraft and downburst locations are depicted by the green and blue arrows, respectively. Shaded blue region represents the cold pool. It is assumed that diabatic cooling from hail melting and rain evaporation plays an important role in accelerating the downdraft to result in a downburst. 58

Fig. 6.1. Horizontal radar reflectivity (Z_H; dBZ), radial velocity (V_R; m s^{-1}), and co-polar correlation coefficient (ρ_{hv}) at 3.0° elevation angle are shown at (a) 0018:50 UTC and (b) 0020:29 UTC. The dotted line (white on V_R; black on Z_H and ρ_{hv}) is the distance between the maximum inbound velocity on the southeastern part of the storm and the maximum outbound

velocity on the northern part of the storm. 1 km range rings and axes are labeled relative to RaXPol's location. 63

Fig. 6.2. Same panels as Figure 6.1, but 3.0° elevation angle at (a) 0022:07 UTC and (b) 0023:45 UTC..... 65

Fig. 6.3. 0023:45 UTC horizontal radar reflectivity (Z_H; dBZ), radial velocity (V_R; m s^{-1}), spectrum width (σ_v; m s^{-1}), differential reflectivity (Z_{DR}; dB), co-polar correlation coefficient (ρ_{hv}) and differential phase (ϕ_{DP}; degrees) at 3.0° elevation angle. Vertical vortices are circled in black. 1 km range rings and axes are labeled relative to RaXPol's location. 67

Fig. 6.4. Same panels as Figure 2, but 3.0° elevation angle at (a) 0025:23 UTC and (b) 0027:01 UTC..... 69

Fig. 6.5. The downburst's spatiotemporal evolution between 0020:29 and 0027:01 UTC. The downburst's horizontal scale is shown with respect to time and maximum inbound radial velocity (V_r). The downburst grew in horizontal scale from at least 2.1 km to 6.4 km in less than 7 min, changing based on size from a microburst to a macroburst while intensifying. 71

Fig. 6.6. Reconstructed range height indicator (RHI) from RaXPol at ~310° azimuth. Horizontal radar reflectivity (Z_H; dBZ), radial velocity (m s^{-1}), and co-polar correlation coefficient (ρ_{hv}) volume scans are shown at (a) 0018:50-0020:16 UTC and (b) 0020:29-0021:54 UTC. Axes are labeled relative to RaXPol's location. Noteworthy storm features are denoted. 73

Fig. 6.7. Same panels as Figure 6.5, but volume scans at (a) 0022:07-0023:32 UTC and (b) 0023:45-0025:10 UTC. 75

Fig. 6.8. Same panels as Figure 6.5, but volume scans at (a) 0025:23-0026:48 UTC, (b) 0027:01-0028:26 UTC, and (c) 0028:40-0030:05 UTC..... 78

Fig. 6.9. 1-min Oklahoma Mesonet data at Norman, Oklahoma, of (a) 10 m maximum wind gust (m s^{-1}) and wind direction (degrees) and (b) surface pressure (hPa) and 2 m temperature (°C) from 0016 to 0030 UTC. The times of the 3.0° elevation angle scans are noted (red dotted line). 81

Fig. 7.1. Attenuation (A_H: left column) and differential attenuation (A_{DP}: right column) versus specific differential phase for (a, b) S-band and (c, d) X-band. Modified from Zhang (2016). ... 87

Fig. 7.2. Backscattering phase differences (δ) as a function of raindrop size at S-band, C-band, and X-band frequencies. Modified from Zhang (2016). 87

Fig. 7.3. ρ_{hv} as a function of mass/volume-weighted diameter of wet hail and fractional water content (fw) at (a) S-band (b) X-band and (c) S-band – X-band. These were calculated using the T-matrix method assuming an exponential PSD and with the canting angle as a function of fw. 90

Fig. 7.4. Flow chart describing the post-processing for PRD for KOUN and RaXPol to conduct dual-frequency comparisons between the two radars. 92

Fig. 7.5. Example of post-processing of Z_H (dBZ) from a 5.3° elevation scan of KOUN WSR-88D data at 0020:08 UTC. (a) Pre-processed $Z_{H,}$ (b) Z_H after the application of a median filter, (c) Z_H after the application of a median filter and attenuation correction, (d) Z_H after the application of a median filter, attenuation correction, and advection correction, and (e) Z_H after the application of a median filter, attenuation correction, and advection correction interpolated to the RaXPol grid are shown. The grid spacing is 250 m x 1.1°. 94

Fig. 7.6. Example of post-processing of ρ_{hv} from a 5.0° elevation scan of RaXPol data at 0020:35 UTC. (a) Pre-processed ρ_{hv} and (b) ρ_{hv} downscaled from 75 m to 250 m range resolution. The grid spacing is 250 m x 1.1°. 94

Fig. 7.7. Difference fields of KOUN- RaXPol radar data for (a) Z_H, (b) Z_{DR}, and (c) ρ_{hv}. Difference fields are calculated from the 5.3° elevation scan of KOUN WSR-88D data at 0020:08 UTC and 5.0° elevation scan of RaXPol data at 0020:35 UTC. The grid spacing is 250 m x 1.1°. 95

Fig. 7.8. HCA applied to 5.3° elevation scan of KOUN WSR-88D data at 0020:08 UTC. 96

Fig. 7.9. HCA results from Figure 7.8 plotted as a function of S-band Z_H and ρ_{hv} difference between KOUN and RaXPol. 97

Fig. 8.1. The fitted parameterized polarimetric forward observation operators compared to direct calculations from T-matrix method for (a) Z_h, (b) Z_H, (c) Z_{dr}, (d) Z_{DR}, (e) K_{DP}, and (f) ρ_{hv}. These are normalized for W of 1 g m^{-3}. The equation on each panel is the derived observation operator. 106

Fig. 8.2. Block diagram of the iteration procedure for the nonlinear variational retrieval for a single azimuth of radar data. 112

Fig. 8.3. Analysis for (a) W and (b) D_m by applying the variational retrieval using a 5.3° elevation scan of KOUN WSR-88D data from 15 June 2011 at 0020 UTC. The boundaries of the sector with hail contamination are marked by the black lines. 113

Fig. 8.4. (a) Z_H observations, (b) Z_{DR} observations, (c) Z_H analysis, (d) Z_{DR} analysis, (e) Z_H observations and analysis difference, and (f) Z_{DR} observations and analysis difference using a 5.3° elevation scan of KOUN WSR-88D data from 15 June 2011 at 0020 UTC. The analyses are from applying the variational retrieval. 114

Fig. 8.5. K_{DP} (a) calculated using the slope of a least squares fit and (b) from the variational retrieval using a 5.3° elevation scan of KOUN WSR-88D data from 15 June 2011 at 0020 UTC. The left panel was calculated using GR2Analyst software. The boundaries of the sector with hail

contamination are marked by white lines on the left panel and black lines on the right panel. The area highlighted in yellow on the left panel is an area with some negative (unrealistic) K_{DP} values. 115

Fig. 8.6. HCA applied to 5.3° elevation scan of KOUN WSR-88D data from 15 June 2011 at 0020 UTC. The boundaries of the sector with hail contamination are marked by the black lines. 116

Fig. 8.7. OI analysis and nonlinear analysis compared to the truth for (a) W, (b) Z_H, (c) D_m, (d) $Z_{DR,}$ and (e) Φ_{DP} using 2DVD data collected on 2005 May 13. The constant background field for W and D_m are also shown. 122

Fig. 8.8. Same panels as Figure 8.7, but with nonlinear analysis without Φ_{DP} and nonlinear analysis with Φ_{DP} compared to the truth. 124

Fig. 8.9. Same panels as Figure 8.7, but with nonlinear analysis without error and nonlinear analysis with random error compared to the truth. The simulated observation (truth + random error) for Z_H, Z_{DR}, and Φ_{DP} are also shown. 126

Fig. 8.10. Analysis for (a) W, (b) Z_H, (c) D_m, (d) $Z_{DR,}$ and (e) Φ_{DP} by applying the variational retrieval on a single azimuth of 5.3° elevation scan of KOUN WSR-88D data from 15 June 2011 at 0020 UTC. The observed values for Z_H, $Z_{DR,}$ and Φ_{DP} are plotted for comparison. The empirical relationship and constant background field for W and D_m are shown as well. 129

Abstract

A significant, wet downburst affected Norman, Oklahoma, on 14 June 2011. Surface winds in excess of 35 m s^{-1} (>80 mph) and hailstones in excess of 4 cm diameter occurred during the downburst. The polarimetric S-band (~11.09-cm wavelength) KOUN Weather Surveillance Radar-1988 Doppler (WSR-88D) and the rapid-scan X-band (~3-cm wavelength) polarimetric, Doppler radar (RaXPol) collected nearly simultaneous polarimetric radar data (PRD) of the downburst.

The focus of this dissertation is the characterization and analysis of the dynamics and microphysics of the 14 June 2011 downburst and parent thunderstorm using various analysis methods. Analysis of the PRD from both KOUN and RaXPol radars are conducted using low-level plan position indicator (PPI) elevation scans and reconstructed range–height indicator (RHI) data. A hydrometeor classification algorithm (HCA) is applied to the KOUN PRD to understand the microphysical evolution of hydrometeors in the downburst. Dual-Doppler analysis is conducted with KOUN and the KTLX WSR-88D. Dual-frequency analysis and a comparison of the PRD are conducted between KOUN and RaXPol. Finally, a variational retrieval algorithm of rain microphysics is developed and applied to KOUN based on S-band parametrized polarimetric observation operators.

Through the above analyses, an understanding of the structure and evolution of the downburst and its potential driving mechanism(s) is developed. It is found that graupel aloft transitioned to nearly all rain and hail mixture above the 0 °C level. Eventually, this large area of rain and hail mixture (i.e., mixed-phase precipitation) descended to the ground with some melting of the hail, causing the downburst. The downburst grew from a microburst at ~2.1 km horizontal scale to a macroburst at ~6.4 km in less than 7 min. As the downburst expanded, its

near-surface horizontal winds intensified from 23 m s^{-1} to 42 m s^{-1}. Descending surges of mixed-phase precipitation cores aloft, indicated by a reduction in co-polar correlation coefficient (ρ_{hv}), provided a continued stream of precipitation loading and melting hail that may have aided in the continued expansion and intensity of the downburst. The unique, rapid-scan observations also captured the development of features such as a horizontal rotor, vertical vortices, multiple gust front heads, and an elevated nose on the leading edge of the gust front. The structure of the downburst is compared to the current conceptual model of a downburst and to 1-min Oklahoma Mesonet observations that were nearly collocated with the radar as well.

Chapter 1 : Introduction

The study of downbursts began with the mysterious crashes of aircraft that had no initial explanation (Wilson and Wakimoto 2001). One of these flights was Eastern Airlines Flight 66 that crashed while attempting to land at New York's John F. Kennedy (JFK) International Airport. The crash killed 112 and injured 12 people. Professor T. Theodore Fujita of the University of Chicago hypothesized that the flight had flown through a diverging wind system. He believed this weather phenomenon also caused the starburst damage patterns during the super outbreak of tornadoes on 3-4 April 1974. He coined the term *downburst* "to capture the notion of a strong downdraft of air that burst outward on contact with the ground" (Wilson and Wakimoto 2001). The significant impacts to aviation led to a period of heavy research—including field projects—on the downbursts in the 1970s and 1980s. This period of research set the foundation for our knowledge on downbursts today.

A significant, wet downburst affected Norman, Oklahoma, on 14 June 2011. A downburst is defined as a "strong downdraft which induces an outburst of damaging winds on or near the ground" (Fujita 1981, 1985). A wet downburst is a downburst where precipitation is measured at the surface (Fujita 1985). Surface winds in excess of 35 m s^{-1} (>80 mph) and hailstones in excess of 4 cm diameter occurred during the Norman downburst (NOAA/NCDC 2011). The focus of this dissertation is the characterization and analysis of the dynamics and microphysics of the aforementioned downburst using various observations and analysis methods. The polarimetric S-band (~11.09 cm) KOUN Weather Surveillance Radar-1988 Doppler (WSR-88D) and the rapid-scan X-band (~3-cm wavelength) polarimetric, Doppler radar (RaXPol) collected nearly simultaneous polarimetric radar data (PRD) of the downburst. In addition to the reflectivity at horizontal polarization (Z_H; hereafter reflectivity), radial velocity (V_R), and

spectrum width (σ_v), these dual-polarized (dual-pol) radars provide the polarimetric variables of differential reflectivity (Z_{DR}), co-polar correlation coefficient (ρ_{hv}), and differential phase (ϕ_{DP}). To my knowledge, RaXPol provided the most detailed and highest resolution polarimetric radar coverage during a wet downburst than any other event documented. Nearly collocated 1-min surface observations of the downburst were recorded by an Oklahoma Mesonet station, which further makes this study unique.

Several analysis methods are utilized in this dissertation, some of which have broader application beyond this study. Analysis of the radar observations from both the KOUN and RaXPol PRD are conducted using low-level plan position indicator (PPI) elevation scans and reconstructed range–height indicators (RHIs). A hydrometeor classification algorithm (HCA) is applied to the KOUN PRD to gain further understanding of the microphysical evolution of the hydrometeors in the downburst. Dual-Doppler analyses are conducted with KOUN and the KTLX WSR-88D. Dual-frequency analyses and comparison of the PRD are conducted with KOUN and RaXPol. Finally, a variational retrieval of rain microphysics from PRD has been developed through the use of S-band parametrized polarimetric observation operators. The variational retrieval has application beyond the scope of this dissertation by providing a method for the optimal retrieval of rain precipitation microphysics and a theoretical approach to find areas of mixed-phase precipitation by using scattering theory. Through these various analysis methods, an understanding on the potential driving mechanism(s) and the structure and evolution of the downburst is developed.

The organization of the dissertation is described as follows. Chapter 2 provides the background, context, and motivation of the study by reviewing our understanding of downbursts, including their structure, driving mechanisms, and radar observations. Aviation hazards

associated with downbursts are also discussed. Chapter 4 describes an overview of the Norman, Oklahoma, downburst event, including a broad summary of the event, the mesoscale and thermodynamic environment, and 1-min surface observations from the Oklahoma Mesonet. In Chapter 5, the microphysical evolution of the downburst is analyzed mostly through the use of RHIs from KOUN PRD and the application of an HCA. The horizontal and vertical spatiotemporal evolution and structure of the downburst and its associated gust front are analyzed using RaXPol PRD in Chapter 6. Dual-frequency analyses and comparison of the PRD from the two radars are shown in Chapter 7. Chapter 8 develops a variational method for microphysical retrieval. Finally, Chapter 9 summarizes the results and provides some thoughts on future work and broader applicability of this study.

Chapter 2 : Review of Downbursts[2]

The primary focus of this dissertation is the analysis and characterization of the dynamics and microphysics of a wet downburst case through the use of PRD. Therefore, it is appropriate to conduct a brief literature review on downbursts including an overview, their structure and associated features, their driving mechanisms, and radar observations.

2.1 Overview of Downbursts

The late Professor T. Theodore Fujita's seminal analyses on aircraft accidents and aerial damage surveys led to the discovery of the convective downburst. Fujita is known as "the person who was responsible for first proposing and eventually proving the existence of the downburst" (Wilson and Wakimoto 2001). Figure 2.1 is a visual depiction of a downburst that was created by using Fujita's hand-drawn sketches (Fujita 1986).



Fig. 2.1. A painting of a downburst based on Fujita's sketches of the downburst associated with the 1985 of Delta Flight 191 at the Dallas-Fort Worth (Texas) airport. From Fujita (1986).

[2]Adapted from: Mahale, V. N., G. Zhang, and M. Xue, 2016: Characterization of the 14 June 2011 Norman, Oklahoma, downburst through dual-polarization radar observations and hydrometeor classification. *J. Appl. Meteor. Clim.*, **55,** 2635–2655.
Mahale, V. N., G. Zhang, M. Xue, H. B. Bluestein, and J. C. Snyder, 2019: Rapid-scan dual-polarization radar observations of the 14 June 2011 Norman, Oklahoma, downburst and associated gust front and rotor, in-preparation. Title and year is subject to change.

Fujita (1981, 1985) defined a downburst as a "strong downdraft which induces an outburst of damaging winds on or near the ground." Downbursts are a significant hazard to aircraft, especially during landing and take offs due to rapid changes in lift (Fujita 1985, 1986; Fujita and Caracena 1977; National Transportation Safety Board 1983). Figure 2.2 is a schematic that describes the impact of a downburst on an aircraft during takeoff.

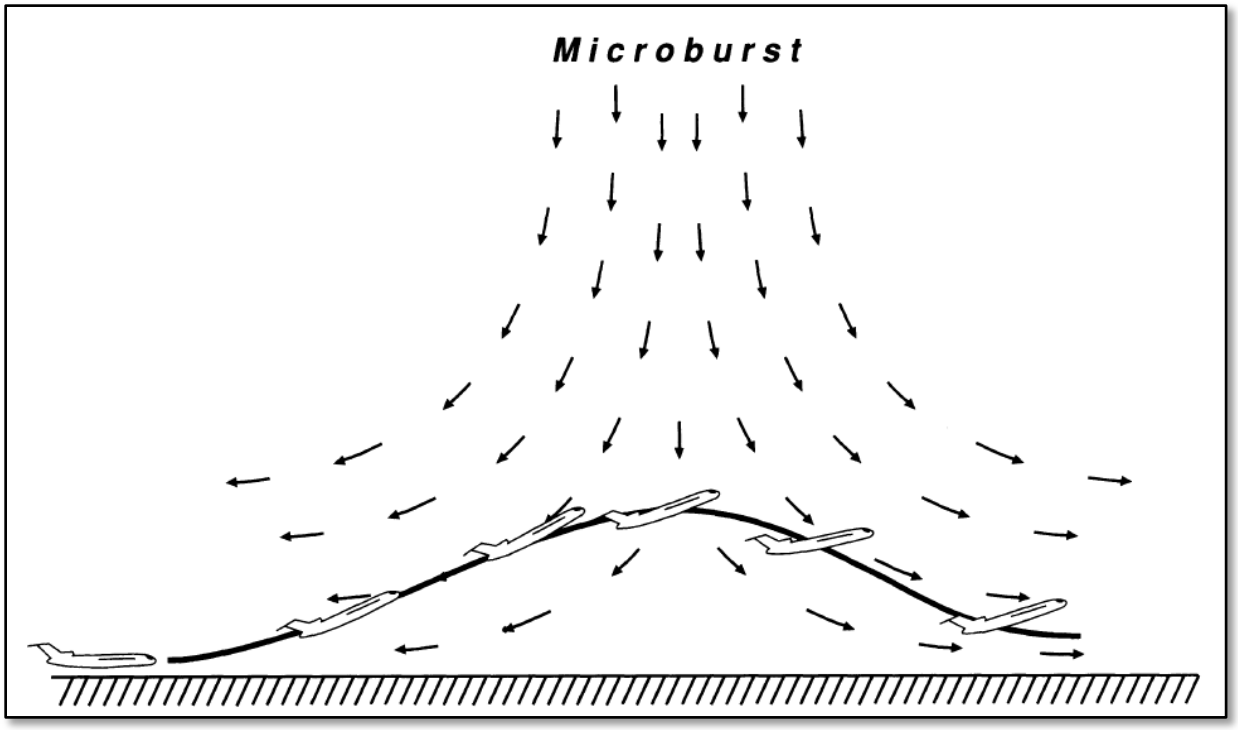


Fig. 2.2. Schematic diagram illustrating the impact of a downburst on an aircraft's performance during takeoff. The aircraft first encounters a headwind during takeoff, which results in enhanced lift. This is followed by a decreasing headwind component, a downdraft, and finally a strong tailwind. Overcompensation during the period of enhanced lift may result in stalling and an impact with the ground. Composite drawing based on numerous studies of aircraft accidents by Fujita and Caracena (1977), Fujita and Byers (1977), and Fujita (1978, 1985, 1986). From (Wakimoto 2001).

The structure and evolution of downbursts were studied through field projects and aerial surveys in the 1970s and 1980s. These field projects include the Northern Illinois Meteorological

Research on Downbursts (NIMROD) in 1978, the Joint Airport Weather Studies (JAWS) project in 1982, and the Microburst and Severe Thunderstorm (MIST) project in 1986.

Downbursts have been classified by the horizontal scale of their damaging winds and precipitation amount (e.g., Fujita 1985; Wakimoto 2001). A macroburst is a large downburst with outflow winds > 4 km in diameter and a microburst is a smaller downburst with winds ≤ 4 km in diameter; however, based on aerial surveys, Fujita and Wakimoto (1981) noted that a downburst in the meso-β scale (> 4 km) may be made up of one or more microbursts with even smaller "burst swaths" embedded inside a microburst. In other words, a downburst event on the macroburst scale could be due to one or more microbursts.

Fujita (1985) defined a wet downburst as a downburst where precipitation was measured at the surface. Other definitions found throughout the literature (e.g., Wakimoto 2001) are that dry/low-reflectivity downbursts have < 0.25 mm rainfall at the surface or a radar echo < 35 dBZ in intensity, and wet downbursts have > 0.25 mm rainfall at the surface or a radar echo > 35 dBZ intensity; wet downbursts may also have hail in addition to rain. The ambient environments and microphysical processes for dry and wet downbursts have been found to be different (e.g.,Wakimoto 2001); however, there can be some overlap between the dry and wet downburst ambient environments and microphysics (e.g., steep low-level lapse rates during a wet downburst). Downbursts that occur with overlapping characteristics sometimes are known as hybrid downbursts in the operational community (Warning Decision Training Division 2018).

2.2 Structure of Downbursts and Associated Features

Fujita (1985) summarizes much of the findings from NIMROD and JAWS, including a conceptual model of a downburst (Fig. 2.3). In this conceptual model, as the downflow (i.e.,

descending air in a downburst) reaches the surface, the attendant cold pool spreads out as a density current (e.g., Simpson 1969).

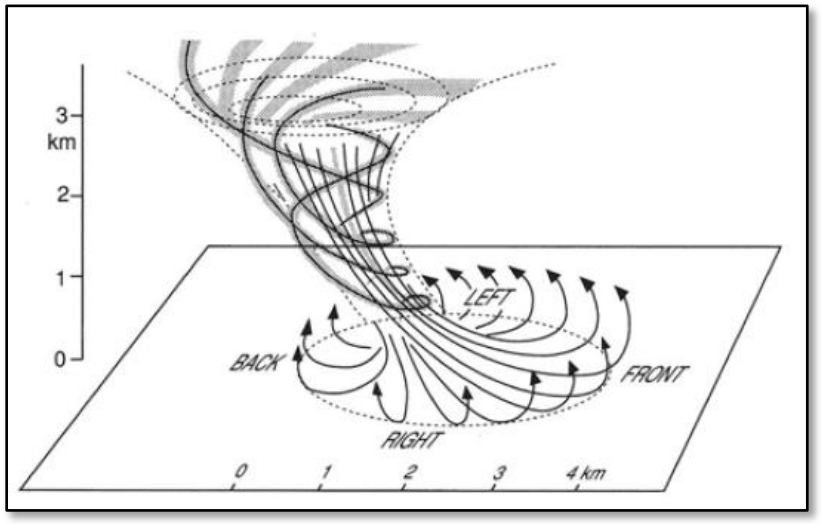


Fig. 2.3. Three-dimensional visualization of a downburst. From Wakimoto (2001), which was adapted from Fujita (1985).

The density current is forced outward by a pressure gradient force acting along it from the denser, colder side to the less dense, warmer side. The leading edge of this density current is associated with a narrow zone of wind shift and wind speed change that is called the gust front. Along the gust front, the baroclinic generation of horizontal vorticity due to the horizontal temperature gradient results in the generation of the horizontal rotor circulations (Rotunno et al. 1988). These rotors may develop aloft and descend to the surface or develop at the surface (Fujita 1986). When this horizontal vortex encircles the downflow center (i.e., a vortex ring), the outflow winds beneath the vortex ring are accelerated continuously as the ring expands and stretches (Fujita 1985). Some downbursts may have multiple vortex rings that surround the downflow region (Fig. 2.4; Fujita 1986).

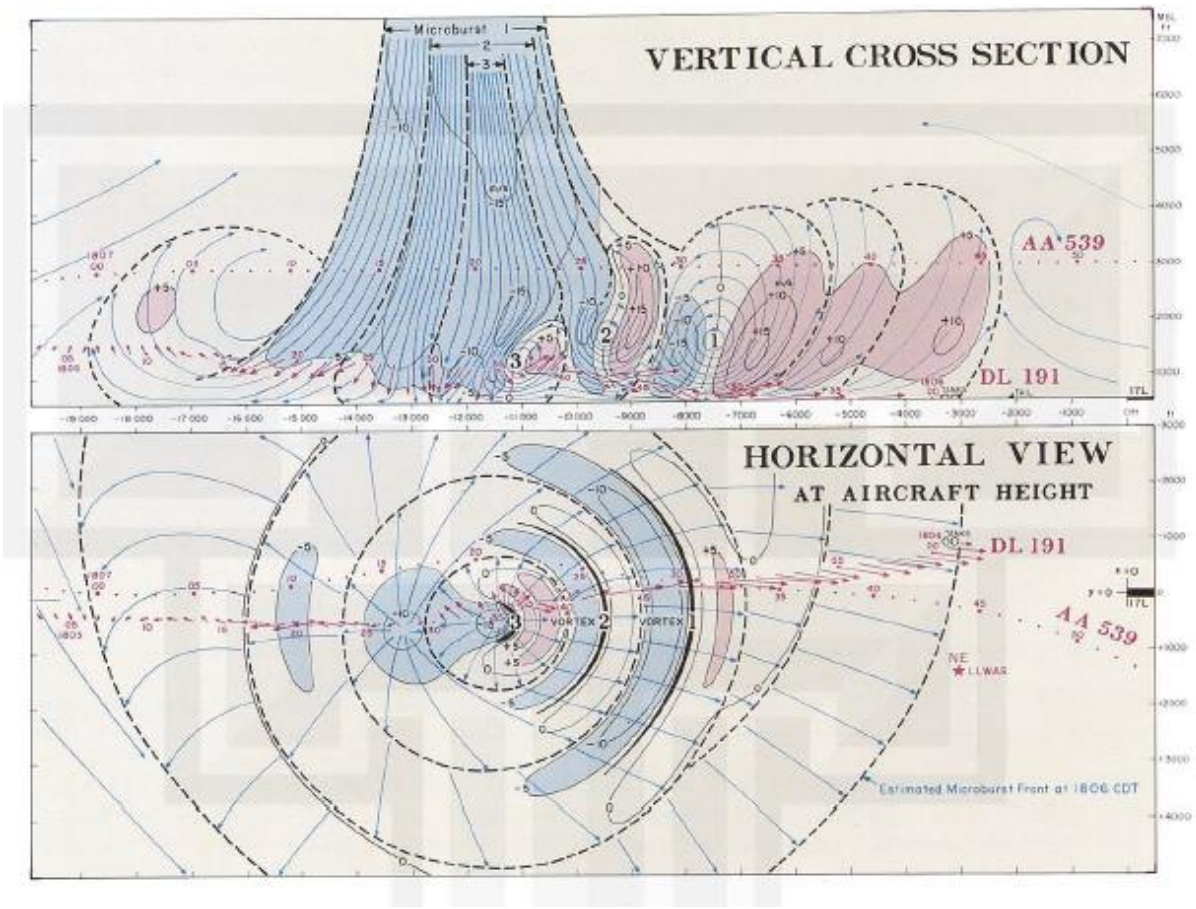


Fig. 2.4. A vertical cross section and horizontal view of the Delta Flight 191 microburst at 1806 CDT on August 2, 1985. This microburst, approximately 16,000' (3.5 km or 1.9 n.m.) in diameter, is characterized by three major Vortices 1, 2, and 3, which are surrounded by an older vortex encircling the overall microburst. From Fujita (1986).

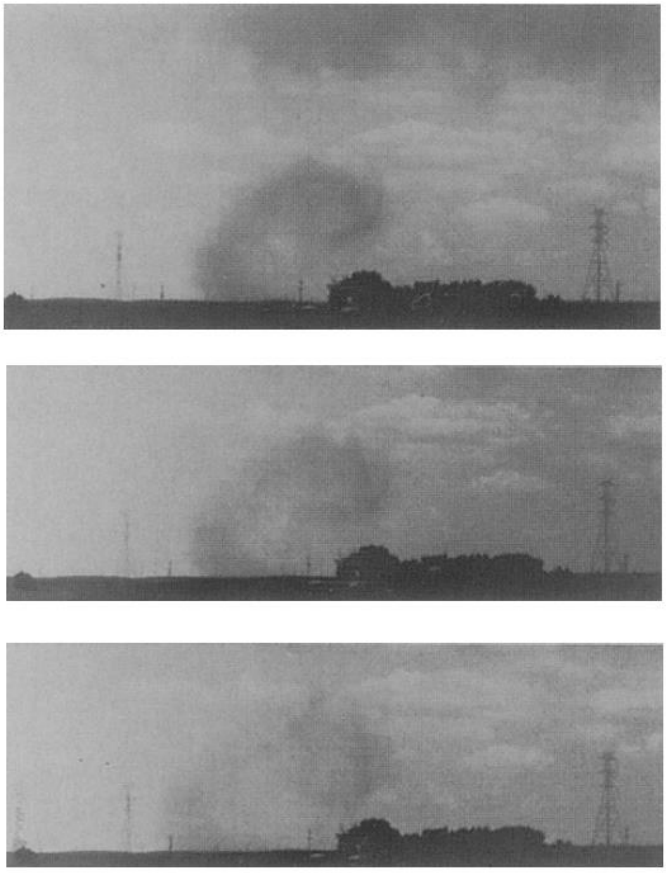


Fig. 2.5. A sequence of photos showing the curling features of dust clouds (i.e., rotors or horizontal vortices) behind the leading edge of a microburst outflow on 15 July 1982 during the JAWS field operation. Photos by Brian Waranauskas. From Fujita (1985).

Rotors or horizontal vortices have been shown to be present at the leading edge of cold outflows in both observations (e.g., Fujita 1985; Hjelmfelt 1988; Kessinger et al. 1988; Fig. 2.5) and model simulations (e.g., Droegemeier and Wilhelmson 1987). Figure 2.6 is a schematic cross section through the gust front of a thunderstorm from Droegemeier and Wilhelmson (1987). Some of these observations and model simulations indicate that rotors may contribute to the high surface winds associated with outflow in downbursts due to stretching of vorticity when the downburst increases in size. Rotors pose a significant risk to aviation. For example, rotors from a downburst may have contributed to the 1985 crash of Delta Flight 191 at the Dallas-Fort Worth

(Texas) airport (Fig. 2.4; Fujita 1986). This crash led the Federal Aviation Administration (FAA) to conduct a study on how dangerous, low-level wind shear could be detected by radar and resulted in funding for the C-band Terminal Doppler Weather Radar (TDWR) program (Whiton et al. 1998).

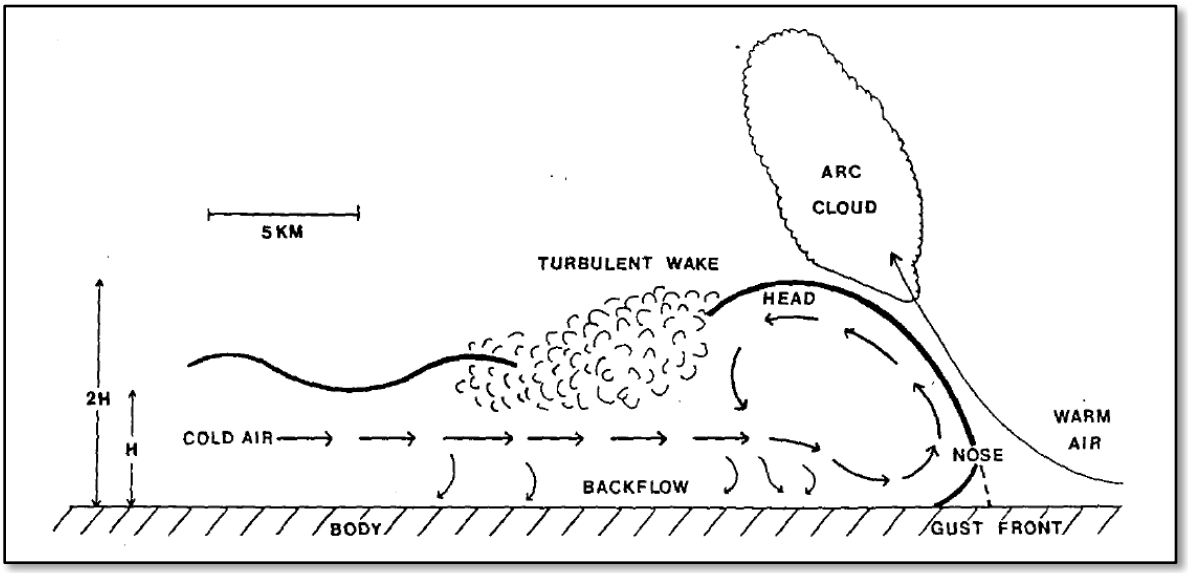


Fig. 2.6. Schematic of a vertical cross section through a mature thunderstorm outflow. From Droegemeier and Wilhelmson (1987); based on previous work from Charba (1974), Goff (1976), Wakimoto (1982), and Koch (1984).

Vertical vortices may develop along the leading edge of the gust front as well and may have the visual appearance of a giant dust devil or dusty tornado (e.g., Fujita 1985; Wakimoto and Wilson 1989). In numerical study by Lee and Wilhelmson (1997), they found that a vertical vortex sheet develops along the leading edge of an outflow boundary when there is a component of motion in the environment (ahead of the outflow boundary) parallel to the gust front. Essentially, the interaction of air masses creates a narrow transition zone of horizontal shear aligned along the leading edge of the convergence boundary/gust front. It is assumed that horizontal shearing instability is triggered (at least primarily) by lobe and cleft instability along

this vortex sheet by perturbations present at the gust front. Other possible triggers may include horizontal convective roll intersections with the outflow boundary, variations in the surface roughness, or variations in the outflow thermal field. Environmental horizontal vorticity tilted upward and stretched may also play a role. These vertical vortices can grow in size have an appearance and strength of a tornado and are sometimes known as "gustnadoes" (Doswell 1985); however, there is debate whether they should be classified as tornadoes because they are a "practically ubiquitous aspect of strong convective outflows" (Markowski and Dotzek 2010) and are often not strong enough to inflict damage.

2.3 Mechanisms Driving Downbursts

Downbursts, by definition, are associated with downward (negative) vertical motion. Therefore, the vertical equation of motion can be used to determine the mechanism (i.e., dynamics) that results in the downward motion (i.e., acceleration) in downbursts. Neglecting friction, the vertical component of the equation of motion is (Houze 2014):

$$\frac{Dw}{Dt} = -\frac{1}{\rho_o}\frac{\partial p^*}{\partial z} + B(\theta_v^*, p^*, q_H) \tag{2.1}$$

where $\frac{Dw}{Dt}$ is the total derivative of w (the vertical component of wind), z is vertical height, p is pressure, ρ is density, B is buoyancy, θ_v is the virtual potential temperature, and q_H is the mixing ratio of hydrometeors in the air (total mass of liquid water and/or ice per unit mass of air). In this form, the reference state is denoted by an "*o*" and the deviation from a hydrostatically balanced reference state (whose properties vary only with height) is denoted by an "*".

The first term on the right hand side of the equation, the acceleration due to a pressure-gradient, has been shown to not contribute to the downward motion in downbursts (Kessinger et al. 1988). This is intuitive because this term would produce an upward directed pressure-gradient

force acting against the downdraft because of a pressure maximum at the surface (Houze 2014). In other words, it acts to decelerate the vertical velocity as it approaches the surface. Therefore, the driving mechanism for downbursts reduces to the negative contributions due to buoyancy.

Buoyancy, *B*, is approximated by (Houze 2014):

$$B \approx g\left[\frac{\theta_v^*}{\theta_{v_o}} + (\kappa - 1)\frac{p^*}{p_o} - q_H\right] \tag{2.2}$$

where $\kappa = {R_d}/{c_p}$. R_d is the gas constant for dry air and c_p is the specific heat of dry air at constant pressure.

Virtual potential temperature, θ_v, is defined as the potential temperature that dry air would have if its pressure and density were equal to those of a given sample of moist air. It can be approximated by (Houze 2014):

$$\theta_v \approx \theta(1 + 0.61 q_v) \tag{2.3}$$

where θ is the potential temperature and q_v is the is the mixing ratio of water vapor in the air.

From the equation for buoyancy (2.2), it can be seen there are three factors that affect buoyancy (Wakimoto 2001): 1) thermal buoyancy, $\frac{\theta_v^*}{\theta_{v_o}}$; 2) perturbation pressure buoyancy, $(\kappa - 1)\frac{p^*}{p_o}$, and 3) condensate (precipitation) loading, q_H.

For the first term, the negative contribution to the thermal buoyancy term can be increased by phase changes and the associated absorption of latent heat (i.e., melting and/or evaporating) from hydrometeors (i.e., θ_v^* becomes more negative). Note that there will be a competing force of adiabatic warming with any downward motion. The temperature deficit for θ_v^* due to evaporation can be calculated by the following relationship (Wakimoto 2001):

$$\theta_v^* = -L\frac{q_r}{c_p} \tag{2.4}$$

where L is the latent heat of vaporization and q_r is the mixing ratio of rain water that has evaporated. A similar formulation may be used to calculate the temperature deficit for θ_v^* due to melting using the latent heat of fusion.

The second term indicates that an air parcel will accelerate upward if it is at a lower pressure than its surroundings (Wakimoto 2001). It has been primarily shown to counteract strong negative thermal buoyancy for overshooting tops (Schlesinger 1980). Otherwise, not much emphasis has been placed in studying its effects (Wakimoto 2001) and the assumption is it does not play a significant role in downbursts.

The third term indicates that the downward drag of precipitation will result in negative buoyancy through the force of gravity acting on the hydrometeors (i.e., precipitation loading). Therefore, it can be surmised that the primary driving mechanisms for the downward motion in downbursts (as deduced through the buoyancy term of the vertical equation of motion) are 1) thermal buoyancy through evaporation and/or melting of hydrometeors and 2) precipitation loading.

If the vertical motion in a downburst can be deduced from the vertical equation of motion (or through some other method such as dual-Doppler analysis), other dynamical quantities can be approximated. The maximum stagnation pressure perturbation, p_{max}^*, at the center of the downburst can be approximated by the following relationship based on Bernoulli's equation (Stull 2017):

$$p_{max}^* = \frac{1}{\rho_o}\left[\frac{w_d^2}{2} - \frac{g\theta_v^* z}{\theta_{v_o}}\right] \tag{2.5}$$

where w_d is the likely peak downburst speed at height z well above the ground.

There are two contributions to the increased pressure at the surface in a downburst. The first term is due to dynamics (i.e., pressure increase due to motion) and the second term due to

thermodynamics (i.e., pressure increase due to the added weight of cold air). Note that this equation assumes a steady-state process.

Using p^*_{max}, the change of outflow wind magnitude can be approximated using the horizontal pressure gradient force (Stull 2017):

$$\frac{\partial M}{\partial t} = \frac{1}{\rho_o}\frac{p^*_{max}}{r} \tag{2.6}$$

where *M* is the outflow wind magnitude and *r* is the radius of the downburst (assuming it roughly equals the radius of the mesohigh). In practice, this is usually an approximate (order of magnitude) value since the pressure gradient will vary in both space and time.

Assuming *r* is constant, the maximum wind speed at the surface (i.e., outflow winds) will increase as p^*_{max} increases. If *r* increases, p^*_{max} would have to increase further to compensate for the increase in *r*. Therefore, the maximum wind speed at the surface is controlled by p^*_{max} and the *r*. p^*_{max} is controlled by peak downburst speed and the temperature deficit in the mesohigh.

The previous assessment of the vertical equation of motion (2.1) and buoyancy (2.2) fit our current understanding on the initiation of downbursts from observation-based studies (e.g., Atlas et al. 2004; Wakimoto and Bringi 1988; Wakimoto et al. 1994) and from idealized numerical simulations (e.g., Proctor 1988, 1989; Srivastava 1985, 1987).

From these studies, it is understood that precipitation microphysical processes in a suitable ambient thermodynamic environment are important in producing downbursts. For dry downbursts, the sublimation of snowflake particles through a deep, dry adiabatic layer has shown to be effective in producing downbursts (Proctor 1989; Wakimoto et al. 1994). For wet downbursts, the ambient thermodynamic environment tends to be more humid and stable. In these situations, precipitation loading becomes more important for driving the initial downdraft

at mid-levels. As the environmental lapse rate decreases (increases), higher (lower) water content is needed for a downburst (Fig. 2.7; Srivastava 1985).

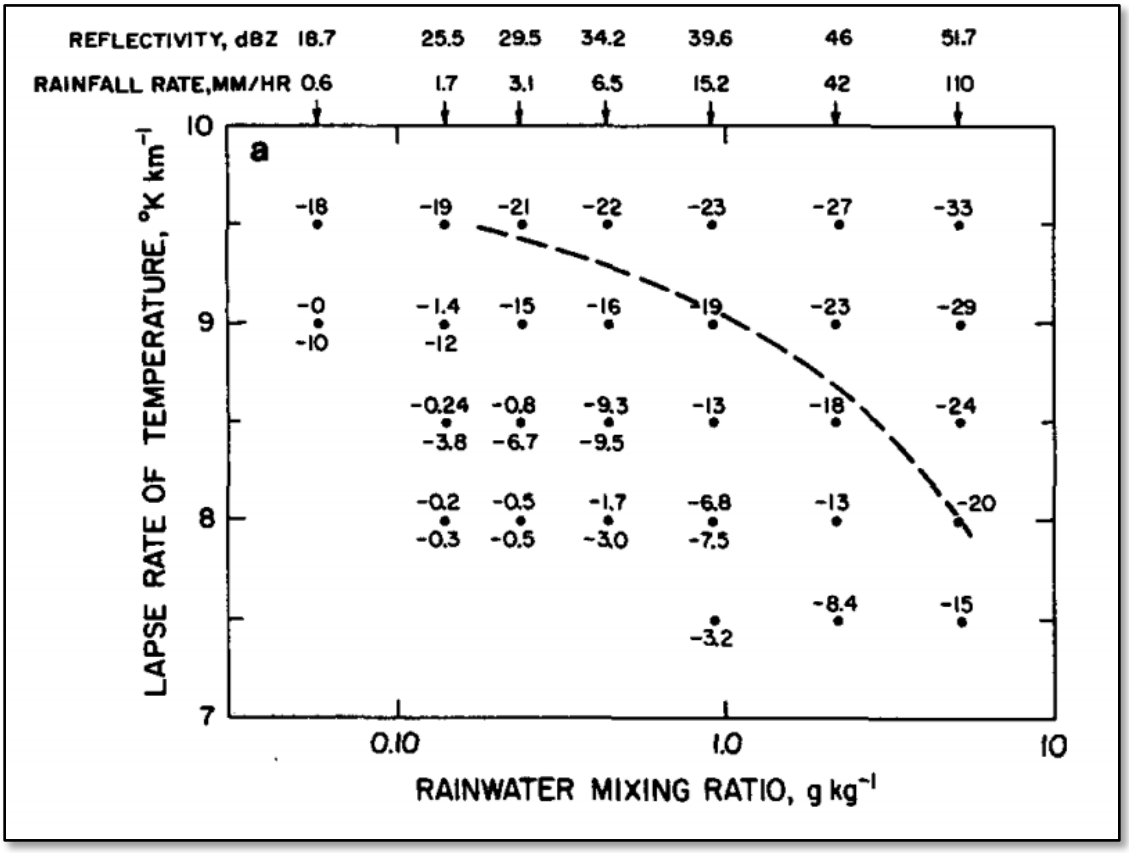


Fig. 2.7. Results of a one-dimensional time dependent nonhydrostatic cloud model of a downdraft. Plotted numbers are vertical air velocity (m s^{-1}) at a level 3.7 km below the top of the downdraft (~850 hPa) as a function of the lapse rate in the environment and total liquid water mixing ratio at the top of the downdraft. Numbers on top scale indicate the radar reflectivity and rain rate at the top of the downdraft. Curved dotted line separates downbursts (<20 m s^{-1}) from less intense downdrafts. It was found that as the environmental lapse rate decreases (increases), higher (lower) water content is needed for a downburst. From Srivastava (1985).

Observations and simulations also suggest that melting hailstones are important for wet downbursts (e.g., Atlas et al. 2004; Fu and Guo 2007; Proctor 1989; Srivastava 1987; Wakimoto and Bringi 1988). Fu and Guo (2007) simulated a downburst using a three-dimensional cloud

model that included hail-bin microphysics. They found that the downburst primarily was produced by hail-loading and was enhanced by cooling processes that were due to melting hailstones and the evaporation of raindrops. Proctor (1989) hypothesized that hail-loading is especially important in more stable environments because the cooling effect is delayed to lower elevations.

It has also been found that dry downbursts tend to have a small negative temperature perturbation (i.e., cooling) over a deep column. In contrast, wet downbursts tend to have a relatively larger, negative temperature perturbation over a shallower column near the surface (Proctor 1989). Proctor (1989) also found warming aloft with wet downbursts, indicating that precipitation loading is necessary to overcome positive temperature buoyancy.

It can be surmised from these studies that precipitation loading (including hail) is much more important for wet downbursts than dry downbursts. Though not explicitly stated yet, one can assume that if a wet downburst occurs in an environment that is favorable for dry downbursts (i.e. steep, low-level lapse rates), both phase changes and precipitation loading may have significant contributions to negative buoyancy.

2.4 Radar Observations of Downbursts

The characteristic radar signature associated with downbursts is a low-level radial divergence signature. Wilson et al. (1984) defined the diverging signature for a microburst having a velocity differential ≥ 10 m s^{-1} at an initial distance ≤ 4 km.

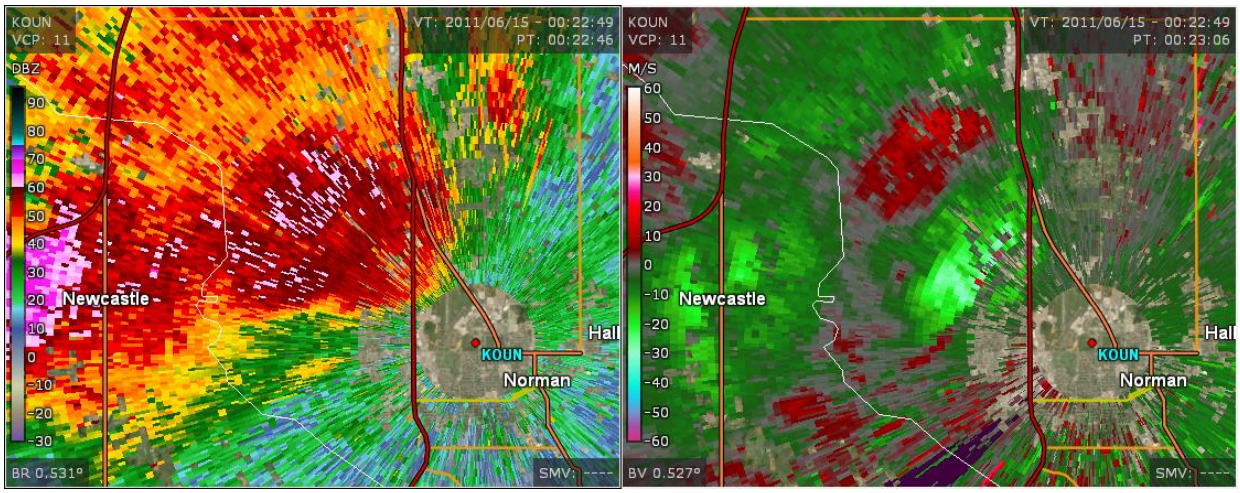


Fig. 2.8. Horizontal radar reflectivity factor (Z_H) and radial velocity (V_R) from KOUN on 15 June 2011 at 0022 UTC. The characteristic low-level radial divergence signature associated with the downburst is seen. Plotted using GR2Analyst.

While the low-level divergence signature is useful in the detection of an ongoing downburst, it does not provide any lead time. Prior to dual-pol radars, descending reflectivity cores (DRCs) were found to occur prior to downbursts (e.g., Roberts and Wilson 1989); however, it is difficult to deduce dominant hydrometeor types and microphysical properties with single-pol radars. There have been some studies that have utilized dual-pol radar observations for downbursts (e.g., Atlas et al. 2004; Kuster et al. 2016; Richter et al. 2014; Scharfenberg 2003; Suzuki et al. 2010; Tuttle et al. 1989; Wakimoto and Bringi 1988), which generally have found that melting hail and associated mixed-phase hydrometeors are an important aspect for downbursts due to cooling from melting and precipitation loading. This matches the findings from the simulations that were discussed previously in this chapter.

Wakimoto and Bringi (1988) found near-zero Z_{DR} surrounded by positive Z_{DR} in the main precipitation core within a microburst-producing downdraft, which they determined was associated with a strong downdraft composed of melting hail (Fig. 2.9). Scharfenberg (2003) and Suzuki et al. (2010) both noted reduced ρ_{hv} in the descending core. The ρ_{hv} reduction was

attributed to mixed-phase hydrometeors (i.e., mixture of rain and hail) in the downburst. From these studies, it is clear the advantage of dual-pol radars when studying downbursts is a better understanding of hydrometeor evolution and associated microphysical properties.

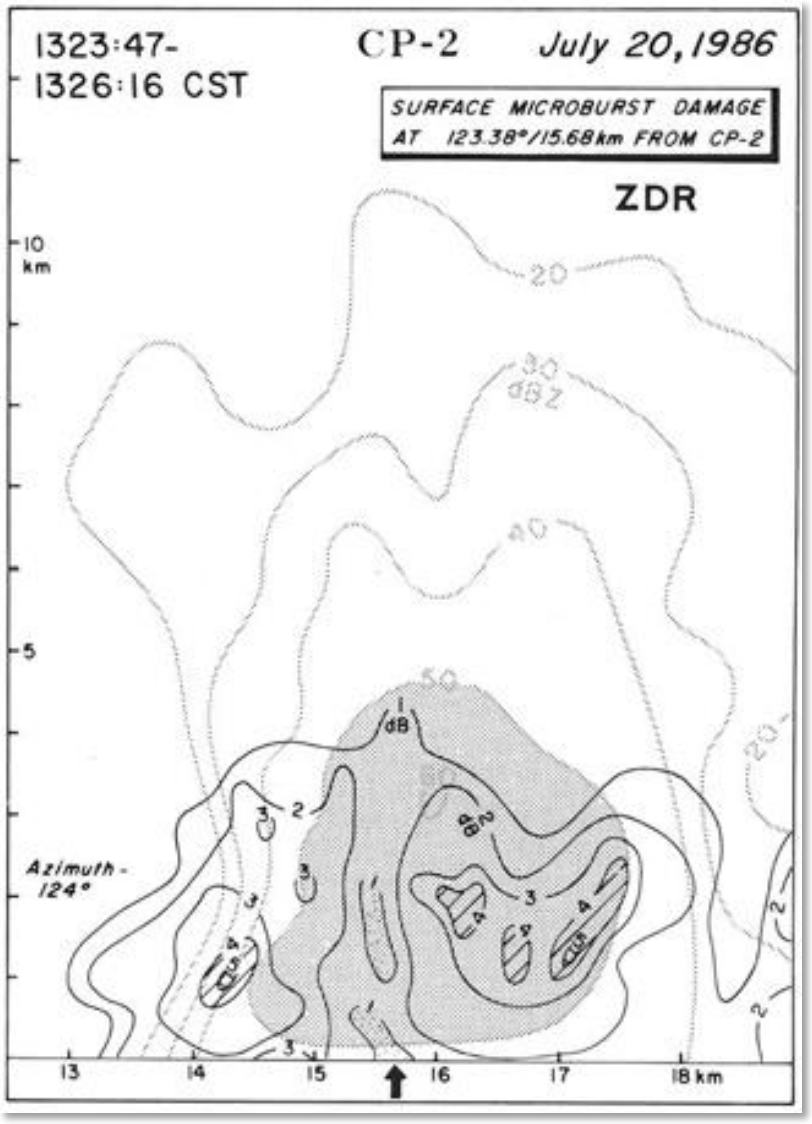


Fig. 2.9. Vertical cross section showing dual-polarization Doppler radar measurements obtained in a thunderstorm in northern Alabama during the MIST project. Note the presence of a Z_{DR} hole within the main precipitation core within a microburst-producing downdraft, which indicates the presence of melting hail. Reflectivity data are presented in contours of dBZ. Z_{DR} are shown in dB units. Arrow indicates location of the center of a surface microburst. From Wakimoto and Bringi (1988).

2.5 Summary

Overall, a downburst occurs when an intense downdraft reaches the surface and the attendant cold pool spreads out as a density current. The primary driving mechanisms for the downward motion in downbursts are 1) thermal buoyancy through evaporation and/or melting of hydrometeors and 2) precipitation loading. Unsurprisingly, precipitation loading (including melting hail) is much more important for wet downbursts than dry downbursts. PRD have been utilized in some downbursts studies, which have shown the importance of melting hail in downbursts.

The maximum wind speed at the surface is controlled by horizontal pressure gradient force at the surface (i.e., the maximum pressure perturbation and radius of the downburst). As shown by Bernoulli's equation, the maximum pressure perturbation at the surface is determined by peak downburst speed and the temperature deficit in the mesohigh. The peak downburst speed is controlled by the previously mentioned driving mechanisms for downward motion.

The aforementioned summary on downbursts serves as motivation for this study. It is evident that the hydrometeor evolution and associated microphysical processes within the parent thunderstorm is important in the dynamics of downbursts. By using PRD, a better understanding of the microphysical evolution of precipitation is possible.

Chapter 3 : Observation Tools

The primary observation tools used in this study include S-band radars, a mobile X-band radar, and a 1-min surface observation station. Details on the radars and the surface station are provided in this chapter.

3.1 KOUN WSR-88D

The KOUN S-band (~11.09 cm) WSR-88D radar, located in Norman, Oklahoma, collected polarimetric radar observations of the downburst and its parent thunderstorm. The National Weather Service (NWS) installed the prototype dual-pol upgrade for the WSR-88D radars on the KOUN radar (Saxion and Ice 2012). It is maintained by the National Severe Storms Laboratory (NSSL).

KOUN was scanning with Volume Coverage Pattern (VCP) 11, which was a VCP frequently used for severe thunderstorms in the past (Office of the Federal Coordinator for Meteorological Services and Supporting Research 2016). In this scanning strategy, each volume scan takes approximately five minutes and includes 360° plan position indicator (PPI) scans (i.e., conical scans) collected at 14 different elevations. The PPI scans are taken at approximately 0.5°, 1.5°, 2.4°, 3.4°, 4.3°, 5.3°, 6.2°, 7.5°, 8.7°, 10.0°, 12.0°, 14.0°, 16.7°, and 19.5° elevation angles.

The radial sampling resolution was 250 m and azimuth increment was 0.5° for the lowest two elevation scans (0.5° and 1.5°). The two lowest elevation angles are split cut elevations, where there is a low PRF contiguous surveillance (CS) and high PRF contiguous Doppler (CD) scan. Reflectivity and PRD are processed from the CS scan. At higher elevations, the azimuth increment is 1.0°. Radar data were manually dealiased using the National Center for Atmospheric Research (NCAR) Earth Observing Laboratory's (EOL) solo3 software package.

The KOUN radar was within 5 km of the downburst, providing excellent resolution and low-level coverage for this event. However, because the highest elevation PPI was at 19.5°, a limitation is the storm top was not sampled due to the radar cone of silence. As the storm approached the radar, less of the storm was sampled aloft. KOUN WSR-88D radar data were obtained from the National Climatic Data Center (NCDC 2011a).

3.2 KTLX WSR-88D

The KTLX S-band WSR-88D radar, located in Norman, Oklahoma, also collected radar observations of the downburst and its parent thunderstorm. In 2011, KTLX had not yet been upgraded to dual-pol; otherwise, its radar characteristics are similar to KOUN. KTLX was located ~20 km to the northeast of KOUN and provided limited dual-Doppler coverage. Dual-Doppler coverage was limited because the between-beam angle was small for much of the thunderstorm's life cycle. KTLX WSR-88D radar data were obtained from the NCDC (NCDC 2011a).

3.3 RaXPol

RaXPol (Fig. 1; Pazmany et al. 2013) collected high spatiotemporal resolution of the downburst and its associated gust front and rotor within close range. Data were collected by Jeff Snyder and Andrew Pazmany. RaXPol has a 2.4-m-diameter dual-pol parabolic dish antenna on a high-speed pedestal. The 20-kW transmitter can generate pulse compression and frequency-hopping waveforms. Frequency hopping allows for more independent samples when compared to no frequency hopping, which allows RaXPol to scan much more rapidly than conventional radars. Pazmany et al. (2013) contains more technical details on RaXPol and its radar system.

For this event, one 360° PPI elevation scan took ~6-7 sec with elevation scans every 2° from 1.0° to 27.0°. An entire volume scan took ~1 min and 40 sec. Note for this event and others collected in 2011 (Houser et al. 2015; Pazmany et al. 2013) the RaXPol data on the lowest elevation scan were actually data collected during the downward spiral from the previous higher elevation scan (this was the first year RaXPol was used). Therefore, the 1.0° elevation scan is not useful for analysis or reconstructed RHIs (i.e., the lowest scan with no data quality issues is 3.0°).

The radial sampling resolution was 75 m and azimuth increment was ~1.1°. The Nyquist velocity was 30.8 m s^{-1}. As with the WSR-88D data, radar data were manually dealiased using the NCAR EOL's solo3 software package. Data where the SNR were less than 5 dB were removed.

As with the WSR-88D, the downburst and its intense winds were moving toward and directly impacted the radar. The RaXPol data collection began later in the thunderstorm's life cycle when compared to the WSR-88D data. Therefore, less of the storm was sampled aloft when compared to the WSR-88D data.



Fig. 3.1. Photo of RaXPol collecting data from the downburst in Norman, Oklahoma, on 14 June 2011. Note that the wet downburst is seen in the background. Photo courtesy Robin Tanamachi.

3.4 Mesonet

Surface observations were provided by the Oklahoma Mesonet, which is maintained by the Oklahoma Climatological Survey (Oklahoma Climate Survey 2011). The Oklahoma Mesonet (Brock et al. 1995; McPherson et al. 2007) is a network of over 100 automated weather stations covering Oklahoma. There is a Mesonet station in Norman, Oklahoma, nearly collocated with the KOUN radar. The Mesonet station recorded 1-min data from the downburst. The data collected include temperature and relative humidity at 2 m, wind speed and direction at 10 m, station atmospheric pressure, and tipping-bucket precipitation. One tip is equivalent to 0.254 mm

of rainfall. The 10-m maximum wind speed (i.e., wind gust) is the highest 3 s sample within the 1-min interval. The unique 1-min temporal resolution provides highly detailed information about the surface conditions beneath the downburst.

3.5 Observation Locations

During the data collection, KOUN was located approximately 256 m to the southeast of RaXPol. The Norman Mesonet station was located approximately 221 m to the southwest of RaXPol. For practical purposes, these are considered nearly collocated. Figure 3.2 is a map with the locations of these three observation sources. Note that KTLX is not shown on this map.

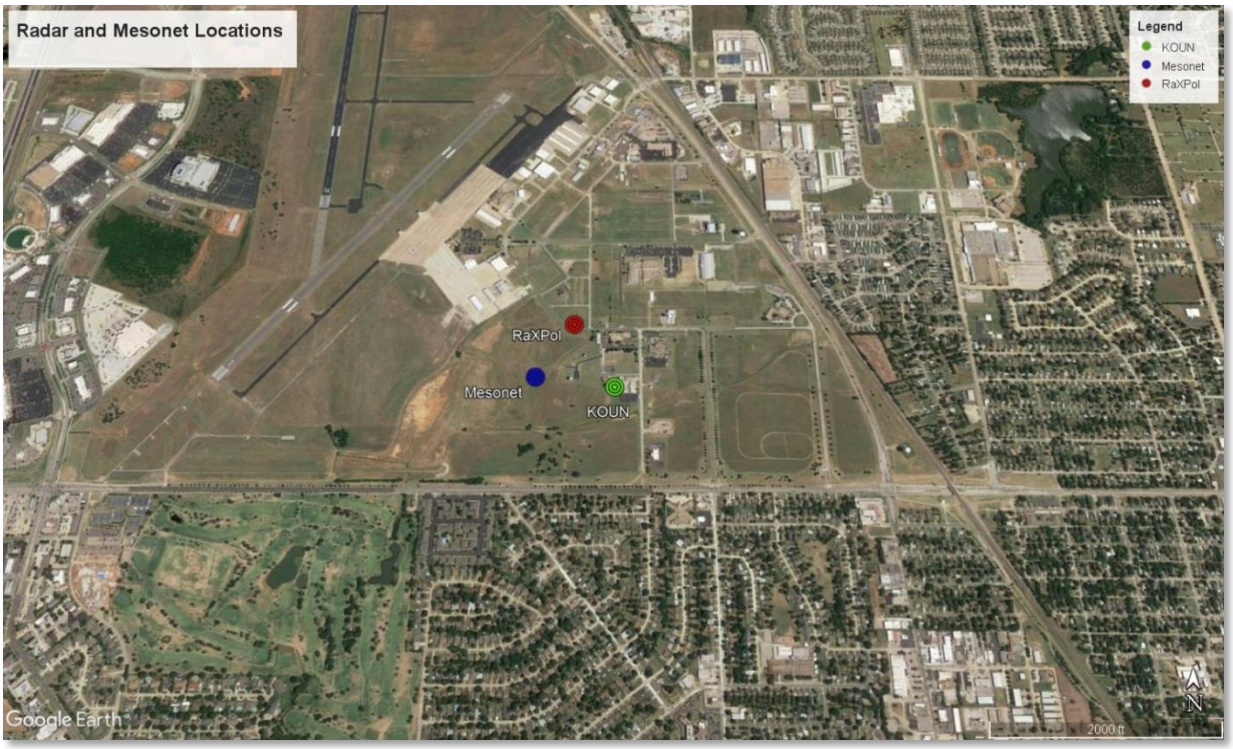


Fig. 3.2. Map of RaXPol, KOUN, and the Norman, Oklahoma, Mesonet locations during data collection. KOUN was located approximately 256 m to the southeast of RaXPol. The Norman Mesonet station was located approximately 221 m to the southwest of RaXPol. Plotted using Google Earth.

Chapter 4 : Downburst Overview, Environment, and Surface Observations[3]

An event overview of the 14 June 2011 Norman, Oklahoma, downburst is provided in this chapter. This includes an overview of damage reports, the mesoscale and thermodynamic environment, and 1-min Oklahoma Mesonet surface observations.

4.1 Event Overview

The downburst affected Norman, Oklahoma, in the early evening between 7:29 to 7:50 pm CDT (0029 to 0050 UTC) on 14 June 2011 (15 June 2011 UTC). Surface winds in excess of 35 m s^{-1} (>80 mph) and hailstones in excess of 4 cm diameter were reported from the storm in Norman, Oklahoma (Fig. 4.1; NOAA/NCDC 2011). The maximum wind gust measured was 36.7 m s^{-1} in southeast Norman, and the largest hailstone reported was 4.4 cm. The maximum wind gust may have been underestimated because the anemometer recorded the 36.7 m s^{-1} before malfunctioning due to windblown hail. As a result of the downburst, widespread wind damage occurred across Norman (Fig. 4.2a), including at Max Westheimer Airport (Fig 4.2b,c). Numerous power lines were snapped and over 33,000 residents of Norman lost power; some residents lost power for over 24 hours. Nearly horizontal, windblown hailstones damaged automobiles, house siding, and store signs. Figure 4.1 is a summary of the official NWS storm reports and episode narrative associated with the downburst. The area of damage from the downburst was over 4 km in length; therefore, the downburst can be classified a macroburst by size.

[3]Adapted from: Mahale, V. N., G. Zhang, and M. Xue, 2016: Characterization of the 14 June 2011 Norman, Oklahoma, downburst through dual-polarization radar observations and hydrometeor classification. *J. Appl. Meteor. Clim.*, **55,** 2635–2655.

Location	County/Zone	St.	Date	Time	T.Z.	Type	Mag	Dth	Inj	PrD	CrD
Totals:								0	0	11.00K	0.00K
(OUN)NORMAN WESTHEIMER ARPT	CLEVELAND CO.	OK	06/14/2011	18:23	CST-6	Hail	1.75 in.	0	0	0.00K	0.00K
(OUN)NORMAN WESTHEIMER ARPT	CLEVELAND CO.	OK	06/14/2011	18:28	CST-6	Thunderstorm Wind	61 kts. MG	0	0	0.00K	0.00K
NORMAN	CLEVELAND CO.	OK	06/14/2011	18:30	CST-6	Hail	1.75 in.	0	0	0.00K	0.00K
NORMAN	CLEVELAND CO.	OK	06/14/2011	18:30	CST-6	Hail	1.75 in.	0	0	0.00K	0.00K
(OUN)NORMAN WESTHEIMER ARPT	CLEVELAND CO.	OK	06/14/2011	18:30	CST-6	Thunderstorm Wind	61 kts. MG	0	0	0.00K	0.00K
(OUN)NORMAN WESTHEIMER ARPT	CLEVELAND CO.	OK	06/14/2011	18:30	CST-6	Thunderstorm Wind	65 kts. EG	0	0	10.00K	0.00K
NORMAN	CLEVELAND CO.	OK	06/14/2011	18:37	CST-6	Thunderstorm Wind	57 kts. MG	0	0	0.00K	0.00K
NORMAN	CLEVELAND CO.	OK	06/14/2011	18:37	CST-6	Thunderstorm Wind	61 kts. EG	0	0	0.00K	0.00K
NORMAN	CLEVELAND CO.	OK	06/14/2011	18:40	CST-6	Thunderstorm Wind	71 kts. MG	0	0	0.00K	0.00K
NORMAN	CLEVELAND CO.	OK	06/14/2011	18:40	CST-6	Thunderstorm Wind	61 kts. EG	0	0	1.00K	0.00K
NORMAN	CLEVELAND CO.	OK	06/14/2011	18:40	CST-6	Hail	1.50 in.	0	0	0.00K	0.00K
NORMAN	CLEVELAND CO.	OK	06/14/2011	19:50	CST-6	Hail	1.00 in.	0	0	0.00K	0.00K
Totals:								0	0	11.00K	0.00K

Episode Narrative	A cold front made its way southeast through Oklahoma during the day, lying over the northwest half of the state by late afternoon. A humid airmass was in place, with plenty of instability from which thunderstorms could work with. Temperatures ahead of the front were well into the 90s to a few degrees above 100 degrees. The large surface temperature and dew point spreads at the surface made the downburst wind threat very high. Also, with the aide of a stronger mid-level flow and cooling, large hail was also a threat. Thunderstorms developed over southwest Oklahoma by late afternoon/early evening. Other thunderstorms began developing over central Oklahoma. The two areas of thunderstorms merged into a line of severe storms, and even extended a little further northeast, with large hail and damaging winds reported through almost the entire complex. The most damaging storm occurred over central Oklahoma, specifically near Norman and Oklahoma City. Shortly after 7 pm, a wet downburst caused intense rainfall and was accompanied by hail up to golf-ball size and winds that were measured at over 80 mph. Damage was reported over much of Norman, with the most intense damage occurring over the northern half of the city. Almost 33,000 residents were without power, some still without power over 24 hours later. This was due to the numerous power poles/lines that were snapped or blown down. The hail was blown almost horizontally, damaging siding, shattering store signs, and denting automobiles. The highest measured wind gust occurred near SE 12th and Boyd, where the anemometer recorded 82 mph before it malfunctioned due to the wind blown hail. The Norman mesonet site measured a gust of 70 mph. A quick inch of rain occurred in about 15 to 20 minutes. This wasn't the only storm to affect parts of central Oklahoma, as some areas received three different rounds of large hail. The thunderstorms moved east, affecting parts of southern Oklahoma through mid evening. The storms weakened in intensity as they moved into eastern and southeast Oklahoma.

Fig. 4.1. Official storm reports and event narrative for the Norman, Oklahoma, downburst from the National Centers for Environmental Information (NCEI) Storm Events Database. The table abbreviations are: St. is state; T.Z. is time zone; Mag is magnitude; Dth is deaths; Inj is injuries; PrD is property damage estimate; and CrD is crop damage estimate. From NOAA/NCDC (2011).

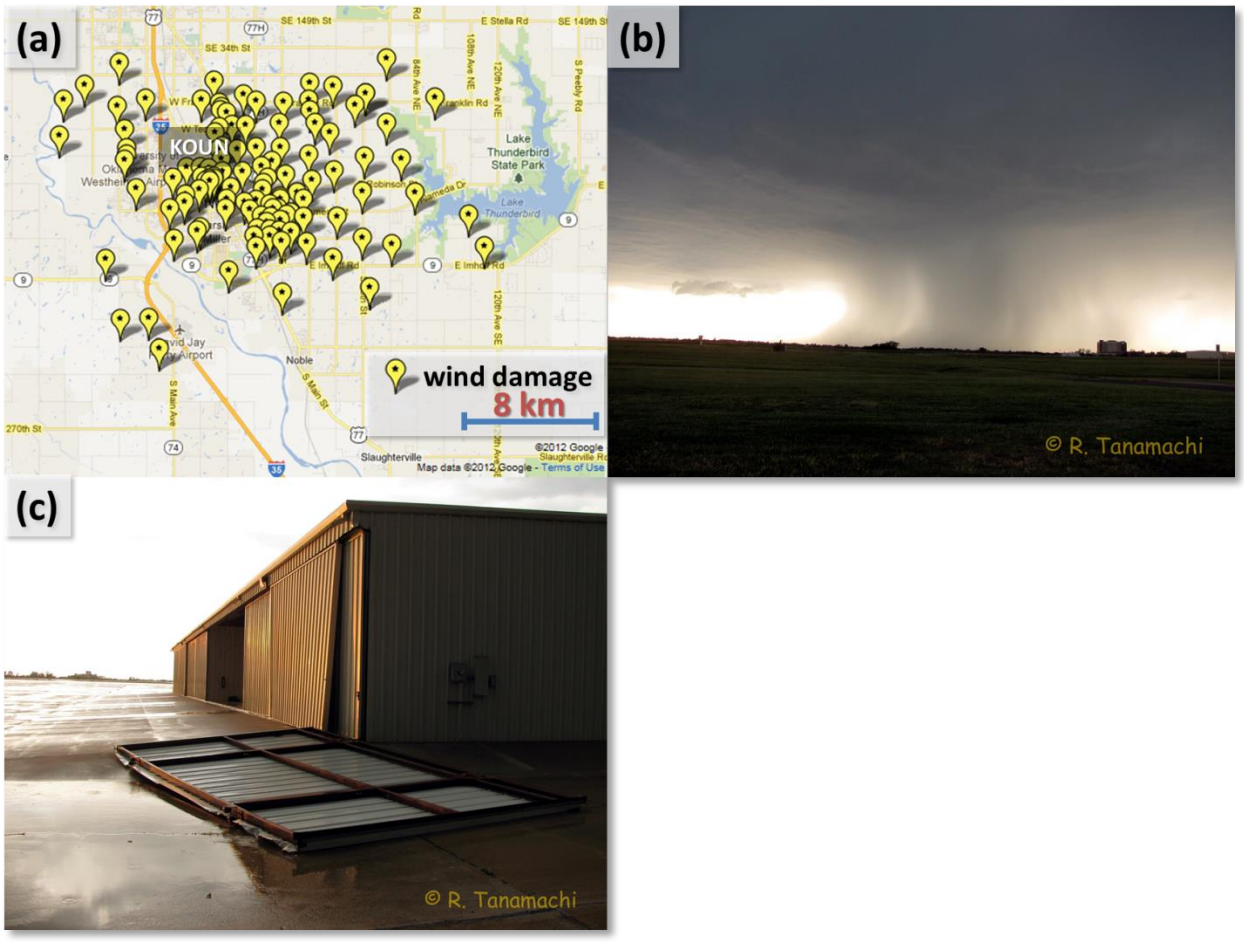


Fig. 4.2. Map of wind damage reports (courtesy National Weather Service Norman, Oklahoma), (b) photo of the downburst from north Norman, and (c) photo of damage at Max Westheimer Airport. Photos courtesy Robin Tanamachi.

4.2 Mesoscale and Thermodynamic Environment

The thermodynamics of the atmosphere were highly conducive for storms to produce severe downbursts in Central Oklahoma on 14 June. The Norman (KOUN) sounding at 0000 UTC on 15 June 2011 was the closest spatiotemporal sounding to the downburst (Fig. 4.3). The downburst affected Norman just after 0020 UTC; therefore, the sounding should be a reasonable representation of the pre-storm environment.

As shown by the calculated parameters, the atmosphere was favorable for organized severe thunderstorms with both moderate instability and vertical wind shear. A nearly dry adiabatic (well-mixed) layer existed below the cloud layer, which is favorable for downbursts (Srivastava 1987) and results in large downdraft convective available potential energy (DCAPE). DCAPE is defined as the maximum increase in kinetic energy (per unit mass) that could result from evaporative cooling from some height to the surface (Emanuel 1994). Note that this sounding is not a classic wet downburst sounding (i.e., Atkins and Wakimoto 1991) due to the relatively dry boundary layer and steep low-level lapse rates.

A couple parameters that specifically have been computed to assess downburst potential are the $\Delta\theta_e$ between the near-ground maximum and the mid-level minimum (Atkins and Wakimoto 1991) and the Wind INDEX or WINDEX (McCann 1994). The WINDEX formula is:

$$WI = 5\left[H_m R_Q (\Gamma^2 - 30 + Q_L - 2Q_m)\right]^{0.5} \quad (4.1)$$

where H_m is the height of the melting level in km above ground, $R_Q = Q_L/12$ but not greater than 1, Γ is the lapse rate in °C per km from the surface to the melting level, Q_L is the mixing ratio in the lowest 1 km above the surface, and Q_m is the mixing ratio at the melting level. The formula is an empirical relationship.

The $\Delta\theta_e$ of 18.4 K is lower than the 20 K threshold for wet downbursts found in Atkins and Wakimoto (1991); however, this could be attributed to not being a classic wet downburst sounding. Finally, the WINDEX was calculated to be 30.4 m s^{-1} (59 knots), which underestimated the > 35 m s^{-1} measured surface winds.

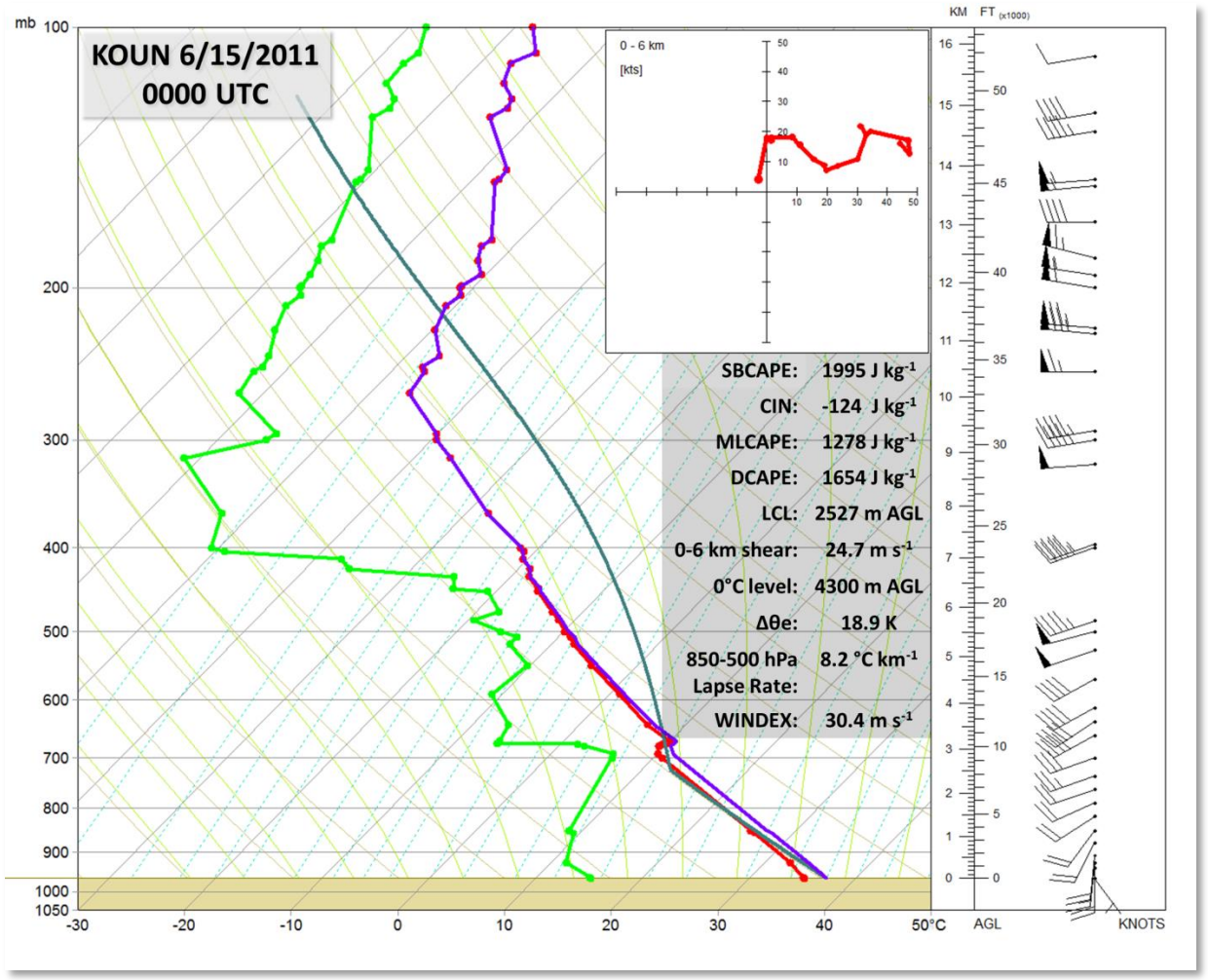


Fig. 4.3. Upper-air sounding and hodograph from Norman, Oklahoma (KOUN) at 0000 UTC 15 June 2011. Temperature is denoted by the red line and dew point by the green line. The purple line is the virtual temperature correction, and the turquoise line represents the parcel path for surface-based parcel. Plotted using The Universal Rawinsonde Observation (RAOB) program.

On the mesoscale, a cold front was located across central Oklahoma (Fig. 4.4). The temperature change across the cold front was weak (~3 to 4°C). The wind shift along the cold front was nearly 180°; thus, surface convergence was present along the boundary. The convergence along the cold front was also detected by the KTLX WSR-88D radar in the velocity data (not shown). This was coincident with a weak line of Z_H, which indicates there was a buildup of particulates and insects along the convergence line. KTLX was not dual-pol capable

in 2011, so no PRD were available. The thunderstorm that would produce the downburst initiated just ahead of a cold front, near the Minco Mesonet site due west of the Norman site, around 2315 UTC on 14 June 2011 (Figs. 4.4a,b).

Initially, the storm motion was northeastward, parallel to the cold front. The thunderstorm rapidly intensified between 2315 and 2345 UTC (Figs. 4,4a,b). By 2345 UTC, the thunderstorm began to split into two cells. The Minco Mesonet station experienced an 8°C decrease in temperature and a 5°C increase in dew point as the storm passed by between 2335 and 2355 UTC (not shown). The left split had a storm motion that was predominantly northward; the right split had an east southeastward storm motion. The right split was the thunderstorm that would produce a downburst in Norman, Oklahoma (Fig. 4.4c). Even though this was a right-mover thunderstorm, there was no evidence of a mesocyclone aloft (i.e., a supercell). Therefore, the cause of the split is unknown. One feature of note is the split occurred simultaneously from when the thunderstorm was intersected by the cold front.

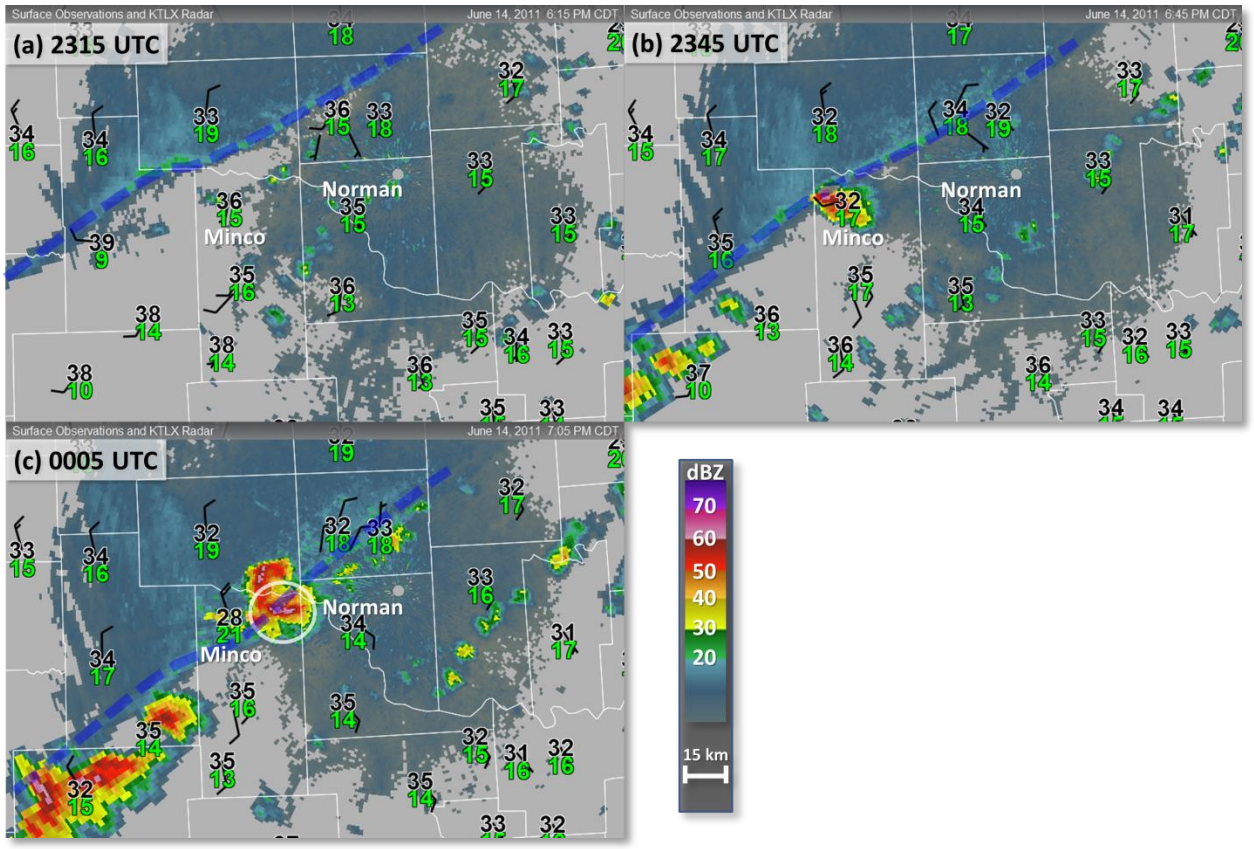


Fig. 4.4. KTLX radar reflectivity (dBZ) and Oklahoma Mesonet surface observations valid at (a) 2315, (b) 2345, and (c) 0005 UTC. Surface temperature (°C), dew point (°C), and wind barbs (full barb ≡ 5 m s^{-1}; half barb ≡ 2.5 m s^{-1}) are plotted. The white circle highlights the storm that would produce the downburst. The dashed blue line is the approximate location of the cold front. The location of the Norman and Minco Mesonet stations are indicated. Plotted using WeatherScope from the Oklahoma Climate Survey.

4.3 1-Min Mesonet Observations of the Downburst

Figure 4.5 shows the 1-min Norman Mesonet data plots from 2330 to 0130 UTC. Initially, the station pressure was steady at ~963.5 hPa from 2330 to 2350 UTC. After 2350 UTC, there was a steady decrease of pressure until 0013 UTC. The gust front passed by the Mesonet station at 0025 UTC, when the wind speed at the station increased from below 10 m s^{-1} to over 30 m s^{-1} in about five minutes. The gust front represents the leading edge of the outflow

from the ambient air. It is speculated that the pressure decrease ahead of the gust front was due to subsidence warming as seen in squall lines (Hoxit et al. 1976). The pressure minimum was followed by a pressure rise and likely rising motion on the leading edge of the gust front. With the gust front passage, the temperature decreased from 34°C at 0025 UTC to 22°C at 0033 UTC, which was accompanied by a relative humidity increase from 34% to 94%. Thereafter, the temperature and relative humidity remained nearly steady-state with only slight fluctuations. The decrease in temperature and increase in relative humidity behind the gust front were due to melting hailstones and evaporating raindrops, which remove latent heat from the atmosphere (i.e., diabatic cooling). The maximum wind gust was 31.5 m s^{-1} from the northwest (322°) at 0029 UTC. A severe thunderstorm has wind gusts greater than or equal to 25.7 m s^{-1} (National Weather Service 2018). Therefore, the wind speed and the accompanying features qualify the event as a severe downburst.

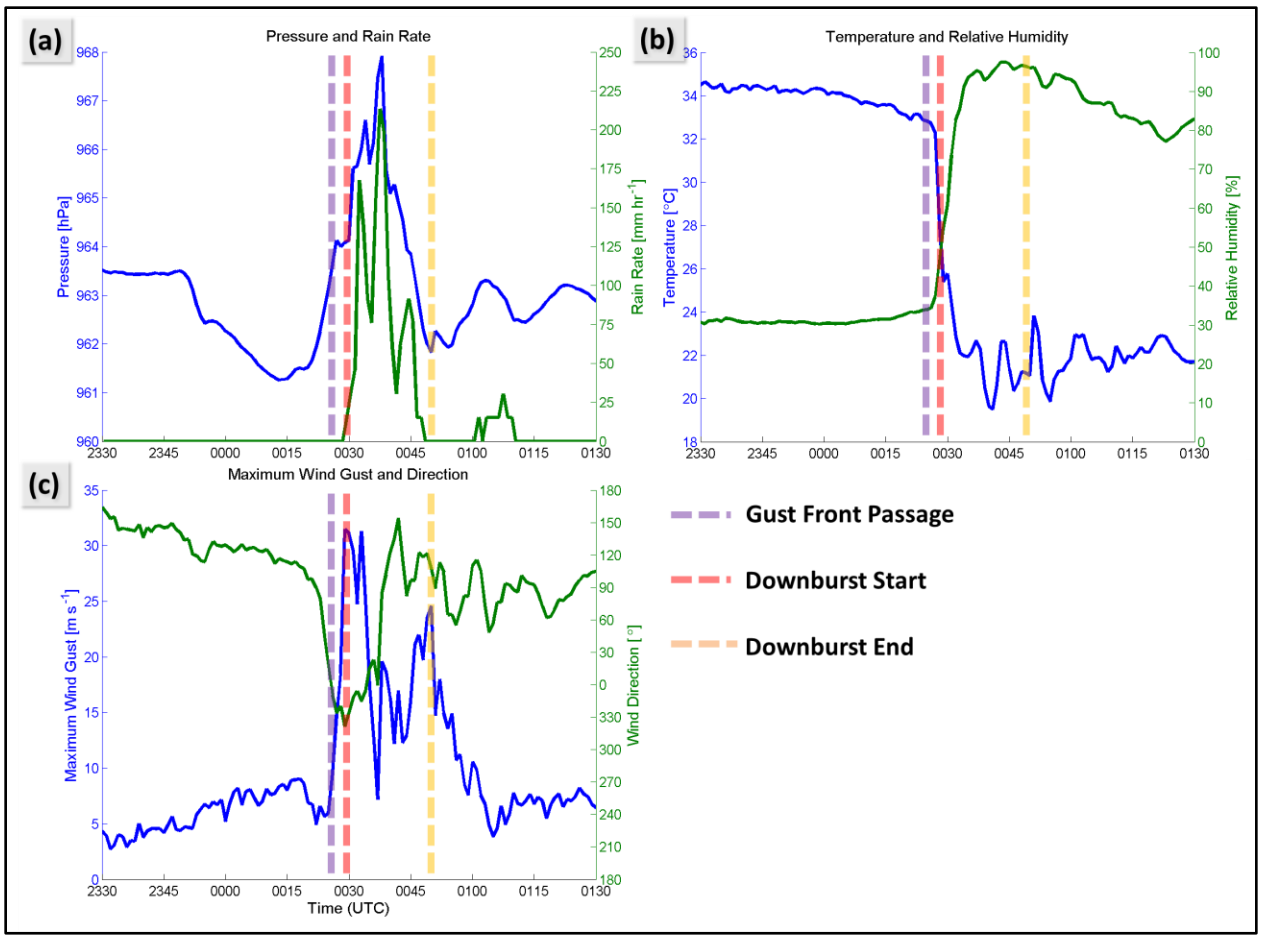


Fig. 4.5. 1-min Oklahoma Mesonet data at Norman, Oklahoma, of (a) surface pressure (hPa) and rain rate (mm hr^{-1}), (b) 2 m temperature (°C) and 2 m relative humidity (%), and (c) 10 m maximum wind gust (m s^{-1}) and wind direction (degrees) valid from 2330 to 0130 UTC. The times of the gust front passage, downburst start, and downburst end are noted by the dashed lines.

Rain began to fall at the station between 0029 and 0030 UTC. Another wind gust of 31.3 m s^{-1} occurred at 0033 UTC. The rain rate rapidly increased to 168 mm hr^{-1} between 0032 to 0033 UTC. The atmospheric pressure increased to 966.6 hPa at 0034 UTC; however, the pressure decreased thereafter until 0036 UTC. The rain rate peaked at 213 mm hr^{-1} (~8.4 in hr^{-1}) between 0037 and 0038 UTC. The peak rain rate was coincident with an atmospheric pressure of 967.9 hPa at 0038 UTC, which was the maximum atmospheric pressure during the event. Note

that this maximum is the 1-min average atmospheric pressure using a sampling period of 12 s. The maximum 12 s sample of atmospheric pressure within that minute was 968.7 hPa (not shown). The minimum (1-min average) atmospheric pressure was 961.3 hPa at 0013 UTC. The minimum 12-s atmospheric pressure within that minute was 961.2 hPa (not shown). Therefore, there was a 6.6 hPa increase in (1-min average) pressure in 15 minutes.

Typically, a downburst is defined by strong outflow winds at the surface; however, the center of the mesohigh associated with the cold pool is a better representation of the downdraft location. For example, (Proctor 1989) found a pressure dome beneath the downdraft in his numerical simulation of a microburst. Recall that the increased pressure at the surface may be created both dynamically (i.e., stagnation point from downward motion) and thermodynamically (i.e., weight of cold air). While there might have been a thermodynamic component, note that there were not significant temperature fluctuations (at least at the surface) after the passage of the gust front. This implies that the dynamic component may have played a role in the development of the mesohigh as well. As shown in Chapter 2, the downward acceleration from the dynamic component is driven by buoyancy (i.e., precipitation loading and thermal buoyancy through evaporation and/or melting of hydrometeors). Negative thermal buoyancy did have some contribution to the downward motion with a > 10 °C cooling behind the gust front. Even so, the maximum atmospheric pressure (i.e., the center of the downburst) being coincident with the (intense) peak rain rate implies that precipitation loading may also have played a role in the dynamics (i.e., the downward acceleration) of this wet downburst.

Several additional wind gusts of $\geq$ 20 m s^{-1} occurred until 0050 UTC. The final downburst-related wind gust was 25 m s^{-1} from the east-southeast (108°) at 0050 UTC. Note that the wind direction switched ~150° from beginning to end, indicating the station experienced

outflow from opposite sides of the downburst. This is reasonable because the pressure maximum and large rain rate suggest the center of the downburst passed over or close to the Norman Mesonet station. The presence of several wind gust surges and a secondary pressure maximum suggest the downburst event was the aggregation of several downdraft surges or pulses within the storm. Downdraft surges previously were documented in 1-min Oklahoma Mesonet data during the 17 August 1994 Lahoma, Oklahoma, windstorm (Morris and Shafer 1996) and have been well-documented in rear-flank downdrafts (RFDs) associated with supercell thunderstorms (e.g., Kosiba et al. 2013; Marquis et al. 2008; Skinner et al. 2011; Wurman et al. 2010).

Figure 4.6 summarizes the observations of the downburst at the Oklahoma Mesonet station. The start and end times of the downburst event at the Oklahoma Mesonet are defined by the first and last wind gust ≥ 20 m s^{-1}. Therefore, the start time is 0029 UTC and the end time is 0050 UTC.

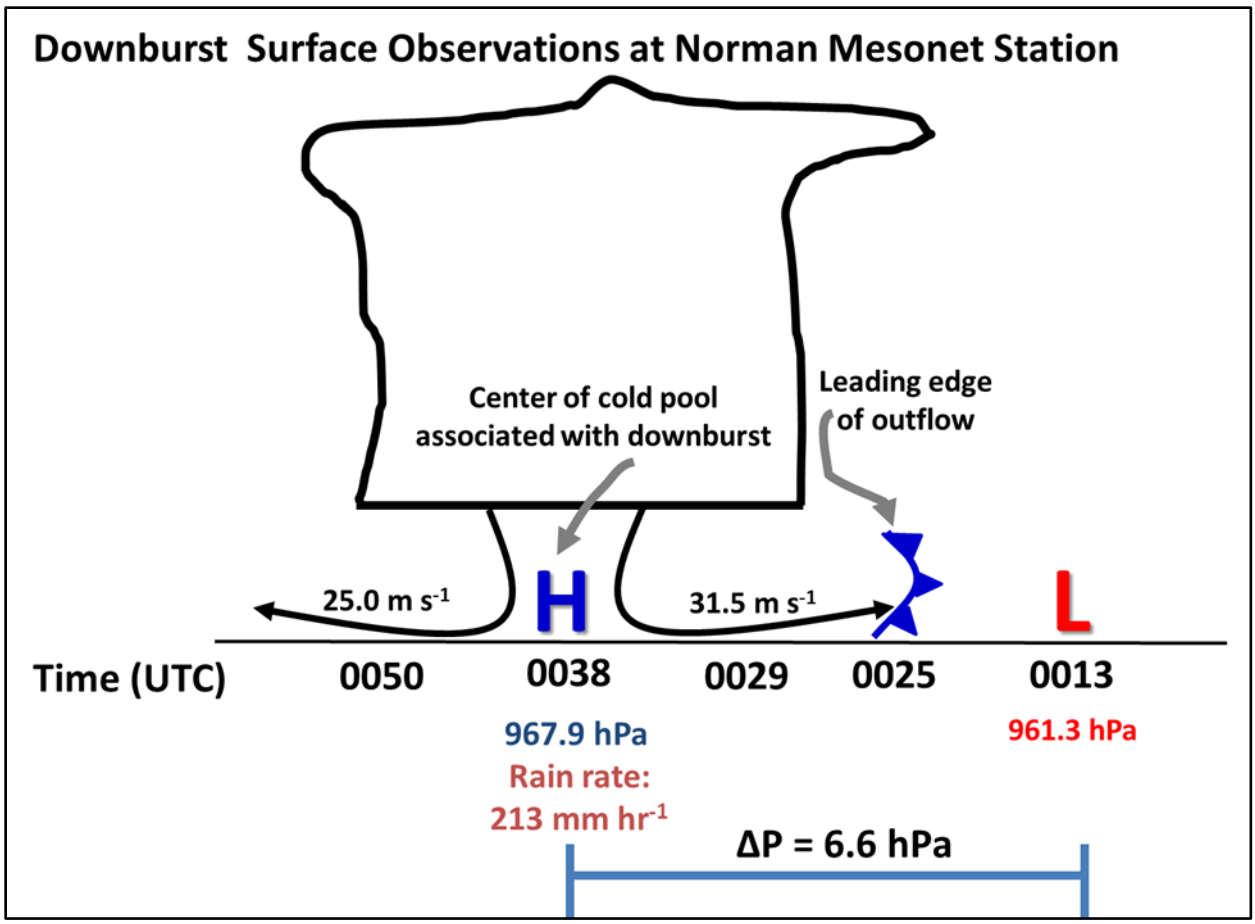


Fig. 4.6. Time evolution of surface observations as the downburst passed over the Oklahoma Mesonet station at Norman, Oklahoma. Time relative maximum and minimum surface pressure are noted by "H" and "L", respectively. Gust front passage is noted by cold front symbol. Schematic is based upon 1-min data from Figure 4.5.

4.4 Quantitative Estimate of the Downward Acceleration Due to Buoyancy

Using the Mesonet data, back of the envelope calculations can be used to estimate the order of magnitude for the contributions to the downward acceleration in the downburst. Recall that buoyancy (neglecting the pressure buoyancy term) is defined as (2.2):

$$B \approx g\left[\frac{\theta_v^*}{\theta_{v_o}} - q_H\right]$$

To estimate the thermal buoyancy term, θ_{v_o} and θ_v^* are estimated to be ~307 K (34 °C) and ~-10 K, respectively from the Mesonet data. These are based on the temperature measurements ahead of and immediately after the passage of the gust front. Using these values is an assumption because these measurements are from the surface. The estimated downward acceleration due to thermal buoyancy is ~-0.3 m s^{-2}.

To estimate the precipitation loading term, Srivastava's (1985) study will be used as a baseline. For the rain rate of 110 mm hr^{-1}, rainwater mixing ratio was approaching 10 g kg^{-1} in his study (Fig. 2.7). Therefore, it will be assumed that with the rain rate of 213 mm hr^{-1}, the combined precipitation loading from rain and hail is ~20 g kg^{-1}. The estimated downward acceleration due to precipitation loading is ~-0.2 m s^{-2}.

From these calculations, it appears at first glance that thermal buoyancy may have played a slightly larger role in the downburst; however, in reality, these terms were not steady-state during the duration of the downburst event. Initially, thermal buoyancy may have dominated with a dry subcloud layer and a relatively high lifting condensation level (LCL) height. The potential for thermal buoyancy may have decreased toward the latter part of the downburst event (assuming less evaporation due to subcloud layer becoming more saturated). However, melting hail may have still contributed to negative thermal buoyancy since melting could still occur even if the environment was saturated.

Chapter 5 : WSR-88D Dual-Pol Observations, HCA, and Analysis[4]

Both the research KOUN and operational KTLX WSR-88D radars were scanning this downburst and its parent storm at close range (<30 km). KOUN provided PRD while both radars provided limited dual-Doppler coverage. In this chapter, the evolution of the downburst is analyzed mostly through the use of RHIs of the PRD. An HCA is applied to the PRD to gain further understanding of the microphysical evolution of the downburst. The HCA analyses are utilized to develop a conceptual model that characterizes the hydrometeor evolution of the parent downburst storm. The analysis period for this chapter is from 2333 UTC to 0027 UTC.

5.1 HCA Overview

HCAs have used PRD to classify radar echoes for different hydrometeors and non-meteorological scatterers (e.g., Straka and Zrnić 1993). HCAs are usually based upon fuzzy logic and the classification techniques have become more sophisticated in recent years (e.g., Lim et al. 2005; Liu and Chandrasekar 2000; Park et al. 2009; Straka et al. 2000; Vivekanandan et al. 1999; Zrnic and Ryzhkov 1999). HCAs aggregate different radar variables to determine the different hydrometeor classes, which can reveal the evolution of storm microphysics.

The basis of the HCA used in S-band WSR-88D radars was developed by Park et al. (2009) (hereafter referred to as P09) and is based upon the fuzzy logic method. The P09 HCA distinguishes among 10 classes of radar echoes: 1) ground clutter and anomalous propagation (GC/AP); 2) biological scatterers (BS); 3) dry aggregated snow (DS); 4) wet snow (WS); 5) crystals (CR); 6) graupel (GR); 7) big drops (BD); 8) light and moderate rain (RA); 9) heavy rain (HR); and 10) a mixture of rain and hail (RH).

[4]Adapted from: Mahale, V. N., G. Zhang, and M. Xue, 2016: Characterization of the 14 June 2011 Norman, Oklahoma, downburst through dual-polarization radar observations and hydrometeor classification. *J. Appl. Meteor. Clim.*, **55,** 2635–2655.

In this study, a modified version of the P09 HCA as described in Mahale et al. (2014) is used for analysis of the microphysical evolution. The methodology of the HCA in Mahale et al. (2014) is described in the following paragraphs with modifications. This HCA was chosen because a version of it is implemented on the WSR-88D network. The following simplifications were made when compared to the original algorithm, which include: 1) No use of K_{DP}; 2) No attenuation correction for Z_H or Z_{DR}; and 3) No confidence vectors. Confidence vectors account for the impact of the measurements errors (e.g., radar miscalibration, nonuniform beam filling, partial beam blockage, and receiver noise) in the P09 HCA. These simplifications are made because of varied methods and uncertainty in K_{DP} calculations and attenuation correction, and the need to determine confidence vectors. Mahale et al. (2014) found the results from these simplifications are "fairly similar to those of the operational algorithm used to produce the HCA categories in the Level-3 WSR-88D data". Therefore, the five variables used for the discrimination of hydrometeors and non-meteorological scatterers are: 1) Z_H; 2) Z_{DR}; 3) ρ_{hv}; 4) a texture parameter, SD(Z_H); and 5) another texture parameter, SD(Φ_{DP}).

The classification of the radar echo is determined by which class has the largest aggregation value, which is dependent on what hydrometeors provide the dominant signal within a radar resolution volume (i.e., radar gate). Therefore, it is reasonable to assume there possibly could be a mix of hydrometeors in a radar resolution volume even outside the mixture of rain and hail classification. One hydrometeor may serve as an embryo for a different hydrometeor. For example, Harimaya (1976) found both snow crystals and frozen drops as center particles for graupel particles. It is understood that graupel develops as supercooled water droplets freeze on contact with snow crystals (i.e., riming; Lamb and Verlinde 2011). Thus, in regions of graupel formation, supercooled droplets and snow crystals would be expected to be present as well. This

is an example where the HCA could give insight into the ongoing microphysical processes within the storm.

As described in Mahale et al. (2014), the depth of the melting layer can be estimated using the height of reduced ρ_{hv} rings in higher elevation PPI scans. Automated melting layer detection algorithms (e.g., Brandes and Ikeda 2004; Giangrande et al. 2008) utilize reduced ρ_{hv} to help determine the melting layer because of its sensitivity to large, wetted particles (e.g., melting hydrometeors). For example, Giangrande et al. (2008) used ρ_{hv} values between 0.90 and 0.97 as a starting point in their algorithm. Therefore, using reduced ρ_{hv} rings should provide similar results to automated algorithms. Using ρ_{hv} rings is advantageous when compared to Z_H rings because it is more sensitive to melting hydrometeors in some situations where Z_H does not display enhanced-reflectivity (i.e., brightband) signatures (Giangrande et al. 2008).

The top of the melting layer (i.e., the estimated 0 °C level) is the height associated with the farthest distance of the ρ_{hv} ring, which was close to the height of the 0 °C level on the observed sounding (Fig. 4.3) in this study (~4.3 km above ground level). The bottom of the melting layer is the height associated with the closest distance of the ρ_{hv} ring. Therefore, the radial extent of the ρ_{hv} ring is proportional to the depth of the melting layer. The following restrictions are placed on classes based upon the melting layer: 1) above the 0 °C level, the only classes allowed are DS, CR, GR, and RH; 2) within the melting layer, the only class not allowed is BS; and 3) below the melting layer, the only classes allowed are GC/AP, BS, BD, RA, HR, and RH. Otherwise, as noted in Mahale et al. (2014), the membership functions, weights, and hard thresholds are the same as implemented in P09. For PPIs, a 9-point median filter of the raw classifications is done to account for errors in the HCA output and noise in the Level-2 radar data. For reconstructed RHIs, a 3-point median filter of the raw classifications is done radially.

In addition, quality control was done on the reconstructed RHI radar data for this event. The default signal-to-noise (SNR) Z_H threshold for WSR-88D radar data is 2 dB (Melnikov and Zrnić 2007). In other words, Z_H is only calculated where SNR is estimated to be larger than 2 dB. Using this threshold, the range-dependent minimum detectable Z_H was estimated by calculating the azimuthal median Z_H on the extreme peripheral of some precipitation. The median Z_H was assumed to be representative of the minimum detectable Z_H at that range. The Z_H estimate was then extrapolated for the entire range of the radar observations. This allowed for the estimation of the SNR for the entire radar domain, which is not provided in the Level-2 radar data. Melnikov and Zrnić (2007) found that Z_{DR} and ρ_{hv} are susceptible to bias for SNR interval of 2–15 dB. For this study, data where SNR were less than 10 dB (i.e., radar data that were 10 dB greater than the minimum detectable Z_H) were removed to reduce the influence of noise.

5.2 Polarimetric radar observations and HCA

One way to gain understanding on the storm microphysics associated with the downburst is to study the spatiotemporal changes in both the PRD and the output of the HCA in the parent thunderstorm. The azimuths for these reconstructed RHIs were subjectively selected through the most intense part of the thunderstorm for each volume scan. No objective analysis scheme was used when creating the RHIs

In the developing stage of the storm, there was a Z_{DR} column that existed above the melting layer of ~4.3 km (Fig. 5.1a). Z_{DR} columns indicate the presence of liquid or mixed-phase oblate hydrometeors being lofted above the 0°C level by the storm updraft (e.g., Hall et al. 1984; Kumjian and Ryzhkov 2008; Kumjian et al. 2012). Therefore, the Z_{DR} column can be considered a proxy for the updraft location within the storm; however, the Z_{DR} column could be slightly

offset from the most intense portion of the updraft (e.g., Loney et al. 2002; Wienhoff et al. 2018). Z_{DR} columns that penetrate above the 0 °C level indicate the presence of a very strong updraft (Kumjian et al. 2012). In the 2333-2337 UTC volume scan (Fig. 5.1a), the Z_{DR} column extended to at least 6.5 km above radar level (ARL), or ~2.2 km above the 0°C level, with a Z_{DR} estimate of 2.6 dB at the top of the column. The deep Z_{DR} column indicates that the storm had a relatively intense updraft. There was also a low ρ_{hv} column collocated with the Z_{DR} column, suggesting mixed-phase hydrometeors were present within the updraft column. The HCA output (Fig. 5.2a) indicates primarily graupel with some rain and hail mixture within and above the Z_{DR} column.

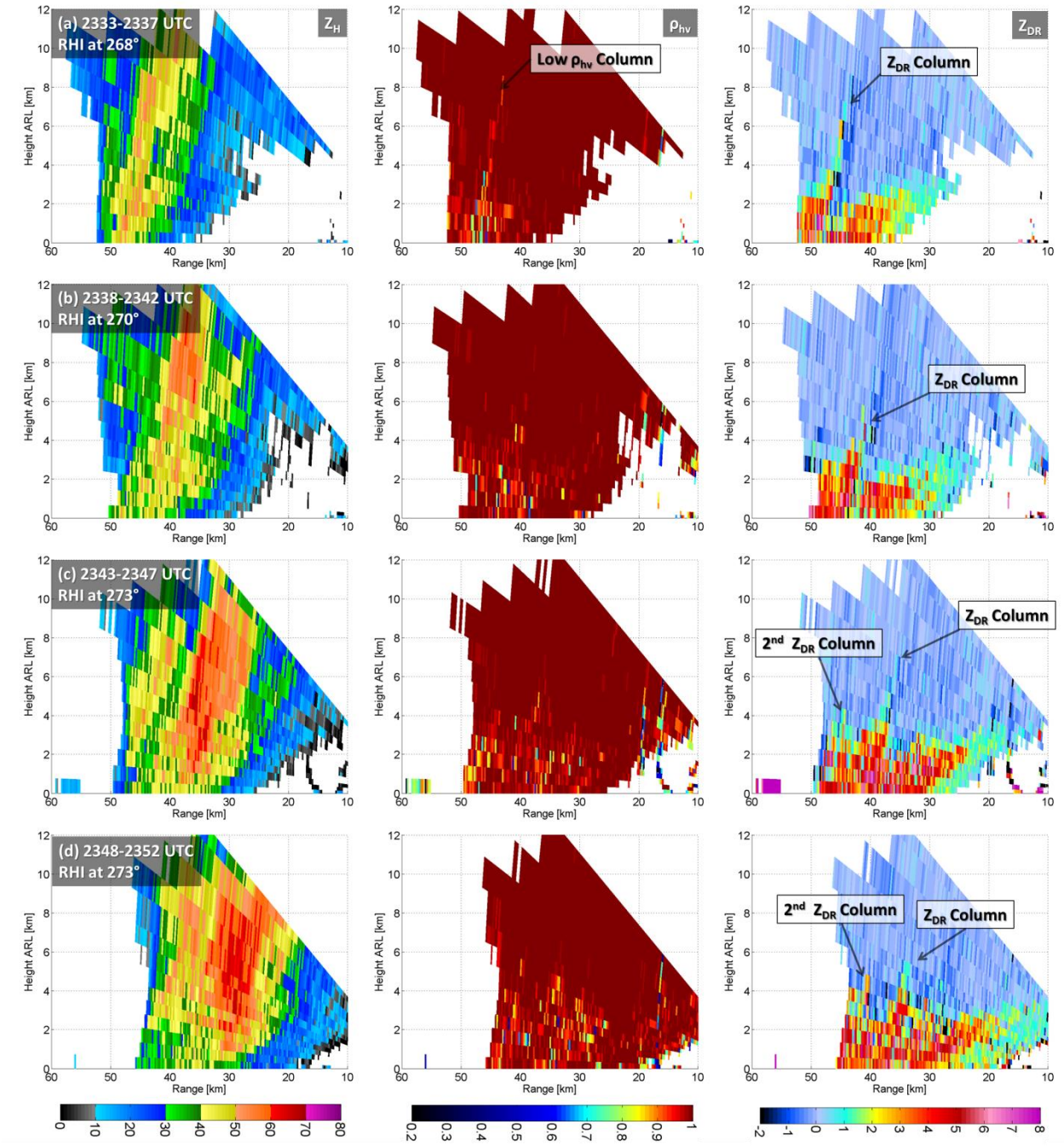


Fig. 5.1. Reconstructed range height indicator (RHI) analyses from KOUN. Horizontal radar reflectivity factor (Z_H), co-polar correlation coefficient (ρ_{hv}), and differential reflectivity (Z_{DR}) are shown at (a) 2333-2337 UTC, (b) 2338-2342 UTC, (c) 2243-2347 UTC, and (d) 2348-2352 UTC volume scans. Axes are labeled relative to KOUN. RHI azimuth angle and noteworthy storm features are denoted.

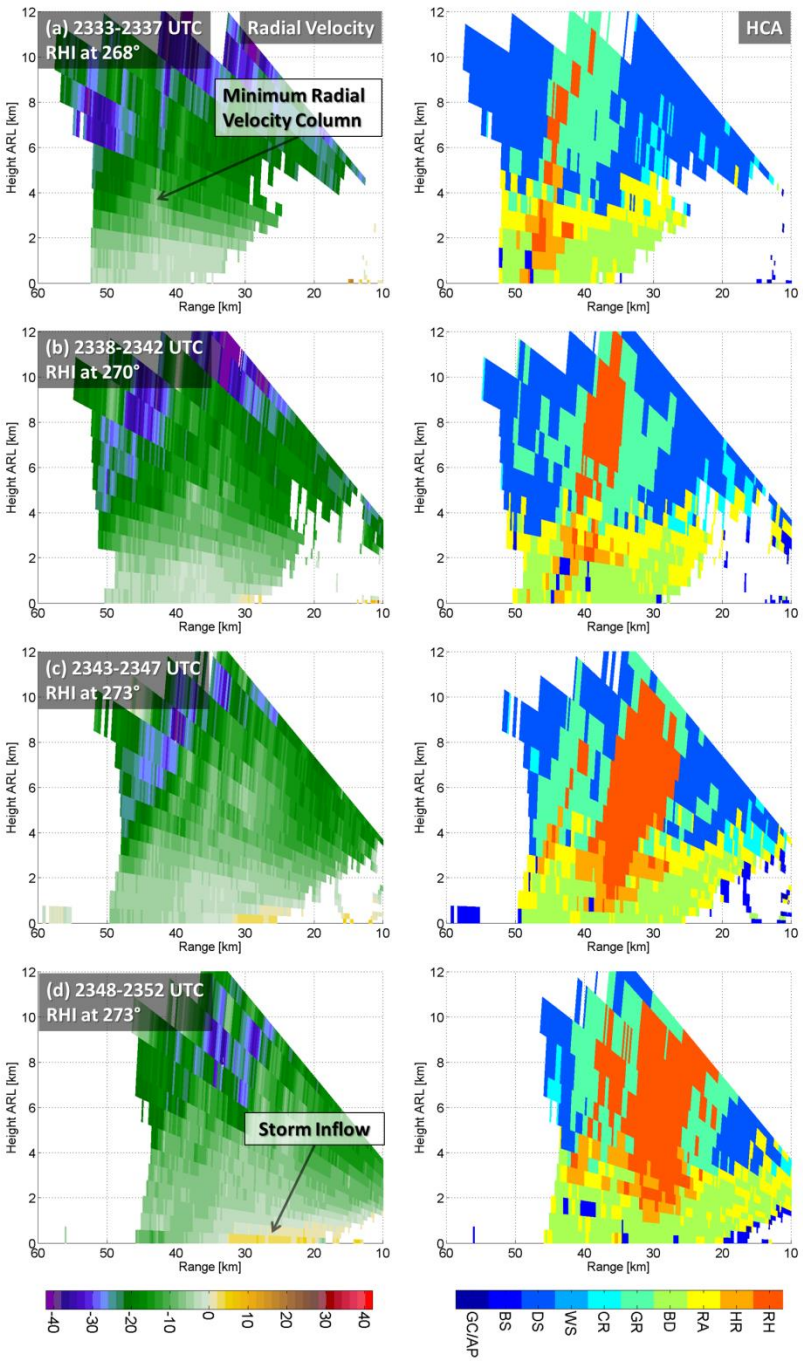


Fig. 5.2. Reconstructed range height indicator (RHI) analyses from KOUN. Radial velocity (V_R) and hydrometeor classification algorithm (HCA) are shown at (a) 2333-2337 UTC, (b) 2338-2342 UTC, (c) 2243-2347 UTC, and (d) 2348-2352 UTC volume scans. The classifications on the right panel are: 1) ground clutter and anomalous propagation (GC/AP); 2) biological scatterers (BS); 3) dry aggregated snow (DS); 4) wet snow (WS); 5) crystals (CR); 6) graupel (GR); 7) big drops (BD); 8) light and moderate rain (RA); 9) heavy rain (HR); and 10) a mixture of rain and hail (RH). Axes are labeled relative to KOUN. RHI azimuth angle and noteworthy storm features are denoted.

Other hydrometers, such as supercooled droplets and snow crystals, probably are present in regions denoted as graupel because they are necessary for the formation of graupel (e.g., Pruppacher and Klett 2010). There was also a column of decreased inbound V_R collocated within the Z_{DR} column, which is further confirmation that the flow was more vertical rather than horizontal within this portion of the storm.

In the 2338-2342 volume scan (Fig. 5.1b), the Z_{DR} column maintained itself to at least 6.0 km ARL, or 1.7 km above the 0 °C level. The HCA output (Fig. 5.2b) indicates that the area of graupel had transitioned to primarily rain and hail mixture within and above the Z_{DR} column. An overall increase of $Z_H \geq 50$ dBZ within and above the Z_{DR} column is the primary reason why the HCA output indicates the presence of more rain and hail mixture than in the previous volume scan. Hailstones have two different precursors (i.e., hail embryos) for development, which are frozen-drop embryos or graupel embryos (Knight 1981). The embryo type depends on the depth of the layer in which the warm-cloud process of collision-coalescence may occur (i.e., the depth of the > 0 °C region within the storm); the shallower the warm-cloud region, the more likely that hailstones will develop from graupel embryos. In this particular storm, there was a large area of graupel in the cold-cloud region that was a much greater area than the warm-cloud region, suggesting graupel embryos were the precursor to hail formation. The areal increase of rain and hail mixture aloft from the conversion of graupel was probably due to the intense updraft, as indicated by the persistent, deep Z_{DR} column.

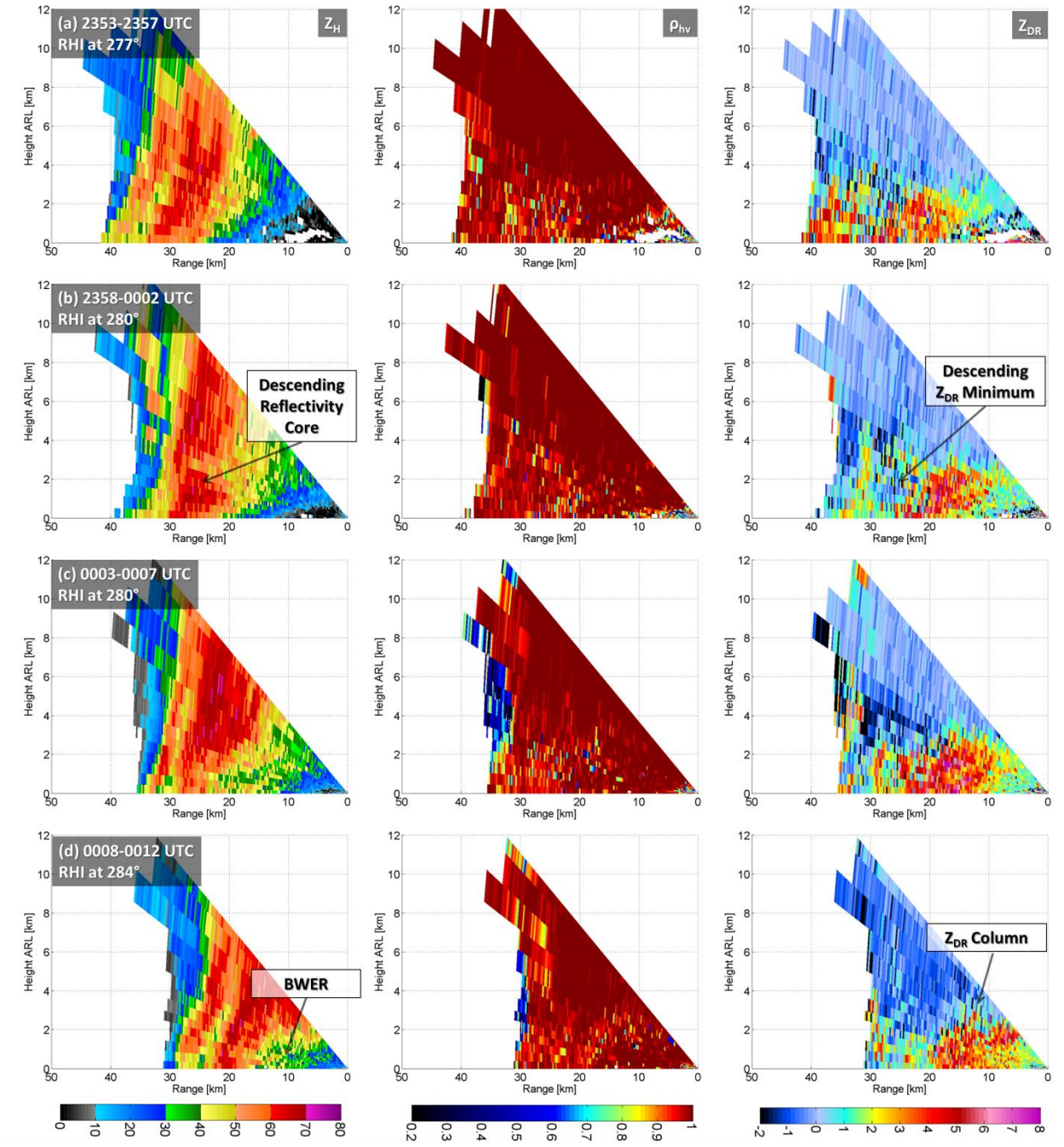


Fig. 5.3. Same panels as Figure 5.1, but at (a) 2353-2357 UTC, (b) 2358-0002 UTC, (c) 0003-0007 UTC, and (d) 0008-0012 UTC volume scans.

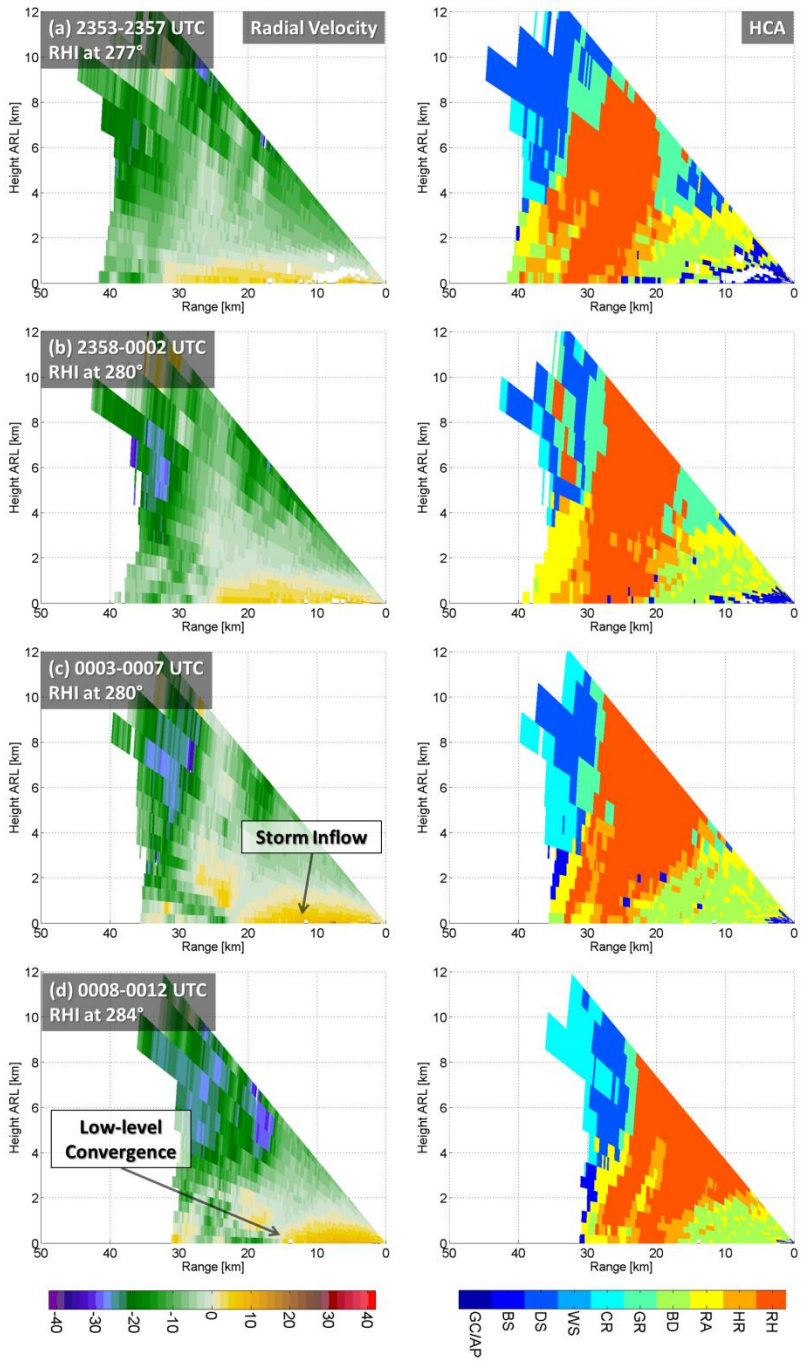


Fig. 5.4. Same panels as Figure 5.2, but at (a) 2353-2357 UTC, (b) 2358-0002 UTC, (c) 0003-0007 UTC, and (d) 0008-0012 UTC volume scans.

The Z_{DR} column continued to maintain itself in the 2343-2347 UTC volume scan (Fig. 5.1c). Behind the primary Z_{DR} column, there was evidence of a developing secondary Z_{DR} column ~44 km downrange from the radar. The height of the secondary Z_{DR} column was only ~4.6 km ARL with a Z_{DR} estimate of 2.1 dB at the top of the column. The secondary Z_{DR} column may represent an updraft pulse behind the primary updraft. A secondary region of enhanced Z_H within and above the secondary Z_{DR} column, separated from the primary region of Z_H, is further evidence of an updraft pulse. Furthermore, the HCA output (Fig. 5.2c) also indicates a new region of rain and hail mixture within and above the secondary Z_{DR} column. This updraft pulse represents the multicellular nature of these storms; recall that the storm had previously split into two distinct cells. There also was an increase in outbound V_R in the lowest two elevation scans ~25-32 km downrange from the radar, indicating increased inflow into the storm.

The storm maintained its intensity during the 2348-2352 UTC volume scan (Fig. 5.1d). The primary Z_{DR} column was still present to ~5.7 km ARL with a Z_{DR} estimate of 1.3 dB at the top of the column. The Z_{DR} column had become offset slightly downrange of the greatest Z_H estimates. A large area of $Z_H \geq 60$ dBZ was present, primarily from the 0 °C level and above. In addition, the outbound V_R (Fig. 5.2d) had expanded even farther downrange and higher into the storm, nearly coincident with the location of the Z_{DR} column. Therefore, the depth and intensity of the inflow into the storm had continued to increase in this volume scan. Evidence of the updraft pulse from the previous volume scan was still present as indicated by a secondary Z_{DR} column, enhanced Z_H, and a separated rain and hail mixture region downrange from the primary Z_{DR} column. The areal coverage of the primary rain and hail mixture had continued to increase aloft during this volume scan as well.

In the next series of volume scans (Fig. 5.3 and Fig. 5.4), there is evidence of at least one descending Z_H core to the surface. During the 2358-0002 UTC volume scan, there was an area of ≥ 60 dBZ, Z_{DR} ~0 dB, and a decrease in ρ_{hv} ~20-30 km downrange from the radar that had descended to near the surface (Fig. 5.3b). In the HCA output, there is separated area of rain and hail mixture that has descended to the surface (Fig. 5.4b). There were no reported wind or hailstones with this descending Z_H core; however, this is evidence that this storm was capable of producing several downburst and/or hail events as the storm continued to maintain its intensity even after the Z_H core had descended to the surface. In addition, this series of volume scans indicates that the Z_{DR} column dissipated and reappeared within the storm in subsequent volume scans. However, this was probably an artifact of the WSR-88D's sampling of the storm; frequent and dense mid-level scans are necessary to accurately monitor the Z_{DR} column and associated updraft strength (Snyder et al. 2015; Tanamachi and Heinselman 2016). The reappearance of the Z_{DR} column on the 0008-0012 UTC volume scan (~13 km downrange from the radar) without any weakening of the storm brings credence to this hypothesis (Fig. 5.3d). The Z_{DR} column is nearly collocated with low-level radial convergence and a bounded weak-echo region (BWER), which is further evidence this is the location of the updraft. The HCA indicates big drops within the BWER, which would be expected since these are oblate hydrometeors (e.g., Kumjian and Ryzhkov 2008; Kumjian et al. 2012). Unfortunately, due to the radar cone of silence, the radar is only able to see below the 0°C level in the region.

The next three volume scans capture the microphysical evolution of the Norman, Oklahoma, downburst (Fig. 5.5 and 5.6). A rain and hail core aloft was present ~5-8 km downrange from the radar during the 0013-0017 UTC volume scan (Fig. 5.5a). The HCA output indicates the presence of rain and hail mixture within this region (Fig. 5.6a). Though rain and

hail mixture does not have a clear boundary downrange on the HCA output, increased Z_{DR} estimates on either side of the rain and hail core can be utilized to separate out a distinct rain and hail core.

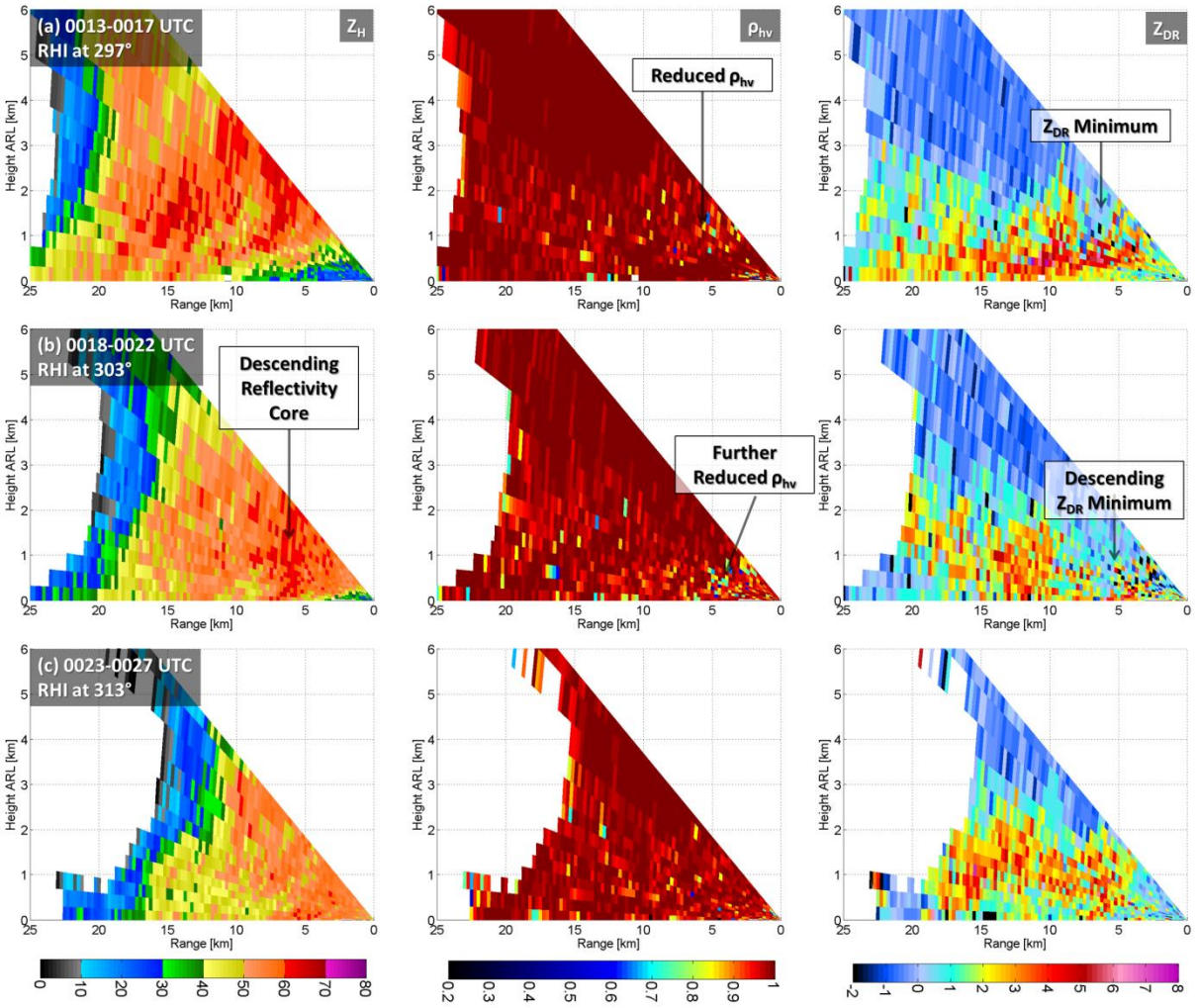


Fig. 5.5. Same panels as Figure 5.1, but at (a) 0013-0017 UTC, (b) 0018-0022 UTC, and (c) 0023-0027 UTC volume scans.

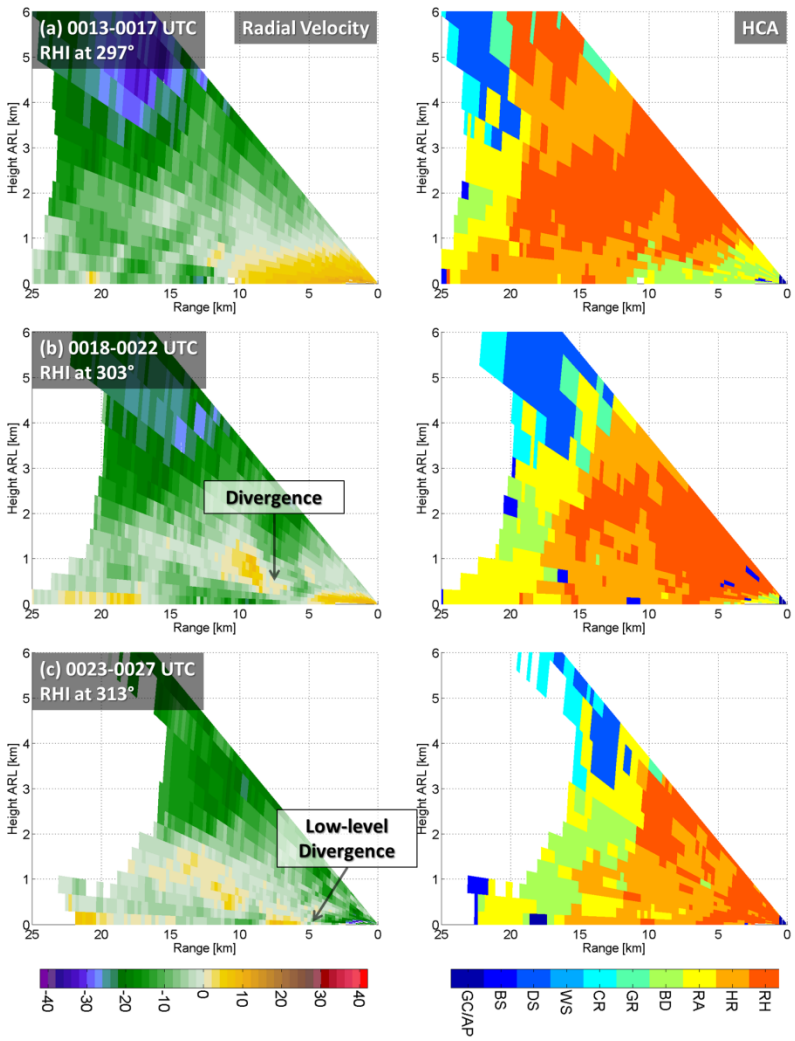


Fig. 5.6. Same panels as Figure 5.2, but at (a) 0013-0017 UTC, (b) 0018-0022 UTC, and (c) 0023-0027 UTC volume scans.

The rain and hail core was located as low as ~0.6 km ARL; the top of the rain and hail core was not sampled due to the radar cone of silence. The radar sampled $Z_H \geq 60$ dBZ, Z_{DR} ~0 dB, and a decrease in ρ_{hv} within the rain and hail core. Outbound V_R became inbound ~11 km downrange from the radar, indicating the presence of low-level radial convergence (~500 m depth), likely associated with the updraft. Evidence of an updraft is suggested by a Z_{DR} column and BWER located above the region of low-level radial convergence.

The rain and hail core began to rapidly descend during the 0018-0022 UTC volume scan (Fig. 5.5b). The HCA output indicates the rain and hail mixture at the lowest elevation scan ~6 km downrange from the radar, which is only ~55 m ARL (Fig. 5.6b). During the rain and hail core's descent, Z_{DR} increased and ρ_{hv} decreased on the bottom periphery of the rain and hail core. The increased Z_{DR} and decreased ρ_{hv} are assumed to be due to the increasing presence of water coating on the descending hailstones (i.e., a torus of water may develop on the hailstones, which may reduce tumbling and increase Z_{DR}). Therefore, it is surmised that there was hail melting in the lower part of the rain and hail core through the combined use of the HCA output and the PRD. Also, there was an area of radial divergence immediately below and within the descending hail core at ~0.4 km ARL. The area of radial divergence was somewhat broad, with near-zero V_R in the center. The near-zero V_R centered within broad divergence implies the flow was more vertical rather than horizontal within this portion of the storm, probably due to the descending downburst. There was still an inflow region, albeit shallower, present in this volume scan. This inflow region was immediately below the region of broad radial divergence, indicating the downburst had not made it to the surface. The HCA output indicates there was a shallow zone of heavy rain, big drops, and rain immediately below the rain and hail mixture region. The outbound V_R had decreased to a maximum estimate of 9 m s^{-1}, implying a decrease in inflow into the storm. This is coincident with a disappearance of the Z_{DR} column from the previous volume scan. The implication of the weakening inflow and the disappearance of the Z_{DR} column is the storm may have become more downdraft rather than updraft dominant (at least on this volume scan).

The downburst was ongoing by the 0023-0027 volume scan (Fig. 5.5c). Note the change in radial convergence at low-levels to radial divergence from the previous volume scan (Fig. 5.6c).

This indicates that the updraft at these lower levels had turned into a downdraft. The maximum inbound V_R was 33 m s^{-1}. Recall the 1-min Mesonet observations (which were nearly collocated with the radar) had detected passage of the gust front at 0025 UTC, which was followed by a peak wind gust of 31.5 m s^{-1} at 0029 UTC (Fig. 4.6). A slight time lag in the surface observations is expected because the downburst began ~5 km downrange (i.e., upstream) from the radar. The HCA output indicates the rain and hail mixture had descended in the immediate vicinity of the radar, implying that the descent of the rain and hail core aloft was coincident with downburst.

5.3 Dual-Doppler Analyses

Dual-Doppler analyses were conducted on the radar data using both KOUN and KTLX WSR-88Ds; however, due to the beam-crossing angle being too small, only two volume scans could be analyzed. The radar data were transformed from the radar coordinate system into a Cartesian coordinate system using National Center for Atmospheric Research's (NCAR) objective analysis software package REORDER (National Center for Atmospheric Research 1995). Once the objective analysis was complete, dual-Doppler analysis was done using NCAR's software package CEDRIC, which conducts its dual-Doppler analysis by finding the projection of the particle motion along the Doppler radar radial direction (National Center for Atmospheric Research 1998). A simple advection correction, using the mean storm motion, was implemented to center the radar data at the 0018 and 0023 for the two dual-Doppler analyses. The 1 km above sea level (ASL) horizontal wind vectors and vertical velocity are overlaid on the 1.45° radar scans and the HCA output in Figure 5.7.

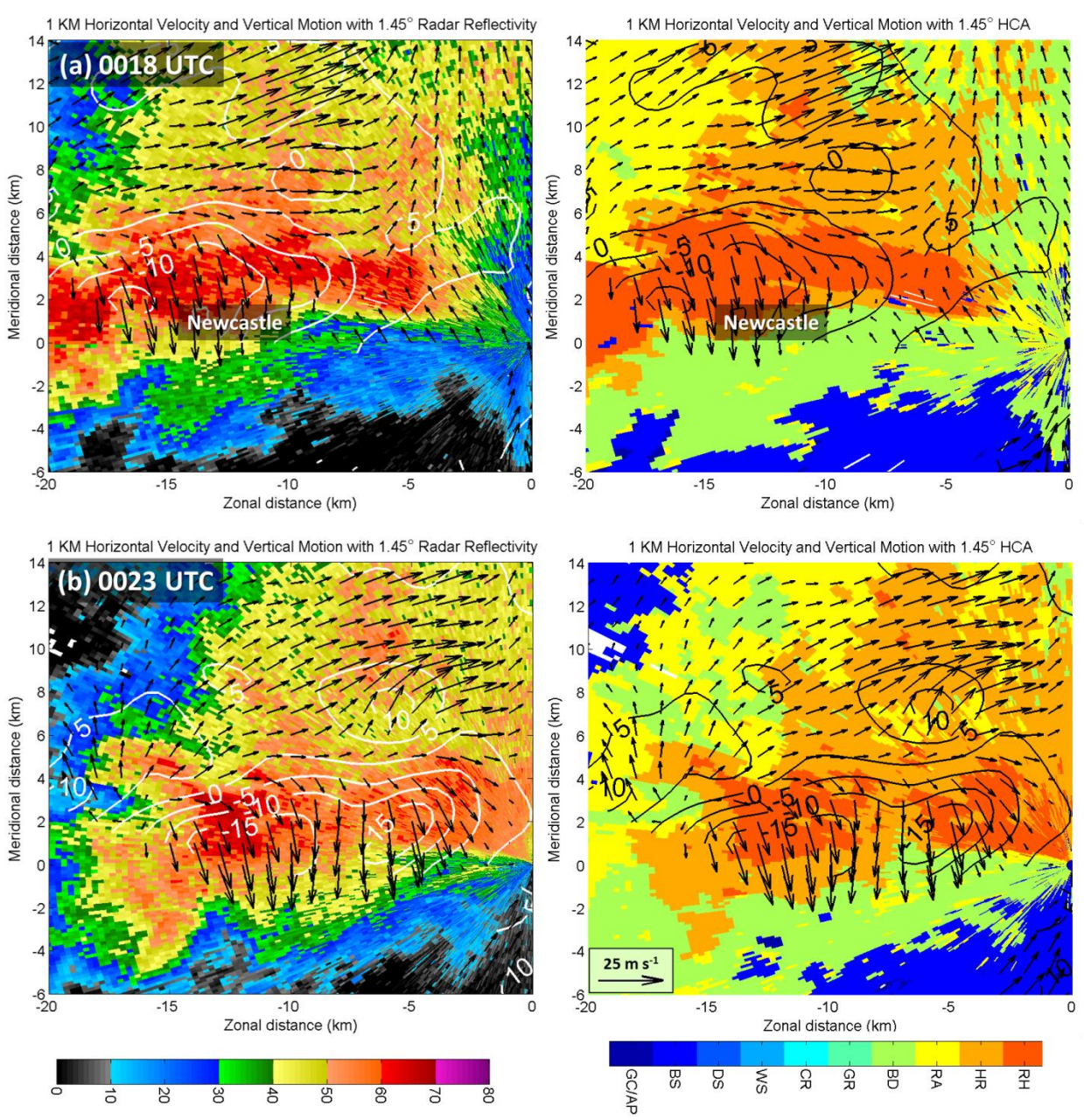


Fig. 5.7. Dual-Doppler analysis at (a) 0018 UTC and (b) 0023 UTC with KOUN 1.45° radar reflectivity and hydrometeor classification algorithm (HCA). Dual-Doppler analysis includes horizontal velocity vectors and vertical velocity contours. Contours are plotted in 5 m s^{-1} intervals in white on the radar reflectivity panels and in black on the HCA panels. The location of Newcastle, Oklahoma, is indicated on panel (a).

The analysis at 0018 UTC (Fig. 5.7a) indicates an elongated storm structure. A minimum vertical velocity of ~ -17 m s^{-1} was present ~17 km west of the radar. There were wind reports

from this storm prior to the reports in Norman, Oklahoma. Approximately 3 km southwest of Newcastle, Oklahoma, there were reports of 31 to 35 m s^{-1} wind gusts between 0020-0023 UTC. Along with the wind gusts, 2.5-cm hailstones were reported as well. Recall there was evidence in the RHI analyses of a possible descending rain and hail core separate from the Norman, Oklahoma, downburst (Fig. 5.3d). The dual-Doppler analysis provides further evidence that this storm was capable of multiple downbursts. The multicellular structure is more evident in the 0023 UTC analysis (Fig. 5.7b). Note the presence of two distinct hail cores with separate vertical motion minima approximately 8 km apart. The development of a multicellular structure was previously noted in the polarimetric observations of two distinct Z_{DR} columns (Fig. 5.3a,b). There was a divergent wind pattern, which is expected near the surface in a downburst. In addition, there was very strong downward motion with a minimum vertical velocity of ~-20 m s^{-1}, which has been previously used to define downbursts (Srivastava 1985). Much of the downward motion in the dual-Doppler analysis was collocated in the rain and hail mixture, which is further confirmation of the wet downburst by radar observations. As previously inferred through the extreme rain rate in the Norman Mesonet observations, this is further evidence that precipitation loading likely had a role in the dynamics of this wet downburst.

5.4 Quantitative Estimate of Surface Mesohigh

Using the Mesonet data from the previous chapter and the vertical velocity from the dual-Doppler analysis, a back of the envelope calculation can be used to estimate the dynamic and thermodynamic contributions to the surface mesohigh. Recall Bernoulli's equation (2.5):

$$p^*_{max} = \frac{1}{\rho_o}\left[\frac{w_d^2}{2} - \frac{g\theta_v^* z}{\theta_{v_o}}\right]$$

For w_d, the dual-Doppler analysis found the maximum downward velocity to be ~-20 m s^{-1}. z is estimated to be ~2 km. This height is just beneath the LCL height of ~2.5 km. ρ_o is assumed to be 1.225 kg m^{-3}. θ_{v_o} and θ_v^* are estimated to be ~307 K (34 °C) and ~-10 K, respectively. For this problem, θ_v^* theoretically needs to include the effect of precipitation loading (which would decrease θ_v^*). However, the effect is likely within the margin of error for this problem since $\theta_v^* \times q_H = 0.2$ K.

Using these values, the estimated contributions from the dynamic and thermodynamic term are ~1.63 hPa and ~5.32 hPa, respectively. The total estimated p_{max}^* is ~7 hPa. This is reasonably close to the 6.6 hPa increase measured by the Mesonet station. From this calculation, it is estimated that the thermodynamic part (i.e., weight of the cold air) had a much greater contribution to the surface mesohigh than the dynamic part.

5.5 Conceptual Model

Figure 5.8 describes the evolution of the microphysics associated with the downburst. Overall, in the early stages of the convective storm (as it was splitting), an area of graupel was developing within the updraft of the storm (Fig. 5.2a). This updraft was detected by the presence of a Z_{DR} column (Fig. 5.1a). The greatest expansion of graupel aloft occurred in early stages of the storm. The large area of graupel was in the cold-cloud region, suggesting graupel embryos were the precursor to hail formation. The area of graupel began to convert to rain and hail mixture (Fig. 5.2b-d). The areal increase of rain and hail mixture aloft from the conversion of graupel was probably due to the intense updraft, as indicated by the persistent, deep Z_{DR} column that had penetrated the 0 °C level (Fig. 5.1a-c). The rain and hail mixture continued to expand significantly above the 0 °C level. Eventually the majority of the graupel evolved into a mixture

of mostly rain and hail (Fig. 5.4). After continued areal expansion, the area of rain and hail mixture eventually descended to the ground. Evidence of the hail core's descent began as early as the 0003-0007 UTC volume scan, nearly 20 to 30 min before there are significant impacts from the downburst (Fig. 5.4c,d); however, the most significant descent occurred after the 0013-0017 UTC volume scan (Fig. 5.6a,b). As it descended to the ground, radial divergence developed immediately below and within the descending hail core (Fig. 5.6b). In addition, evidence of the Z_{DR} column (i.e., the updraft) had dissipated (Fig. 5.5b). Eventually, the downburst reached the surface, as indicated by radial convergence becoming radial divergence on the lowest elevation scan (Fig. 5.6c).

As noted in Chapter 2, studies have shown that ice hydrometeors (i.e., hailstones) can play a significant role in downbursts by increasing the intensity of the downdraft compared to just rain (Atkins and Wakimoto 1991; Fu and Guo 2007; Srivastava 1987). Recall that Fu and Guo (2007) found in their simulated downburst that hail-loading, melting hailstones, and evaporation of rain were crucial in the formation of downbursts within their storm. This observational study on the evolution of hydrometeors and the inferred phase changes using PRD support the importance of these processes in wet downburst formation.

Also noted earlier, the atmosphere was highly conducive for downbursts on this day. Recall that the environmental lapse rate was nearly dry adiabatic in the subcloud layer (Fig. 4.3). For wet downbursts, as the environmental lapse rate increases, lower water content is needed for a downburst (Srivastava 1985); the deep, dry adiabatic layer was probably even sufficient to produce dry downbursts on this day (Proctor 1989; Srivastava 1985; Wakimoto et al. 1994).

The intense rain rate (213 mm hr^{-1}) and the large rain and hail mixture aloft indicate that the storm had relatively high water and ice content. In other words, there was a significant

contribution to q_H (precipitation loading) in the buoyancy equation (2.2). Srivastava (1985) found if the environmental lapse rate is dry adiabatic, the greater the rainfall rate (or Z_H), the more intense the downburst. Therefore, it can be surmised that an observed rapid growth of an expansive rain and hail mixture, as can be revealed by PRD, would indicate imminent risk of a downburst on a day with similar thermodynamic conditions. Note that this was still ~30 min before the downburst caused damage at the surface; therefore, closely monitoring PRD and real-time HCA output can help forecast and warning of strong downbursts in a real-time operational setting.

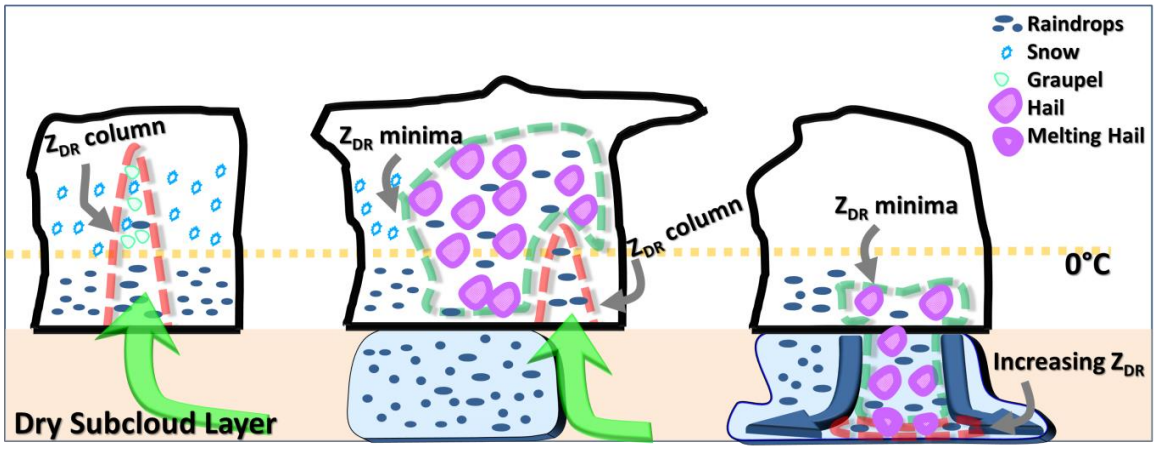


Fig. 5.8. Schematics of the microphysical evolution of hydrometeors during the Norman, Oklahoma, downburst as observed by polarimetric radar data (PRD) and the applied hydrometeor classification algorithm (HCA). The schematics depict raindrops, snow, graupel, hail, and melting hail. Increasing water coating on the melting hailstones is depicted by the increasing line width of the hailstones. The 0 °C level is depicted by the dotted yellow line. Local Z_{DR} maxima (e.g., Z_{DR} columns) are depicted by the dashed red line. Local Z_{DR} minima are depicted by the dashed green line. The updraft and downburst locations are depicted by the green and blue arrows, respectively. Shaded blue region represents the cold pool. It is assumed that diabatic cooling from hail melting and rain evaporation plays an important role in accelerating the downdraft to result in a downburst.

5.6 Summary

Here is a summary of the significant findings from this chapter:

- PRD indicated the presence of a strong updraft, as indicated by a persistent, deep Z_{DR} column that had penetrated the 0°C level. The primary Z_{DR} column had dissipated as the downburst occurred. A secondary Z_{DR} column indicated the presence of a secondary updraft pulse within the multicellular thunderstorm.
- During the early stage, an area of mostly graupel and some rain and hail mix expanded aloft. Eventually, the graupel evolved to nearly all rain and hail mixture above the 0 °C level. This large area of rain and hail mixture descended to the ground during the downburst. Increased Z_{DR} and decreased ρ_{hv} at the bottom of the rain and hail mixture are assumed to be due to the increasing presence of water coating on the descending hailstones (i.e., melting). This demonstrates that melting of hailstones contributed to some of the negative buoyancy in the downburst.
- Dual-Doppler analysis indicates intense downward motion with a minimum vertical velocity of ~-20 m s^{-1}. This downward motion was coincident with rain and hail mixture. Using this value with the Mesonet observations, the estimated contributions for the surface mesohigh from the dynamic and thermodynamic term from Bernoulli's equation are ~1.63 hPa and ~5.32 hPa, respectively.

This chapter shows the important roles polarimetric radars can play in microphysical studies, in particular microphysical processes associated with an intense downburst event. Without the polarimetric observations, it is difficult to determine the dominant hydrometeor types or infer related microphysics processes or updraft strength. With the help of an HCA that

depends on polarimetric radar information, the spatial distributions of microphysical species and their time evolution can be estimated, and the associated microphysical processes inferred. The information from the PRD, combined with dual-Doppler wind retrieval, were able to depict clearly the time evolution of the developing downburst.

Chapter 6 : RaXPol Dual-Pol Observations and Analysis[5]

RaXPol captured the quick expansion of the downburst as it moved to the east-southeast toward Norman with its gust front passing over the radar site. The horizontal and vertical spatiotemporal evolution and structure of the downburst and its associated gust front are the focus of this chapter. The rapid-scan observations captured the development of features such as a horizontal rotor, vertical vortices, multiple gust front heads, and an elevated nose on the leading edge of the gust front. The structure of the downburst is also compared to 1-min Oklahoma Mesonet observations that were nearly collocated with the radar. The analysis period for this chapter is from 0018:50 UTC to 0030:05 UTC.

6.1 Horizontal Evolution and Structure of the Downburst

In this section, the focus is on analyzing the RaXPol observations at its lowest usable elevation angle scan of 3.0°, which can provide insight on the horizontal structure and evolution of the downburst. The downburst had developed to the northwest of RaXPol with the storm moving east-southeastward toward the radar's location. Before analyzing the radar data, it is important to note that the downburst did not appear axisymmetric (i.e., circular) in the radar data near the surface due to two factors. One factor is that the downburst was moving. As noted by Fujita (1985), the storm motion distorts the surface airflow pattern from a circular to elliptical shape. The front-side (relative to storm motion) ground-relative winds increase while the back-side winds decrease in a traveling downburst due to the superposition of the downburst system motion. This results in mostly parallel streamlines or straight-line winds on the leading edge of

[5]Adapted from: Mahale, V. N., G. Zhang, M. Xue, H. B. Bluestein, and J. C. Snyder, 2019: Rapid-scan dual-polarization radar observations of the 14 June 2011 Norman, Oklahoma, downburst and associated gust front and rotor, in-preparation.
Title and year is subject to change.

the gust front. The second factor is the radar estimates the radial component of the ground-relative winds. Initially, the northern and southern parts of the downburst had a large component perpendicular to the radar beam (which would underestimate the true wind speed). Based on the aforementioned factors, the radar would estimate the strongest winds on the southeastern part of the downburst because that part of the thunderstorm had the radar beam parallel to the storm motion and was on the front side of the thunderstorm.

Another consideration is the type of hydrometeors expected to be sampled in the radar data. As previously noted, the 0 °C level was about 4.3 km AGL. At 10 km range, the center height of the 3.0° radar beam is about 0.53 km above radar level (ARL). Therefore, any hydrometers on the 3.0° elevation scan will be raindrops and/or hailstones (i.e., hydrometeors expected with deep, intense moist convection). Because of differential attenuation in Z_{DR} estimates, the most useful parameter to discriminate between pure rain and a mix of rain and hail is ρ_{hv} (used in conjunction with Z_H). At X-band, the probability of hail in a sampling volume increases when ρ_{hv} is $\leq$ ~0.95, collocated with moderate to high Z_H ($\geq$ 40 dBZ) (Snyder et al. 2010). Note that reduction in Z_H due to attenuation will decrease the Z_H below this threshold when there is significant precipitation uprange. The probability of hail increases even more so when ρ_{hv} is $\leq$ ~0.92. This is implied by the probability for pure rain (even in the case of big drops and heavy rain) being low with this value of ρ_{hv}. Therefore, ρ_{hv} will be utilized in this study to track in a quantitative manner precipitation cores containing a mix of rain and hail (henceforth known as mixed-phase precipitation in this chapter). Mixed-phase precipitation cores were found in the previous chapter through the analysis of S-band polarimetric radar data and application of a HCA to the data. Note that any hail would be melting hail with some percentage of fractional water content because of the hail falling into an environment that is above freezing.

The first 3.0° elevation scan of radar data collected by RaXPol was at 0018:50 UTC (Fig. 6.1a), which was prior to the occurrence of the downburst. The elevation scan had a broad area of inbound V_R associated with the downdraft portion of the thunderstorm. The magnitudes of these V_R estimates were generally $\leq$ 10 m s^{-1}. There was moderate to high Z_H (40-55 dBZ) collocated with downdraft, indicating the location of the precipitation core. There were at least two distinct areas of the reduced ρ_{hv} ($\leq$ 0.85) within this area of Z_H. These areas of reduced ρ_{hv} were collocated with moderate to high Z_H, which indicates the likely existence of mixed-phase precipitation near the surface.

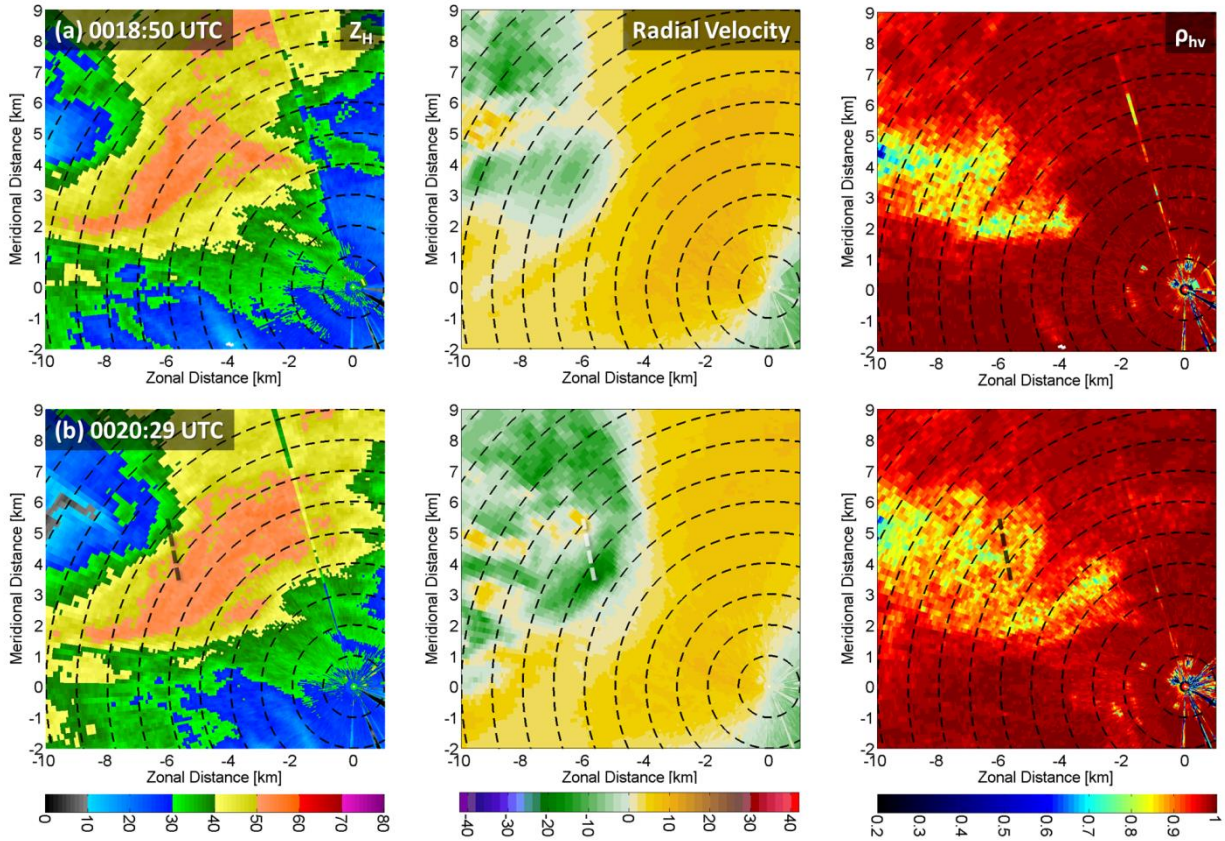


Fig. 6.1. Horizontal radar reflectivity (Z_H; dBZ), radial velocity (V_R; m s^{-1}), and co-polar correlation coefficient (ρ_{hv}) at 3.0° elevation angle are shown at (a) 0018:50 UTC and (b) 0020:29 UTC. The dotted line (white on V_R; black on Z_H and ρ_{hv}) is the distance between the maximum inbound velocity on the southeastern part of the storm and the maximum outbound velocity on the northern part of the storm. 1 km range rings and axes are labeled relative to RaXPol's location.

By the 0020:29 UTC 3.0° elevation scan (Fig. 6.1b), the downdraft had intensified. The maximum inbound V_R had increased to 23 m s^{-1}, which is near NWS severe thunderstorm warning criteria ($\geq$ 26 m s^{-1} wind gust at the surface) (National Weather Service 2018). Based on the marked increase in the inbound V_R, the near severe magnitude of the inbound V_R, and the appearance of an outbound V_R maximum to the north-northwest of this location (as part of the near surface radially divergent flows), a downburst was likely occurring in this area (~7 to 8 km to the northwest of RaXPol's location). There was an area of reduced ρ_{hv} centered between these localized wind maxima (i.e., the approximate center of the downburst), suggesting that a descending mixed-phase precipitation core was a significant contributor to the downburst through precipitation loading and/or melting of hailstones. Evaporation may have initially contributed as well, but note that this downburst began well-behind the leading edge of precipitation, so the environment may have been close to saturation. When compared to the previous elevation scan, it may appear that this mixed-phase precipitation had advected eastward (i.e., primarily in the horizontal); however, note that it was actually the downdraft region that was moving eastward with new mixed-phase hydrometeors descending to the lowest elevation scan (replacing the previous hydrometeors). Analysis through the vertical evolution and structure the downburst will provide more insight on this in the next section. Attenuation resulted in the underestimation of Z_H in this area, which is expected with heavy rain and hail uprange. Ahead of the downburst, there was another area of reduced ρ_{hv} (~4 to 5 km to the northwest of RaXPol's location), which indicates that mixed-phase precipitation was likely occurring in this part of the thunderstorm as well.

As a proxy for the approximate size (i.e., horizontal scale) of the downburst, the distance between the maximum inbound V_R on the southeastern part of the storm and the maximum

outbound V_R on the northern part of the storm can be measured on this scan and tracked in subsequent scans. Using the method, it is reasonable to assume that the downburst was *at least* this size in horizontal scale. At this time, the distance between the maximum inbound V_R on the southeastern part of the storm (23 m s^{-1}) and the maximum outbound V_R on the northern part of the storm (6 m s^{-1}) was ~2.1 km, corresponding to the size of a microburst.

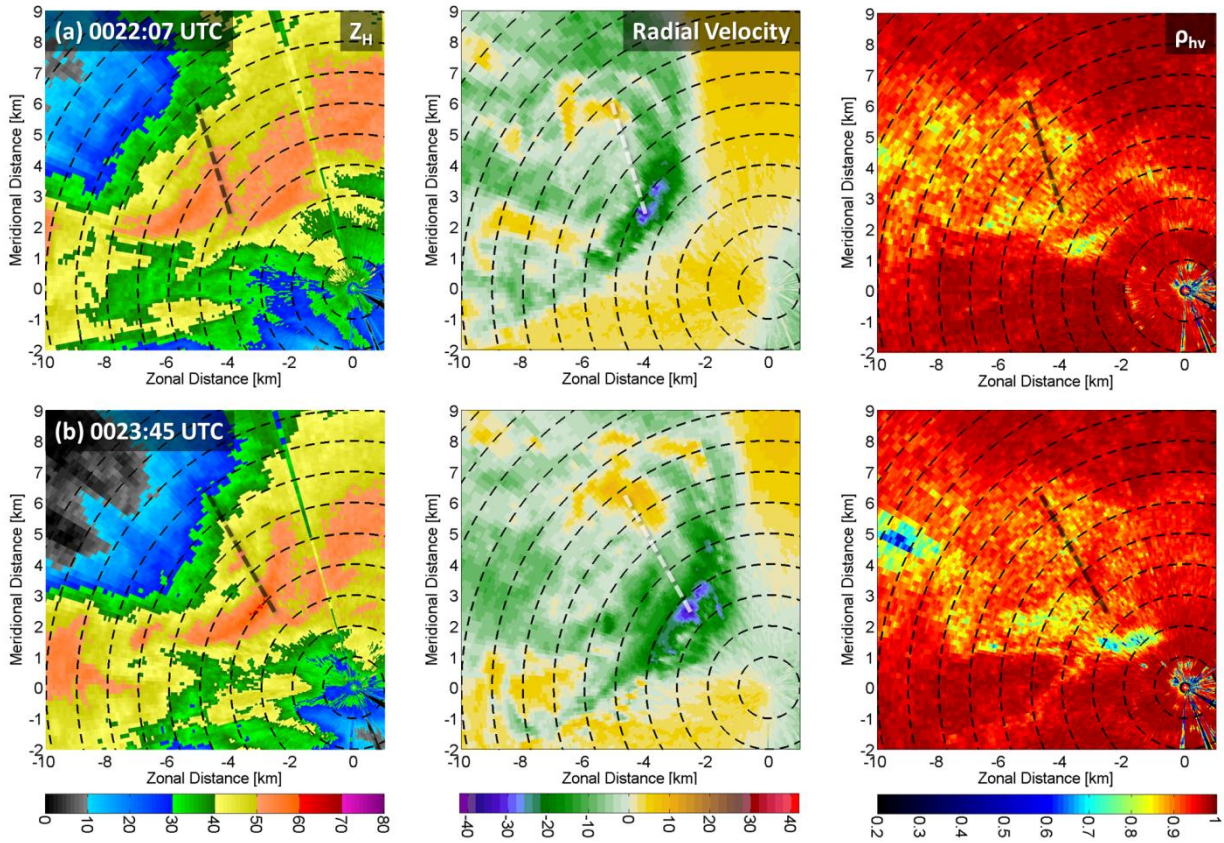


Fig. 6.2. Same panels as Figure 6.1, but 3.0° elevation angle at (a) 0022:07 UTC and (b) 0023:45 UTC.

By 0022:07 UTC 3.0° elevation scan (Fig. 6.2a), the distance between the maximum inbound V_R on the southeastern part of the storm (34 m s^{-1}) and the maximum outbound V_R on the northern part of the storm (11 m s^{-1}) had increased to ~3.6 km. As the cold pool spread outward, the horizontal winds associated with the downburst had accelerated. The elliptical,

asymmetric shape of the traveling downburst is evident in the V_R pattern; the front-side winds on the eastern side of the downburst, immediately behind the gust front, were the most intense. There was still an area of reduced ρ_{hv} along and behind the gust front. There was $\rho_{hv} \leq 0.85$ with some embedded areas ~0.75, which indicates that mixed-phase precipitation was still descending to the surface even after the downburst had commenced. Continued precipitation loading may explain why the downburst's horizontal winds had intensified between 0020:29 and 0022:07 UTC (even with the ~75% increase in horizontal scale). There was also an area of reduced ρ_{hv} ahead of the gust front (~3 to 4 km to the northwest of RaXPol's location).

By the 0023:45 UTC 3.0° elevation scan (Fig. 6.2b), the distance between the maximum inbound V_R on the southeastern part of the storm (33 m s^{-1}) and the maximum outbound V_R on the northern part of the storm (10 m s^{-1}) had increased further to ~4.7 km. By horizontal scale, this downburst was now a macroburst event. The leading edge of the gust front was ~3 to 4 km to the northwest of RaXPol's location. There continued to be an area of reduced ρ_{hv} along and behind the gust front. Moderate to high Z_H (40-60+ dBZ) was associated with this reduced ρ_{hv}, which suggests there was continued mixed-phase precipitation loading. There also continued to be another area of reduced ρ_{hv} ahead of the gust front. The Z_H was lower (~35-45 dBZ) in this area of reduced ρ_{hv}. The relatively lower Z_H was not due to attenuation, as indicated by higher Z_H downrange and no significant precipitation uprange. Therefore, it is assumed the quantity of precipitation was less (fewer hailstones and raindrops) in the leading convection. In addition, depending on the characteristics of the hail (i.e., canting angle and fractional water content), there are cases where hail may not result in as high Z_H due to resonance effects at X-band (e.g., Snyder et al. 2010). While there was a gap in the reduced ρ_{hv} at low-levels, there was no visible gap aloft at higher elevation scans (not shown). The strong upward motion at the gust front is

believed to be the cause of this zone of reduced ρ_{hv} gap, as will be discussed in more detail in the next section.

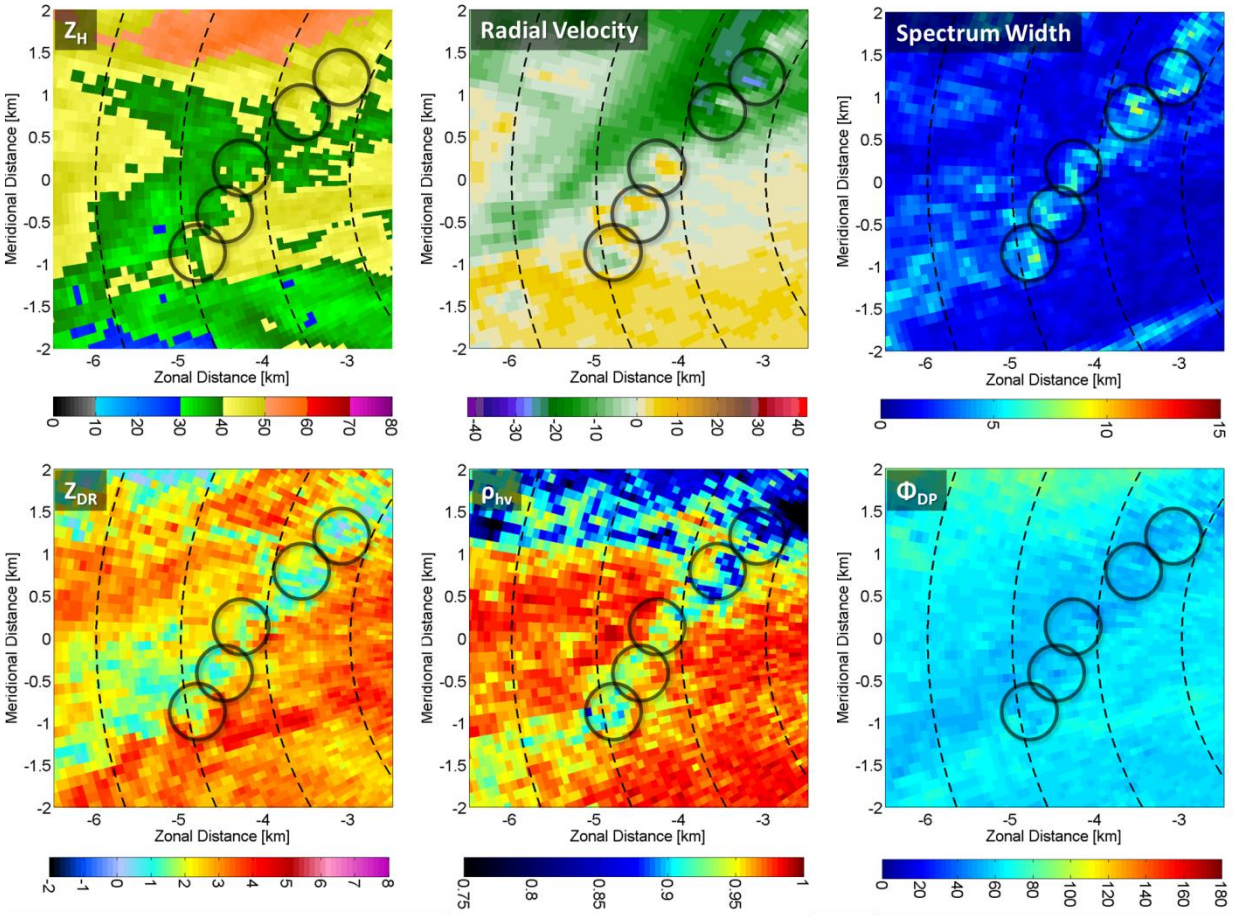


Fig. 6.3. 0023:45 UTC horizontal radar reflectivity (Z_H; dBZ), radial velocity (V_R; m s^{-1}), spectrum width (σ_v; m s^{-1}), differential reflectivity (Z_{DR}; dB), co-polar correlation coefficient (ρ_{hv}) and differential phase (ϕ_{DP}; degrees) at 3.0° elevation angle. Vertical vortices are circled in black. 1 km range rings and axes are labeled relative to RaXPol's location.

There was a line of small vertical vortices along the leading edge of the gust front showing up as positive-negative V_R couplets. Vertical vortices have been found along a rear-flank gust front in a supercell using W-band Doppler radar observations (Bluestein et al. 2003). Figure 6.3 is a zoomed-in view of the southwest part of the gust front with a different color scale for ρ_{hv} that emphasizes values ≤0.95. In addition to Z_H, V_R, and ρ_{hv}, Z_{DR}, ϕ_{DP}, and σ_v are shown.

Since this is the leading edge of the thunderstorm with no heavy rain or hail core uprange, it is assumed that differential attenuation was minimal (especially since Z_{DR} increased markedly immediately behind the gust front). These vertical vortices did have vertical continuity as they were present in higher elevation scans through ~15°, which is ~1.1 to 1.3 km AGL (not shown). It is somewhat subtle, but there was a slight reduction in ρ_{hv} (~0.87-0.95) along this line of vertical vortices. This reduction was most pronounced along the southwest part of the gust front (southwest of the reduced ρ_{hv} associated with the mixed-phase precipitation). There were localized minima in ρ_{hv} coincident with some of these V_R couplets. This slight reduction of ρ_{hv} may have occurred due to the presence of some non-meteorological hydrometeors (e.g., dust) being lofted by the vortices or the gust the front. Bluestein et al. (2003) found localized Z_H minima, known as weakecho holes, associated with the line of vortices in their study (c.f. 10 in Bluestein et al. 2003). For the three southwest-most vortices, there may have been subtle, localized minima of reflectivity. There was a reduction of Z_{DR} (~0 to 1 dB) along this line as well, which indicates the presence of smaller and/or more spherical targets in the sampling volume (e.g., small raindrops and/or dust), perhaps due to centrifuging. Relatively high σ_v along the gust front indicates the presence of turbulence, which is expected along a horizontal shear zone. There were local maxima (~7 to 8 m s^{-1}) embedded within this line of enhanced σ_v that were collocated with the velocity couplets. These vertical vortices were relatively small in diameter, but may have corresponded to small gustnadoes.

There were still vertical vortices along the leading edge of the gust front on the 0025:23 UTC 3.0° elevation scan (Fig. 6.4a), which were coincident with a slight reduction in ρ_{hv}. The distance between the highest inbound V_R on the southeast part of the storm (34 m s^{-1}) and the highest outbound V_R on the northern part of the storm (~15 m s^{-1}) had increased further to ~5.9

km; the intensity of the winds remained steady with continued expansion in size. A new mixed-phase precipitation core was located ~5 to 6 km to the west-northwest from the RaXPol location (immediately behind the other two cores).

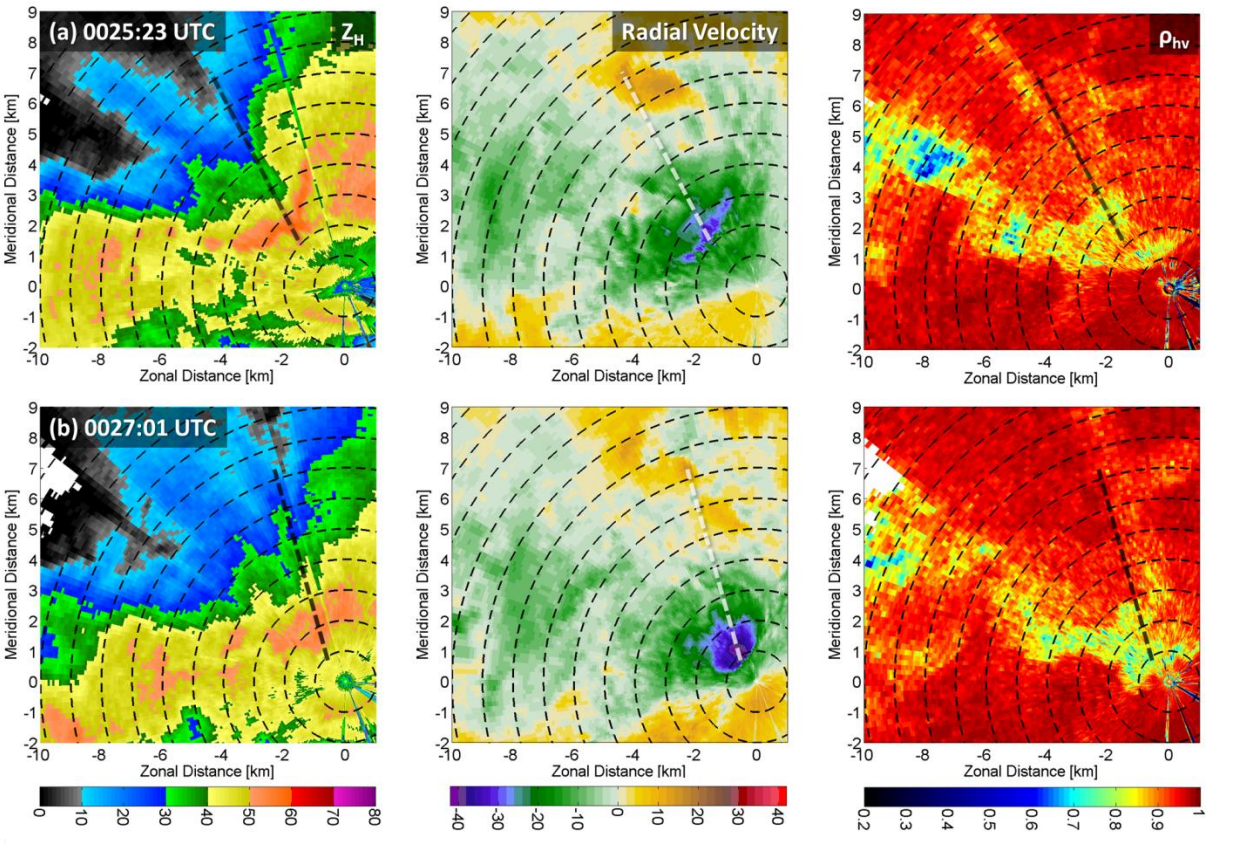


Fig. 6.4. Same panels as Figure 2, but 3.0° elevation angle at (a) 0025:23 UTC and (b) 0027:01 UTC.

On the 0027:01 UTC 3.0° elevation scan (Fig. 6.4b), there was a nearly continuous line of mixed-phase precipitation from just northwest of the RaXPol location to ~6 km west-northwest. The ρ_{hv} within this area was ≤ 0.80. The separate cores in the previous scan had consolidated. The distance between the highest inbound V_R on the southeast part of the storm (42 m s^{-1}) and the highest outbound V_R on the northern part of the storm (15 m s^{-1}) had increased further to ~6.4 km Using the low-level V_R as a proxy for intensity, it is evident that the

downburst had intensified markedly from the previous scan. The line of vertical vortices had become ill-defined during this scan. The leading edge of the most intense winds had accelerated southeastward, which may have undercut the vortices. As previously noted, it is hypothesized that continued precipitation loading may explain why the downburst's horizontal winds had continued to intensify. This was the last scan before RaXPol was directly impacted by the downburst. Therefore, this will be the last scan analyzed in the context of the horizontal structure and evolution (a subsequent volume scan will be shown in the next section).

Overall, the rapid-scan updates captured how quickly the downburst had grown in size as it moved to the east-southeast. Figure 6.5 is a summary of the downburst's spatiotemporal evolution. It had grown from a microburst at ~2.1 km horizontal scale to a macroburst at ~4.7 km in ~3 min. Even with continued expansion in size to ~6.4 km, the downburst's near-surface horizontal winds intensified from 23 m s^{-1} to 42 m s^{-1} (assuming the true ground-relative winds were nearly parallel to radar beam on the southeastern part of the storm). Note there was a continued area of mixed-phase precipitation collocated with the approximate center of the downburst. In the next section, the vertical structure and evolution the downburst will be analyzed.

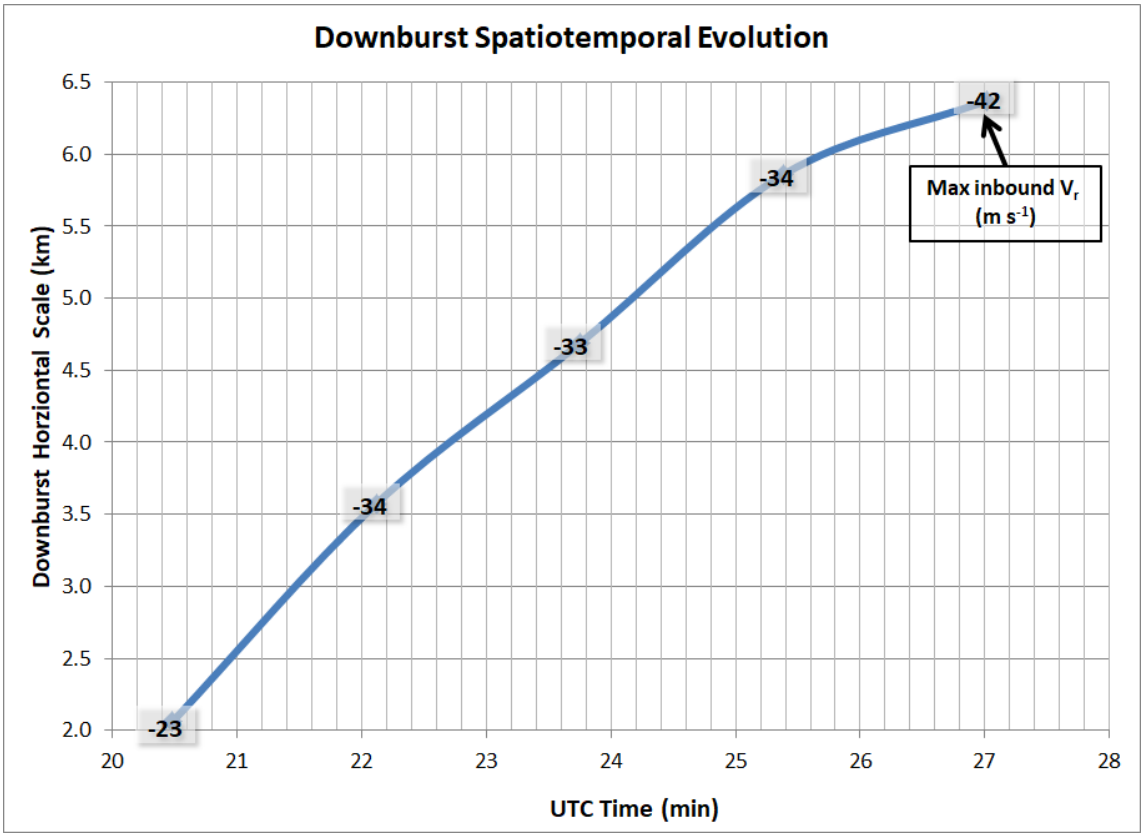


Fig. 6.5. The downburst's spatiotemporal evolution between 0020:29 and 0027:01 UTC. The downburst's horizontal scale is shown with respect to time and maximum inbound radial velocity (V_r). The downburst grew in horizontal scale from at least 2.1 km to 6.4 km in less than 7 min, changing based on size from a microburst to a macroburst while intensifying.

6.2 Vertical Structure and Evolution of the Downburst

The previous section focused on the horizontal structure and evolution of the downburst. In this section, reconstructed RHIs from each volume scan were created to conduct storm-scale analysis on the vertical structure and evolution of the downburst. This includes features such as the gust front and the attendant rotor. The vertical structure is important because it can provide more insight on the mechanism for the formation of the downburst.

An important consideration was what azimuth to select for reconstructed RHIs. After viewing several reconstructed RHIs, the azimuth selected was ~310°. This azimuth was chosen because it was approximately parallel to the direction of the storm motion vector (i.e., it would have a large component of winds parallel to the radar beam) and because it best captured some unique features associated with the gust front and downburst (e.g., rotor). Note that because the storm motion was not completely parallel to the RHI (and the motion was not steady state), it cannot be assumed that precipitation was only moving in the vertical or along the RHI (i.e., there was some horizontal, cross-azimuth motion of precipitation). For example, when it is noted in the analysis that a precipitation core is descending, the assumption is *most* of the motion is in the vertical.

When creating the RHIs, the closest azimuth to 310° for each elevation scan was used. Due to the data quality issues previously noted in Chapter 3, reconstructed RHIs used elevation scans from 3.0° to 27.0°. Note that because these RHIs are reconstructed from PPI data, each elevation of data in the reconstructed RHI is ~6 to 7 sec after the previous elevation. As in the previous chapter, no objective analysis scheme was used when creating the RHIs.

The first volume scan of radar data collected by RaXPol was from 0018:50-0020:16 UTC. During this volume scan (Fig. 6.6a), the thunderstorm was in the mature stage and somewhat tilted with a Z_H overhang ~4 km downrange. There was a relatively large area of outbound radial V_R from RaXPol's location to ~6.8 km downrange (where the V_R became inbound), which represented the inflow into the thunderstorm. The maximum depth of this inflow region was at least ~1.3 km. The leading edge of the inflow region was the location of the wind shift (i.e., gust front) and the transition zone from the updraft to the downdraft part of the thunderstorm. As previously noted, the inbound V_R within the downdraft region were ≤ 10 m s^{-1};

therefore, it is assumed that the downdraft was quite weak during this volume scan. Within and above this downdraft region, there was a large area of the reduced ρ_{hv} ($\leq$ 0.85) that was collocated with higher Z_H (45-50+ dBZ) from the lowest elevation scan to the highest elevation scan. Since this column of reduced ρ_{hv} was $\leq$ ~3.5 km ARL, it is assumed all of this reduction of ρ_{hv} was due to a mixed-phase precipitation.

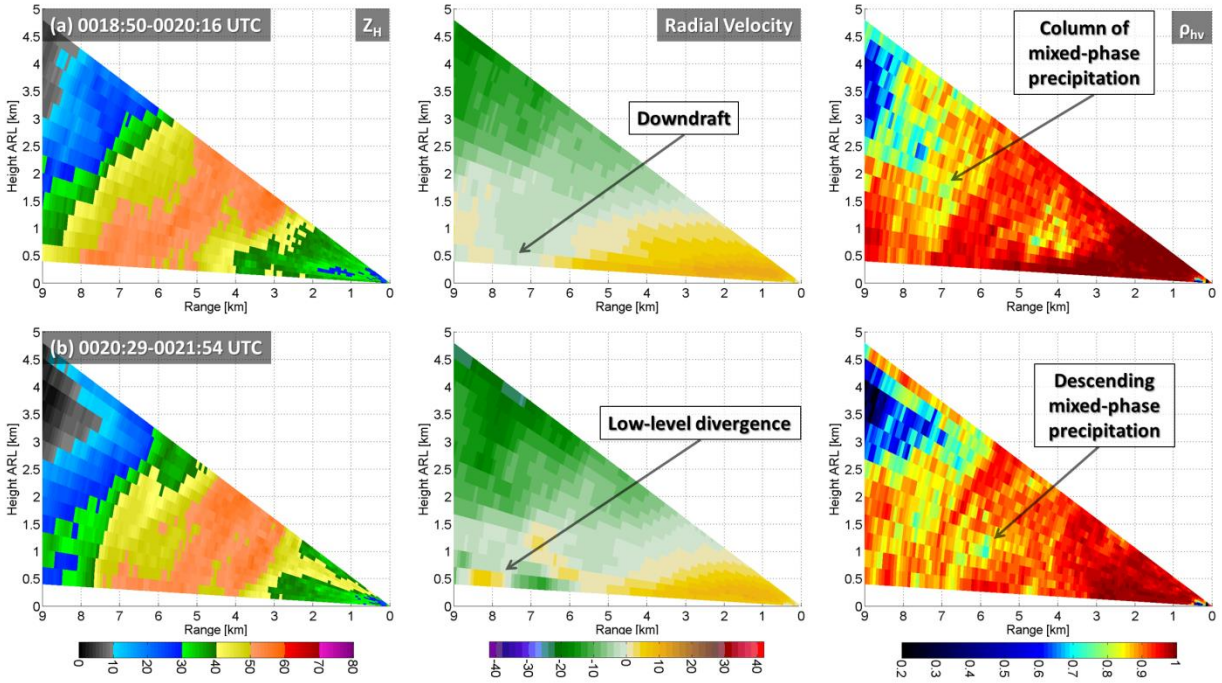


Fig. 6.6. Reconstructed range height indicator (RHI) from RaXPol at ~310° azimuth. Horizontal radar reflectivity (Z_H; dBZ), radial velocity (m s^{-1}), and co-polar correlation coefficient (ρ_{hv}) volume scans are shown at (a) 0018:50-0020:16 UTC and (b) 0020:29-0021:54 UTC. Axes are labeled relative to RaXPol's location. Noteworthy storm features are denoted.

On the backside of the thunderstorm, beginning at ~7.6 km downrange and ~2.5 km ARL (and continuing farther downrange), the streaky, reduced ρ_{hv} coincident with low Z_H ($\leq$ 30 dBZ) was likely due to nonuniform beam filling and/or three-body scattering. Nonuniform beam filling occurs due to cross-beam gradients of Z_H, Z_{DR}, and/or ϕ_{DP} (Ryzhkov 2007). This may occur due

to a vertical gradient in hydrometeors in the radar beam and results in a reduction of ρ_{hv} downrange (e.g., Snyder et al. 2013; Warning Decision Training Division 2018). Three-body scattering is attributed to non-Rayleigh (i.e., Mie or resonance) scattering from a region of hydrometeors made up of spongy ice spheres (i.e., wet hail) (Zrnić 1987) and is seen in radar data as a "spike" in Z_H coincident with low ρ_{hv} downrange from hail aloft (e.g., Mahale et al. 2014). For this event, attenuation makes it difficult to discern three-body scattering as there is no evidence of a spike in Z_H downrange (even though ρ_{hv} continues to decrease downrange). In either scenario, nonuniform beam filling or three-body scattering would occur due to the presence of hail in the thunderstorm aloft (which further substantiates that the reduced ρ_{hv} collocated with the higher Z_H was due to mixed-phase precipitation aloft).

By the 0020:29-0021:54 UTC volume scan (Fig. 6.6b), the reduced ρ_{hv} aloft had descended with a ρ_{hv} estimate of 0.80 at ~7.6 km downrange and ~0.3 km ARL. Even lower ρ_{hv} was estimated higher in the thunderstorm; a ρ_{hv} estimate as low as 0.71 with moderate Z_H ($\geq$ 45 dBZ) was located ~5.9 km downrange and ~0.9 km ARL. Note that with the thunderstorm moving toward the radar, in addition to descending, the reduced ρ_{hv} aloft had also moved uprange. There was also a divergence signature on the lowest elevation scan within the area of descending, reduced ρ_{hv}. Within the divergence signature, ~7.5 km downrange, the maximum inbound and outbound radial V_R were estimated at 13 m s^{-1} and 5 m s^{-1}, respectively. The divergence signature at low-levels represents the thunderstorm's downdraft impinging on the surface, which causes winds to diverge from its center. The gust front was uprange from the divergence signature, ~5.7 km downrange from the radar. Uprange from the gust front, there was still a well-defined inflow region with maximum outbound V_R at 10 m s^{-1}. Overall, the increased inbound V_R and the divergence signature indicate that the downdraft had intensified from the

previous volume scan; however, the strength of the downdraft (using the horizontal, near-surface winds as a proxy), was not sufficient to produce severe weather (as noted in the previous section). It can be surmised that precipitation loading and/or melting hail was important for driving the initial downdraft due to descending area of reduced ρ_{hv} associated with the downdraft.

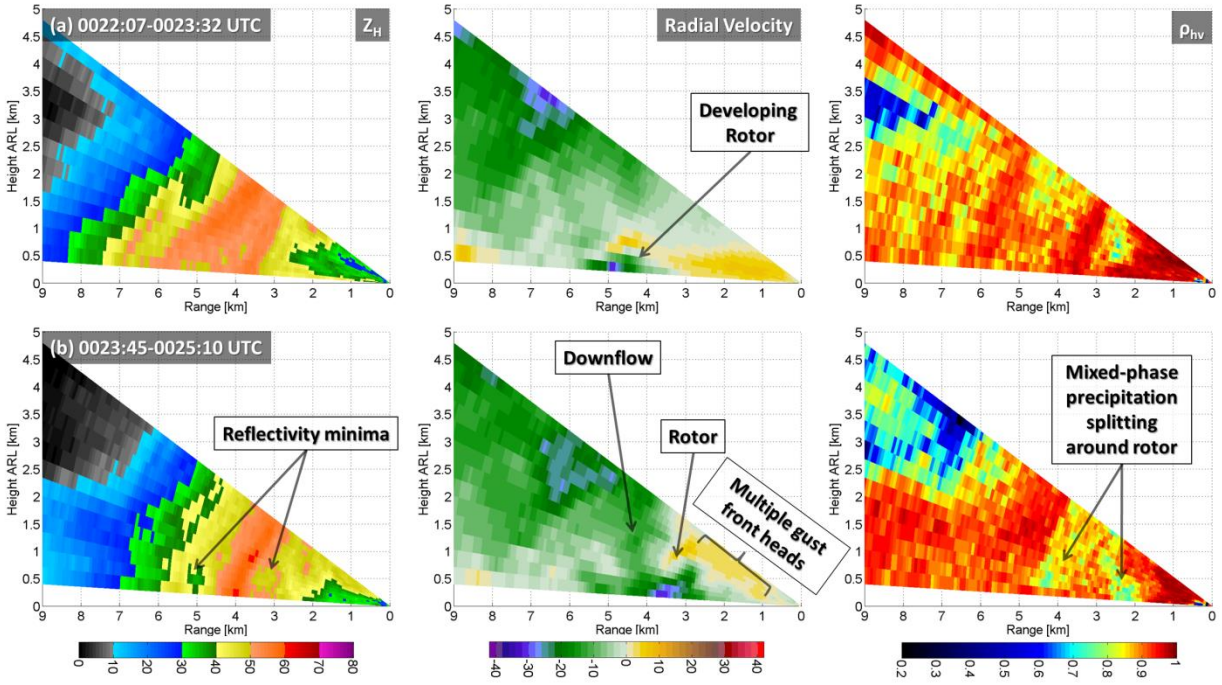


Fig. 6.7. Same panels as Figure 6.5, but volume scans at (a) 0022:07-0023:32 UTC and (b) 0023:45-0025:10 UTC.

By the 0022:07-0023:32 UTC volume scan (Fig. 6.7a), the magnitude of the maximum inbound and outbound V_R had increased and were estimated at 30 m s^{-1} and 8 m s^{-1}, respectively. The distance between these velocities had also increased to ~4 km. The gust front was now ~3.1 km downrange. The maximum inbound V_R of 30 m s^{-1} (58 knots) indicates that the horizontal winds in the downburst were intense enough to produce severe weather and were likely affecting the surface since the radar estimated winds were only ~0.21 km ARL. In addition, an area of

horizontal vorticity (i.e., a rotor) had developed at the same distance (~4.8 km downrange) from the radar (as indicated by the velocity couplet). The top of the rotor was ~1 km ARL. The rotor had developed as accelerating outflow winds undercut the inflow into the thunderstorm (i.e., the maximum inbound V_R had increased by 18 m s^{-1} from the previous volume scan). Baroclinic generation of horizontal vorticity due to a horizontal buoyance gradient (from the temperature contrast between cold outflow and warm inflow regions) should have contributed to the generation of the rotor (e.g., Rotunno and Klemp 1985; Rotunno et al. 1988).

It is assumed the mixed-phase precipitation core aloft (indicated by the reduced ρ_{hv} at ~0.90 km ARL on the previous volume scan) had descended to the surface, resulting in strengthening of the downburst. However, a new area of reduced ρ_{hv} (≤ 0.85) aloft was located above the ongoing downburst. This area of reduced ρ_{hv} was ~1.5 km in length and at least 1 km deep. There was also another area of reduced ρ_{hv} ahead of the downburst at ~2.5 km downrange. Therefore, even with the descent of a mixed-phase core of precipitation to the surface, there was a new core aloft (i.e., precipitation loading from a mix of rain and melting hail continued to be an integral factor in the ongoing downburst event).

By the 0023:45-0025:10 UTC volume scan (Fig. 6.7b), the rotor had grown vertically and horizontally. The magnitude of the maximum inbound V_R had increased slightly to 32 m s^{-1} at ~3.6 km downrange. The rotor and its associated maximum inbound V_R were located ~2.2 to 2.7 km behind the initial wind shift. To the left of the rotor, there was a narrow, vertical column of inbound V_R with magnitudes that were somewhat constant at ~12 to 14 m s^{-1}. Note that because the thunderstorm was moving toward the radar, if the magnitude of the storm motion is assumed to be approximately the same as the V_R in the column, the column's storm-relative velocity would be around zero. Therefore, this column is assumed to be a radar representation of a

downburst (i.e., the downflow region). The areas of reduced ρ_{hv} from the previous scan had descended. On the leading edge of the thunderstorm, ahead of the rotor, the mixed-phase precipitation was likely reaching the surface with a ρ_{hv} estimate of 0.72 at ~2.1 km downrange and only 94 m ARL. Hail was observed prior to the arrival of the gust front and associated intense winds at RaXPol's location (R. Tanamachi 2019, personal communication).

The circulation associated with the rotor and/or upward motion associated with the gust front may have split the hail core into two segments as indicated by the reduced ρ_{hv} separating around the rotor. There was even a slight, circular reduction of Z_H in vicinity of the rotor (slightly displaced lower than the rotor's center). One potential hypothesis is less precipitation may have been able to descend into this location due to the circulation associated with the rotor. The split of the ρ_{hv} in the rotor supports this hypothesis as there is evidence that the mixed-phase core of precipitation was splitting into two segments.

On the next volume scan at 0025:23-0026:48 UTC (Fig. 6.8a), the magnitude of the maximum inbound V_R had remained steady at 31 m s^{-1} at ~2.2 km downrange. The rotor became a bit ill-defined during this volume scan; however, less of the thunderstorm in the area of interest was sampled aloft owing to the radar cone of silence (i.e., data only to ~1.2 km ARL were collected above the maximum V_R). Nevertheless, there is some evidence there was at least a remnant rotor with a broad velocity couplet centered ~1.7 km downrange and ~0.6 km ARL. There was a large area of reduced ρ_{hv} nearly collocated (with respect to range) with the highest inbound V_R estimates. This area of reduced ρ_{hv} was ~0.8 to 3.5 km downrange from the radar (i.e., ~2.7 km length) and was present from the lowest elevation scan to the highest elevation scan at this location (i.e., at least ~1.9 km depth at ~3.5 km range). Within this broad area, there were ρ_{hv} estimates $\leq$ 0.70 with some as low as 0.64. As occurred previously, even with an

ongoing downburst with damaging winds at the surface, precipitation loading had continued in the thunderstorm with descending surges of mixed-phase precipitation cores.

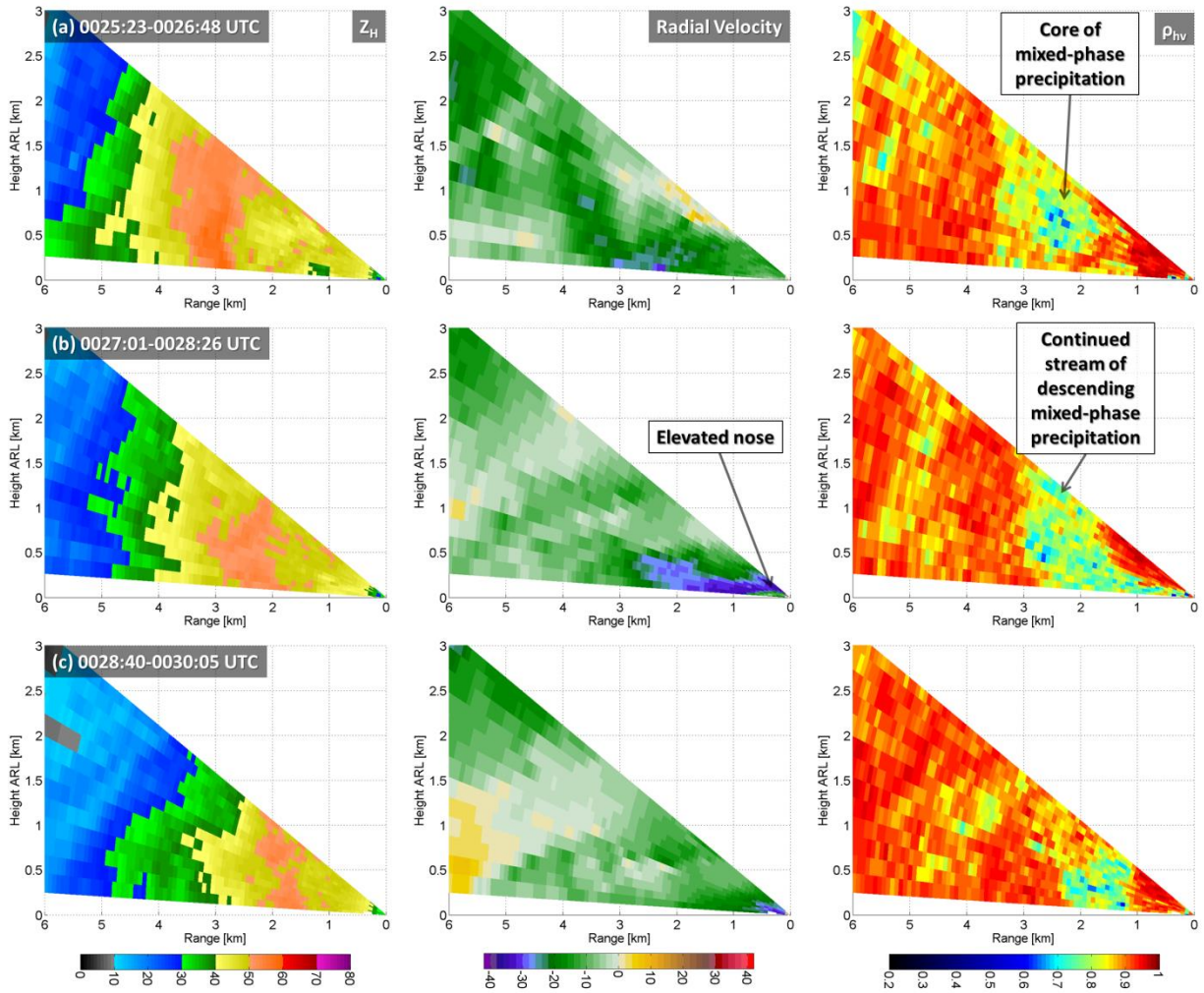


Fig. 6.8. Same panels as Figure 6.5, but volume scans at (a) 0025:23-0026:48 UTC, (b) 0027:01-0028:26 UTC, and (c) 0028:40-0030:05 UTC.

By the 0027:01-0028:26 UTC volume scan (Fig. 6.8b), the magnitude of the maximum inbound V_R had increased to 36 m s^{-1}. The large area of reduced ρ_{hv} had descended to the lowest elevation scan with a > 2.5 km length of $\rho_{hv} \leq 0.85$ collocated with moderate to high Z_H (40 to 50+ dBZ). Even with descent to the surface, the area of reduced ρ_{hv} continued to be present at the highest elevation scan above the most intense winds (i.e., there was a continued stream of

descending mixed-phase precipitation aloft). The continued stream of descending rain and melting hail aloft may explain the strengthening of the downburst's winds during this particular volume scan. In addition, there was another column of mixed-phase precipitation ~5 km downrange from the radar. There was an elevated bulge on the head of the gust front in the velocity data. Sometimes referred as the "nose of the gust front" (e.g., Goff 1976; Klingle et al. 1987), this feature occurs due to flow moving faster above the near-surface friction layer. For this case, the depth was quite shallow with a peak height for the bottom of the nose ~75 m ARL.

By the 0028:40-0030:05 UTC volume scan (Fig. 6.8c), RaXPol was directly impacted by the downburst with an estimated 34 m s^{-1} maximum inbound V_R. There continued to be a column of mixed-phase precipitation with ρ_{hv} estimates $\leq$ 0.70 collocated with moderate to high Z_H (40 to 50+ dBZ) ~1 to 2 km downrange from RaXPol's location. Farther downrange (~5.6 km), there was a low-level divergence signature associated with the other descending core of mixed-phase precipitation. This divergence signature may indicate another downburst was occurring. The Mesonet observations in Chapter 4 documented additional surges of wind that would impact the Mesonet site located 221 m to the southwest of RaXPol's location.

Overall, the rapid-scan updates of the vertical evolution and structure of the downburst provided evidence that surges of mixed-phase precipitation cores aloft—indicated by reduced ρ_{hv}— descended to surface. These surges of descending precipitation indicate surges in the downburst. For this downburst event, surface winds (using the lowest elevation maximum inbound velocity as a proxy) gradually increased and remained somewhat steady-state. The absence of weakening (and in some cases strengthening) may be due to continued stream of hydrometeors for precipitation loading and melting of hailstones and attendant downburst surges.

The largest increase happened between 0020:29 and 0022:07 UTC, when the maximum inbound V_R increased by 17 m s^{-1}.

6.3 Comparison to 1-min Mesonet Data

Since the orientation of the gust front as it approached RaXPol was northeast to southwest, RaXPol and the Norman Oklahoma Mesonet site experienced the impacts from the downburst at approximately the same time. Since the Mesonet collected observations every minute, it provides an excellent data set to compare to RaXpol's rapid scan data.

Figure 6.9a is a plot of the Mesonet 1-min maximum wind gust and wind direction at 10-m along with RaXPol volume scan times detailed in the previous section. Figure 6.9b is a plot of the Mesonet 1-min surface pressure and temperature at 2 m. The volume scan times correspond to the starting time of the 3.0° (lowest) elevation scan because that provides the closest height for comparison.

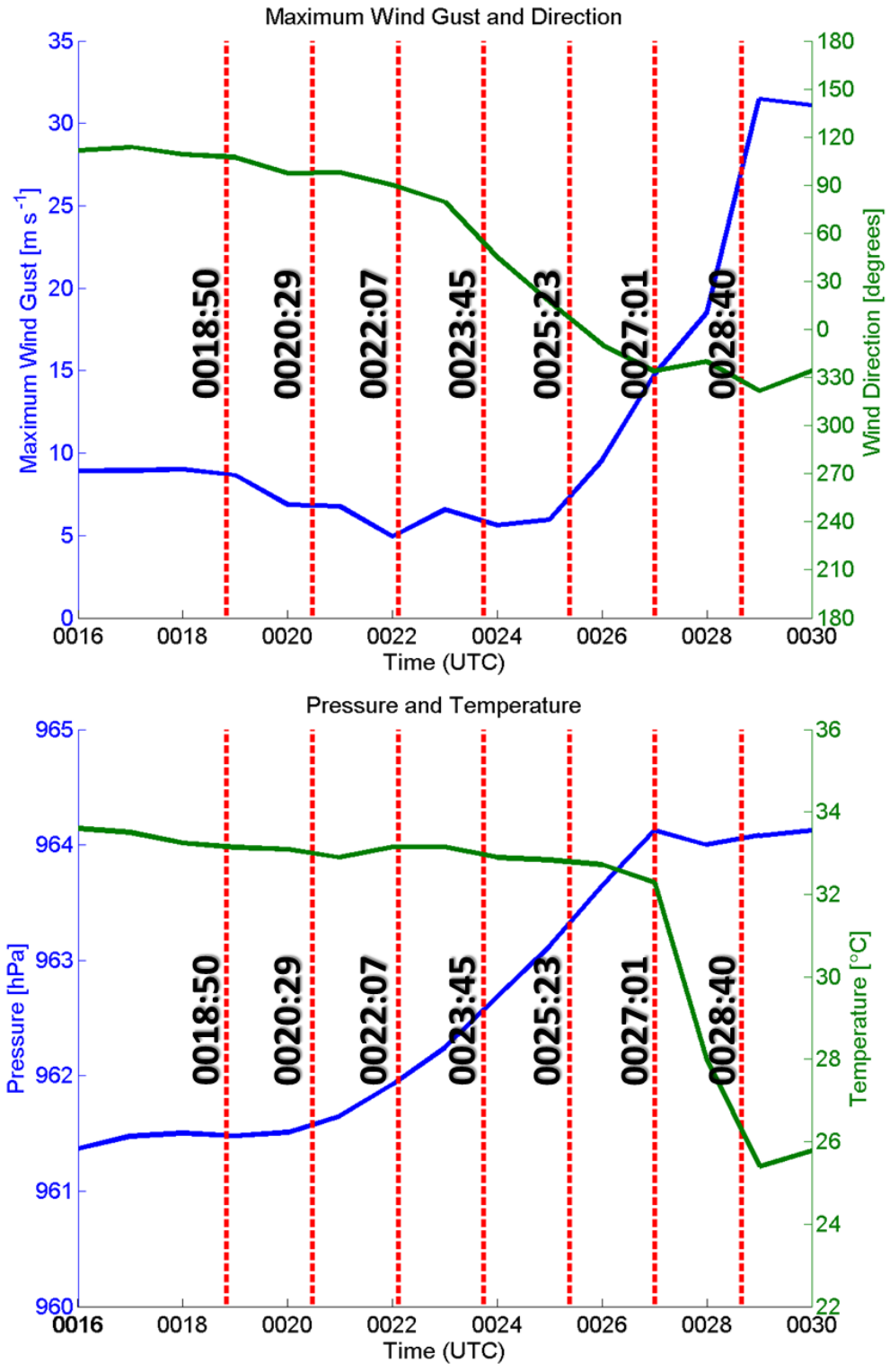


Fig. 6.9. 1-min Oklahoma Mesonet data at Norman, Oklahoma, of (a) 10 m maximum wind gust (m s^{-1}) and wind direction (degrees) and (b) surface pressure (hPa) and 2 m temperature (°C) from 0016 to 0030 UTC. The times of the 3.0° elevation angle scans are noted (red dotted line).

The most intuitive comparison is the RaXPol velocity data to wind direction and wind gusts. As noted, the initial gust front passed by RaXPol between the 0023:45 and 0025:23 UTC volume scans. The RaXPol data indicated a lag between the initial gust front and the more intense winds (and associated rotor) downrange. At the Mesonet site, the wind direction backed from 80° to 45° between 0023:00 and 0024:00 UTC. The wind direction backed further from 45° to 17° between 0024:00 and 0025:00. During this same period, the wind speeds were relatively low with maximum wind gusts ≤ 7 m s^{-1}. The RaXPol velocity data had some evidence of the gradual backing of winds. During the 0023:45-0025:10 UTC volume scan (Fig. 6.7b), the velocity data had three distinct gust front heads behind the initial gust front. Each of these heads had a localized maximum of inbound V_R. The magnitude of the maximum inbound velocity behind the first two heads (ahead of the primary head) were only 2 m s^{-1} and 5 m s^{-1}. The passage of each gust front head may have slightly backed the winds.

The wind direction backed further from 17° to 351° between 0025:00 and 0026:00 UTC. The wind direction remained between 320° to 340° from 0027:00 to 0029:00 UTC. Maximum wind gusts began to increase by 0026:00 UTC with an increase to 10 m s^{-1}. The wind gusts increased further to 15 m s^{-1} at 0027:00 UTC and to 19 m s^{-1} at 0028:00 UTC. This observation is consistent with the RaXPol data. As previously noted, there was an elevated nose in the RaXPol data during the 0027:01-0028:26 UTC volume scan with the most intense winds ≥ 75 m ARL. By 0029:00 UTC, the maximum wind gust had increased to 31 m s^{-1} (i.e., severe thunderstorm criteria). This wind gust agrees with the 0028:40-0030:05 UTC volume scan, which had an estimated 34 m s^{-1} maximum inbound V_R directly impacting RaXPol.

The temperature remained steady through 0027:00 UTC (~33 °C) before decreasing to ~28 °C at 0028:00 UTC and to ~25 °C at 0029:00 UTC. The cold air lagged behind the initial

gust front/wind shift that passed by between the 0023:45 and 0025:23 UTC volume scans. The cold air was associated with the primary head and attendant rotor downrange from the initial gust front. In other words, the two initial gust front heads did not have a discernable horizontal temperature gradient by the time they reached the Mesonet site (i.e., the temperature gradient may have weakened). This may explain why the wind gusts with these two heads were relatively weak and the more intense winds were only associated with the primary head. The surface pressure had gradually increased from 0021:00 UTC to 0027 UTC from 961 hPa to 964 hPa before becoming steady through 0030:00 UTC once the primary gust front head had passed by the station. As noted in Chapter 4, there was a subsequent pressure rise to 968 hPa (Fig. 4.6) associated with the peak precipitation rate at 0038:00 UTC along with additional wind gusts surges.

Overall, the RaXPol radar data are consistent with the 1-min wind data from the Oklahoma Mesonet. There were three wind shifts ≥ 15° between 0024:00 and 0027:00 UTC (two of which were ≥ 25°). These wind shifts may have corresponded with separate gust front heads as seen in RaXPol velocity data. Finally, an elevated nose in velocity data had resulted in a period of maximum wind gusts between 15 to 19 m s^{-1} before increasing to 31 m s^{-1} at the Mesonet station.

6.4 Summary

Here is a summary of the significant findings from this chapter:

- The downburst grew in horizontal scale from at least 2.1 km to 6.4 km in less than 7 min, changing based on size from a microburst to a macroburst. During this time, the maximum near-surface horizontal winds intensified from 23 m s^{-1} to 42 m s^{-1}.

- A horizontal rotor occurred adjacent to the downflow region of the downburst. The rotor was associated with a localized Z_H minimum.
- There were three distinct gust front heads, each with a localized wind maximum, behind the initial gust front. There were three wind shifts ≥ 15° in the 1-min Mesonet data that may have corresponded to these gust front heads.
- The most intense winds (31 m s^{-1} at the Mesonet station) were associated with the final head, which occurred ~5 min after the passage of the initial gust front.
- There was an elevated nose at about 75 m ARL, which the 1-min Mesonet data documented with a 2 to 3 min lag from the most intense winds.
- Vertical vortices developed along the leading edge of the gust with enhanced σ_v and a reduction in ρ_{hv}.
- There were descending surges of mixed-phase precipitation cores aloft indicated by a reduction in ρ_{hv}.

What is remarkable about this wet downburst is the intensification of the horizontal winds during the rapid, horizontal expansion. This expansion in size being coincident with the acceleration of the horizontal winds is notable because it would dynamically imply an increase in the horizontal pressure gradient force. Given the radius of the downburst was increasing, one can infer this increase in the pressure gradient force was due to an increase in the mesohigh surface pressure (see section 5.4).

Given the descending surges of mixed-phase precipitation, it can be inferred the continued stream of mixed-phase precipitation may have aided in the continued expansion and intensity of the downburst through precipitation loading and/or melting hailstones. Evaporation

may have initially contributed as well, but this downburst began well-behind the leading edge of precipitation. Therefore, it is possible the environment may have been close to saturation toward the latter part of the downburst event.

The findings of this chapter complement conceptual models of downbursts (i.e., Fujita 1985) and associated gust fronts (e.g., Goff 1976; Lee and Wilhelmson 1997) from previous studies. None of the previous observation studies had as high spatiotemporal radar data that also contain additional polarimetric variables for better understanding of microphysical processes, such as the detection of descending surges of mixed-phase precipitation cores.

Chapter 7 : Dual-Frequency Comparison

As noted in Chapter 3, KOUN and RaXPol were nearly collocated during the downburst. Therefore, it is judicious to conduct a brief dual-frequency comparison of the PRD for the two radars.

7.1 S-Band and X-band Differences in PRD

It is well-documented that there are significant differences in PRD between S-band and X-band radar data due to the differences in radar wavelength/frequency (e.g., Snyder et al. 2010; Zhang 2016). These differences in PRD are due to both propagation and scattering effects.

For propagation, attenuation and differential attenuation are much more significant at X-band than S-band (Fig. 7.1; Zhang 2016). Attenuation will result in a decrease in the radar estimated Z_H when compared to the intrinsic (or unattenuated) Z_H. Attenuation increases with range when going through precipitation. In other words, there is an increasing difference between the radar estimated Z_H and intrinsic Z_H when going through precipitation. Similarly, differential attenuation will result in a decrease in the radar estimated Z_{DR} when compared to the intrinsic Z_{DR}. Note that V_R, σ_v, and ρ_{hv} are not affected by attenuation if some detectable signal is returned to the radar (though there are still differences between S- and X-band for ρ_{hv} due to scattering). However, many times when going through heavy precipitation (as is often the case in severe convection) there will be total extinction of the signal. At this point, not only would there be a complete loss in radar estimated Z_H and Z_{DR}, but all these other radar variables as well.

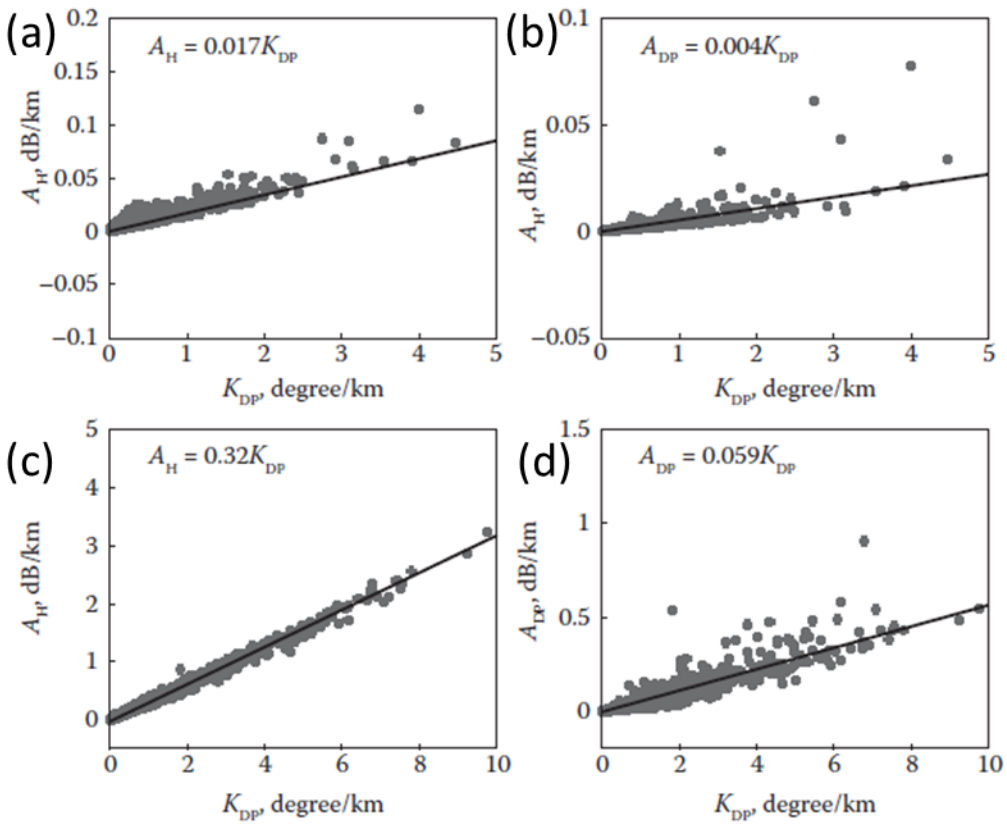


Fig. 7.1. Attenuation (A_H: left column) and differential attenuation (A_{DP}: right column) versus specific differential phase for (a, b) S-band and (c, d) X-band. Modified from Zhang (2016).

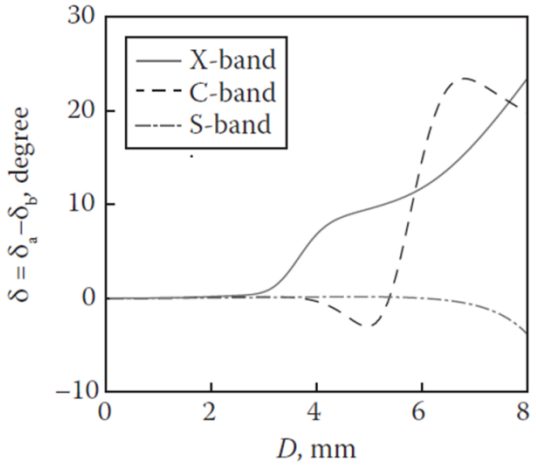


Fig. 7.2. Backscattering phase differences (δ) as a function of raindrop size at S-band, C-band, and X-band frequencies. Modified from Zhang (2016).

For scattering, resonance/non-Rayleigh effects start to have an effect for smaller hydrometeors at X-band than at S-band. This can result in differences in intrinsic dual-pol variables, including Z_H and Z_{DR} (c.f. 1 in Snyder et al. 2010).

These resonance effects also increase the backscatter differential phase (δ) at X-band when compared to S-band (Fig. 7.2; Zhang 2016). ρ_{hv} is sensitive to increased variability in δ. The sensitivity of ρ_{hv} to the increased variability in δ was proven mathematically by Zhang (2016) . It was found that ρ_{hv} is reduced by a factor of $e^{-\sigma_\delta{}^2/2}$ due to random scattering phase difference. In other words, the increased variance of δ will result in the reduction of ρ_{hv}. Therefore, in the case of this downburst with mixed-phase precipitation, it would be expected that ρ_{hv} would have a much greater dynamic range at X-band than at S-band (i.e., it would be more readily be able to detect mixed-phased locations). The benefit of ρ_{hv} when compared to Z_H and Z_{DR} is that it is immune to attenuation (assuming there is not complete extinction of the signal).

One way to quantify the increased sensitivity to ρ_{hv} is by comparing S-band and X-band numerical-scattering solutions for wet hail using the T-Matrix method. Using these numerical solutions ρ_{hv} can be calculated using the following relationship (Zhang 2016):

$$\rho_{hv} = \frac{\int s_a^*(\pi, D) s_b(\pi, D) N(D) dD}{[\int |s_a(\pi, D)|^2 N(D) dD \int |s_b(\pi, D)|^2 N(D) dD]^{1/2}} \tag{7.1}$$

where N(D) (# m^{-3} mm^{-1}) is the particle size distribution (PSD) and $s_{a,b}(\pi, D)$ is the backscattering amplitude at the major or minor axis.

There are some assumptions made when making these calculations. First, an exponential distribution is assumed for the PSD. The disadvantage of an exponential distribution is that it may not perform as well in areas where there is concavity present in the PSD or if there is a

narrow distribution present. Second, the standard deviation of the canting angle is parameterized as a function of fractional water content (Jung et al. 2008):

$$\sigma = 60°(1 - 0.8f_w) \tag{7.2}$$

where f_w is the water fraction for wet hail. Wet hail is assumed because this is below the 0 °C level, so some degree is melting should be expected. More details on the exponential distribution and the T-Matrix method are provided in Chapter 8.

Figure 7.3a and 7.4b are plots of ρ_{hv} as a function of mass/volume-weighted diameter of wet hail and f_w at S-band and X-band, respectively. From these plots, it can be seen that ρ_{hv} at X-band is more sensitive than S-band for wet hail. Note that some of the low values could be due to the fact an exponential distribution for hail was assumed. Since differences between the dual-pol variables will be calculated later in this chapter, it is also useful to plot the ρ_{hv} difference between S-band and X-band (Fig. 7.3c). The sensitivity of ρ_{hv} to distributions of wet hail at X-band when compared to S-band is now clear. This sets the foundation for the dual-frequency comparison later in this chapter.

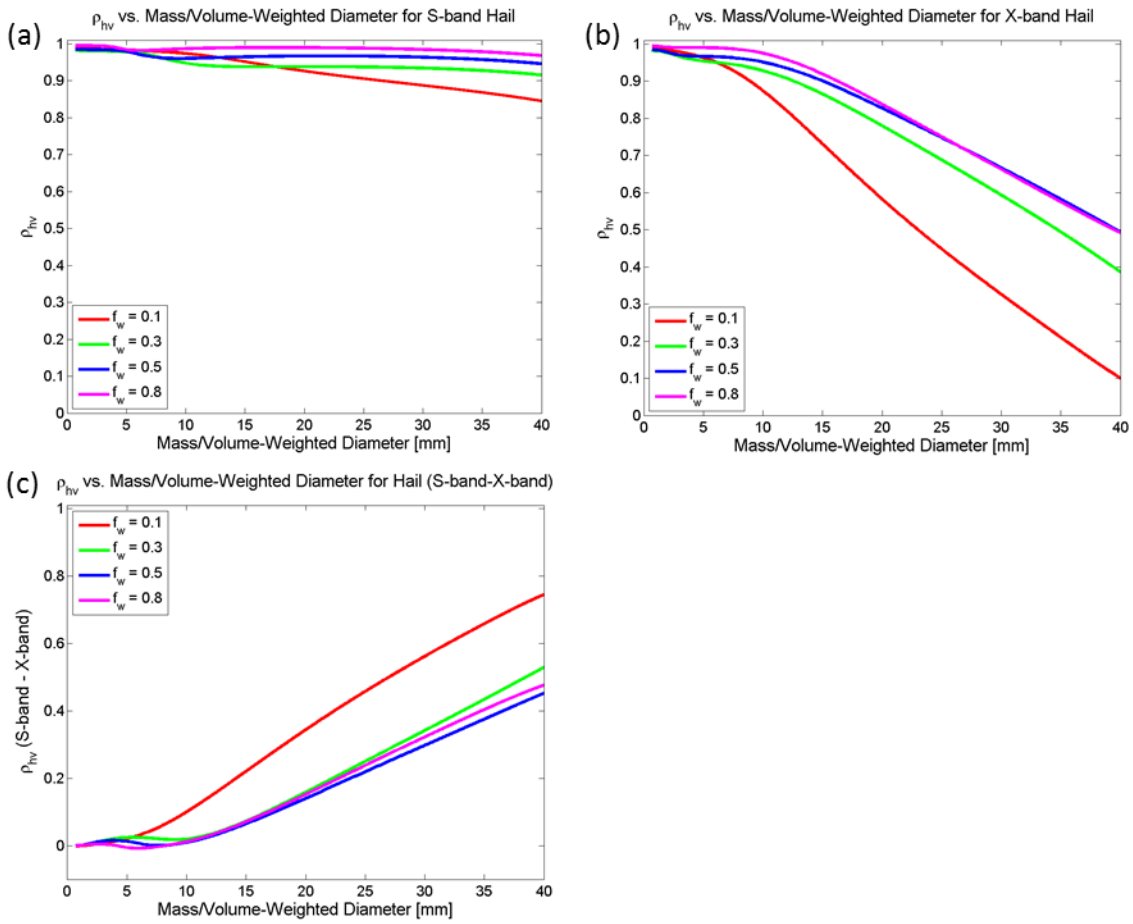


Fig. 7.3. ρ_{hv} as a function of mass/volume-weighted diameter of wet hail and fractional water content (f_w) at (a) S-band (b) X-band and (c) S-band – X-band. These were calculated using the T-matrix method assuming an exponential PSD and with the canting angle as a function of f_w.

7.2 Comparison PPI Scans

Even though the two radars were nearly simultaneous in location, their scanning strategies were not simultaneous. As shown in the analysis of RaXPol data in Chapter 6, the downburst was a fast-evolving system. Therefore, it is sensible to compare elevation scans that are similar in time and space to reduce the influence of errors due to mismatched scans.

For this comparison, the goal was to pick low-level elevation scans (i.e., elevation scans where the radar beam was below the melting layer within 30 km range) that were within 0.5°

elevation angle and 30 sec. Comparison PPI scans that met these criteria were the KOUN 0020:08 UTC scan at 5.3° and the RaXPol 0020:35 UTC scan at 5.0°.

7.3 Comparison Methodology

The methodology for the comparing the PRD from both radars was dependent on the radar. For KOUN, the post-processing for the dual-frequency comparison was a four-step process. In the first step, the data were quality-controlled. As with the HCA, low SNR data were removed. In addition, a median filter was applied to remove the influence of noise. In the second step, a simple attenuation correction was applied to the radar data for Z_H and Z_{DR} using ϕ_{DP} and the relationships in Fig. 7.1. This will allow for the comparison of "intrinsic" S-band values with attenuated X-band values. In the third step, a simple advection correction was applied. The KOUN data were advected azimuthally to the RaXPol PPI time (i.e., each azimuth's scan time was used in the advection). In the final step, the KOUN data were interpolated to the RaXPol downscaled grid (250 m x 1.1°).

For RaXPol, the post-processing for the dual-frequency comparison was a two-step process. In the first step, the data were quality-controlled. As done previously, low SNR data was removed. In second step, RaXPol data were downscaled from 75 m to 250 m range resolution. The azimuth increment of 1.1° remained the same. The downscale process used a median filter to calculate the 250 m resolution data. The final RaXPol downscaled grid was 250 m x 1.1° resolution. Attenuation correction was not applied to RaXPol data due to non-negligible δ from wet hail (i.e., propagation was not the only significant contribution to ϕ_{DP}).

Once the data were on the same grid, the dual-frequency data could be compared, including the calculation of differences between the variables. Figure 7.4 is a flow chart describing the post-processing for PRD from both radars.

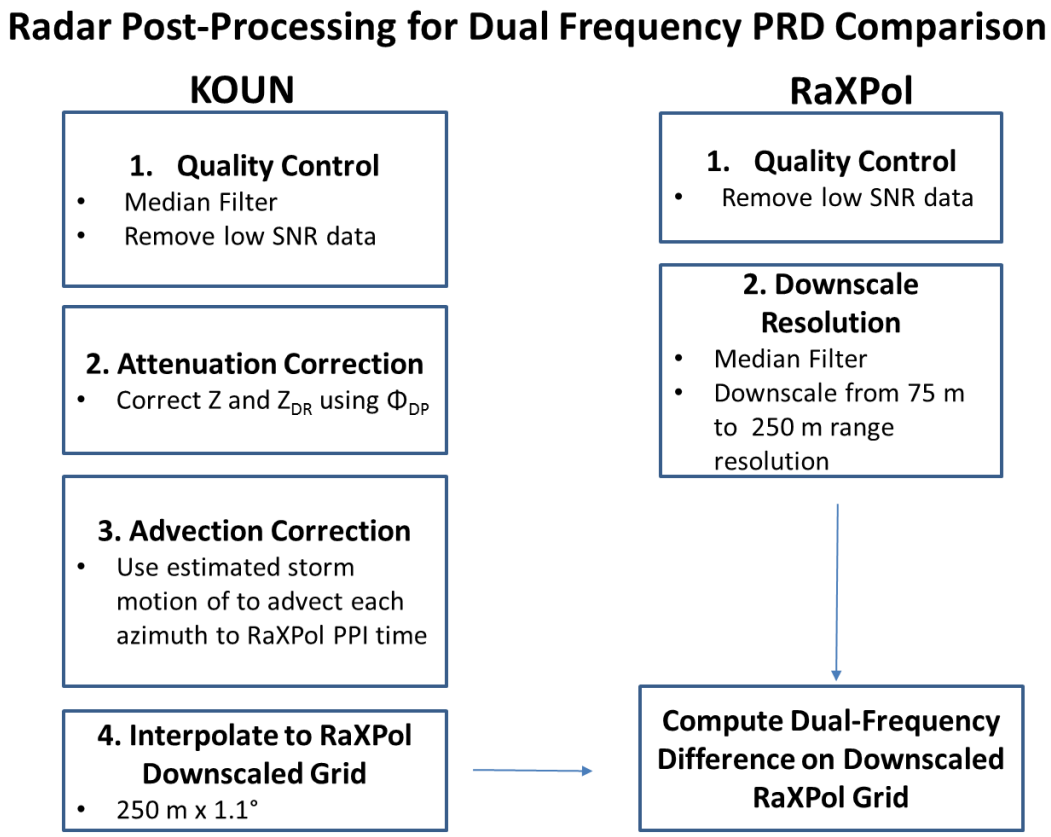


Fig. 7.4. Flow chart describing the post-processing for PRD for KOUN and RaXPol to conduct dual-frequency comparisons between the two radars.

Figure 7.5 is a step-by-step example of how each step in the post-processing affected the KOUN data with Z_H. Similarly, Figure 7.6 is an example of how each step of how each step in the post-processing affected the RaXPol data with ρ_{hv}.

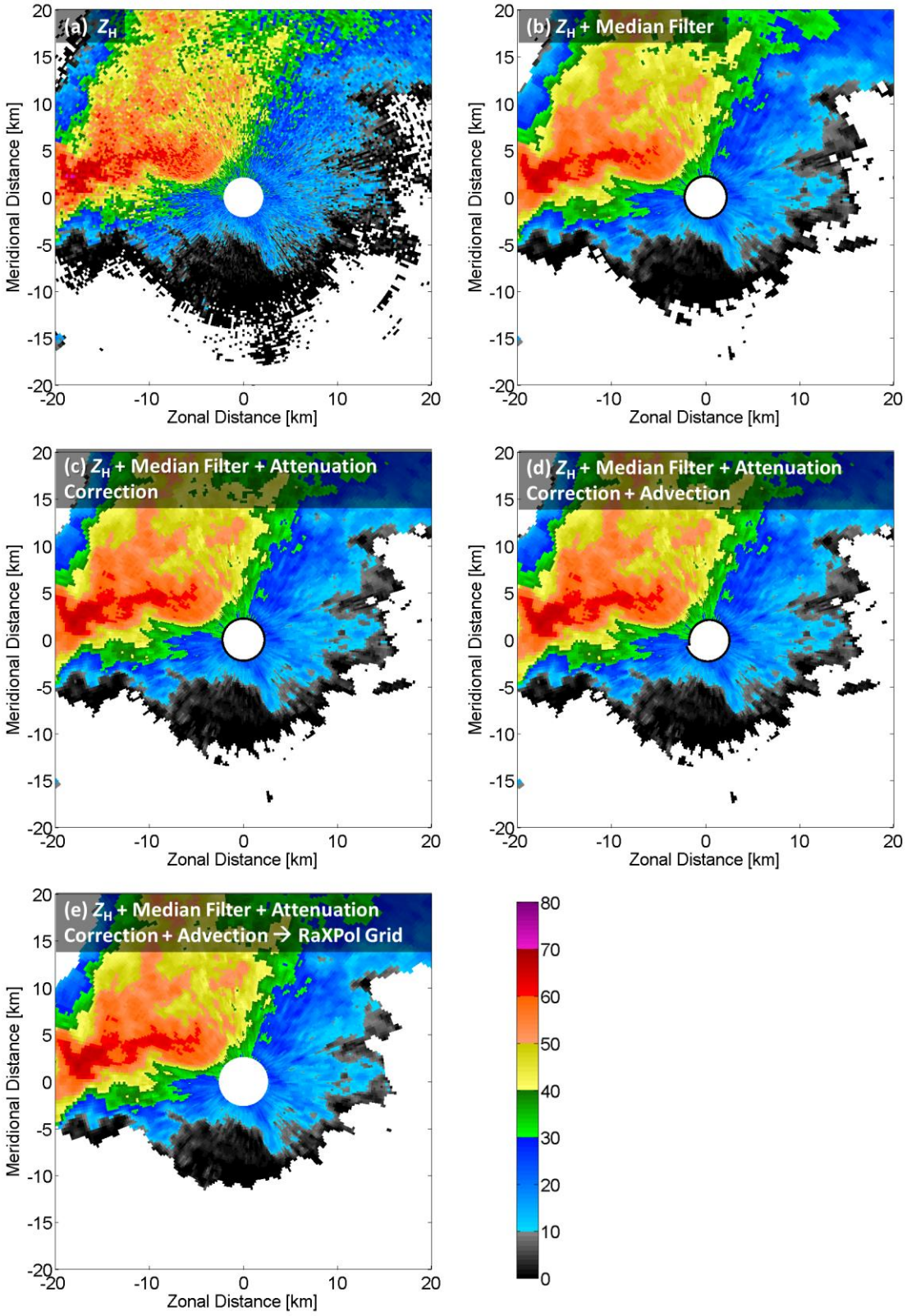

(a) Z_H
(b) Z_H + Median Filter
(c) Z_H + Median Filter + Attenuation Correction
(d) Z_H + Median Filter + Attenuation Correction + Advection
(e) Z_H + Median Filter + Attenuation Correction + Advection → RaXPol Grid
Meridional Distance [km]
Zonal Distance [km]
20
15
10
5
0
-5
-10
-15
-20
80
70
60
50
40
30
20
10
0

Fig. 7.5. Example of post-processing of Z_H (dBZ) from a 5.3° elevation scan of KOUN WSR-88D data at 0020:08 UTC. (a) Pre-processed Z_H, (b) Z_H after the application of a median filter, (c) Z_H after the application of a median filter and attenuation correction, (d) Z_H after the application of a median filter, attenuation correction, and advection correction, and (e) Z_H after the application of a median filter, attenuation correction, and advection correction interpolated to the RaXPol grid are shown. The grid spacing is 250 m x 1.1°.

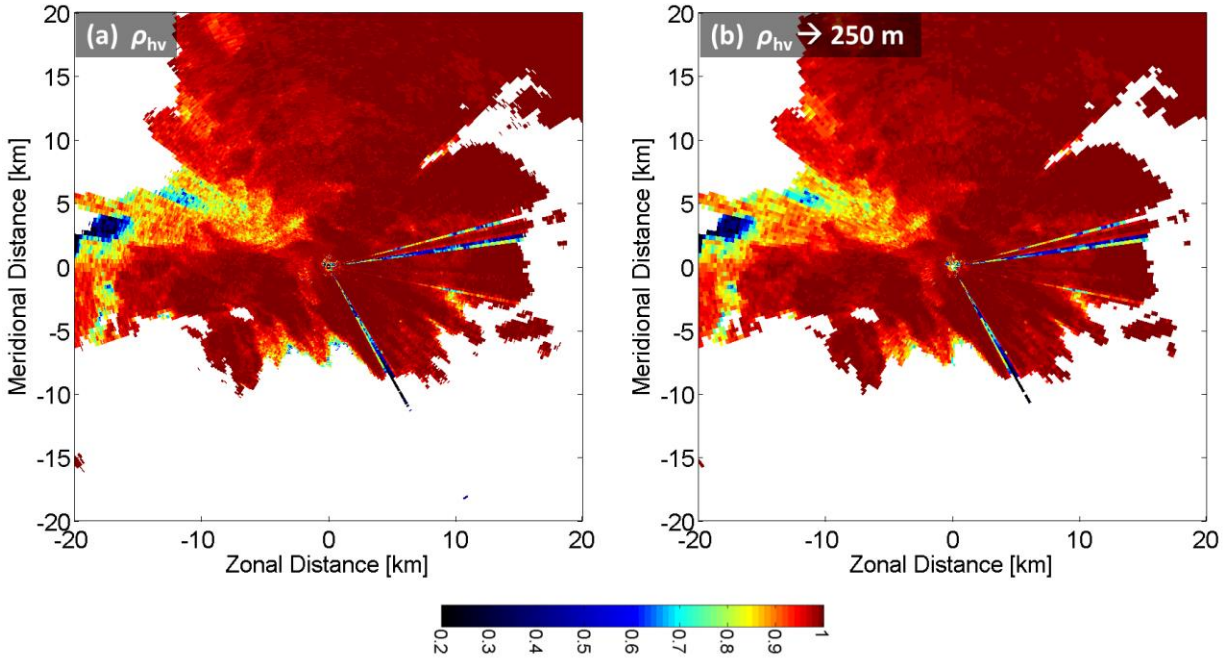


Fig. 7.6. Example of post-processing of ρ_{hv} from a 5.0° elevation scan of RaXPol data at 0020:35 UTC. (a) Pre-processed ρ_{hv} and (b) ρ_{hv} downscaled from 75 m to 250 m range resolution. The grid spacing is 250 m x 1.1°.

7.4 Dual-Frequency Comparison

Once post-processing was complete, the dual-frequency differences could be calculated since the radar data were on the same grid (Fig. 7.7). The calculation of the difference field allows for easy comparison of the data. For this study the difference taken was KOUN – RaXPol (i.e., S-band – X-band).

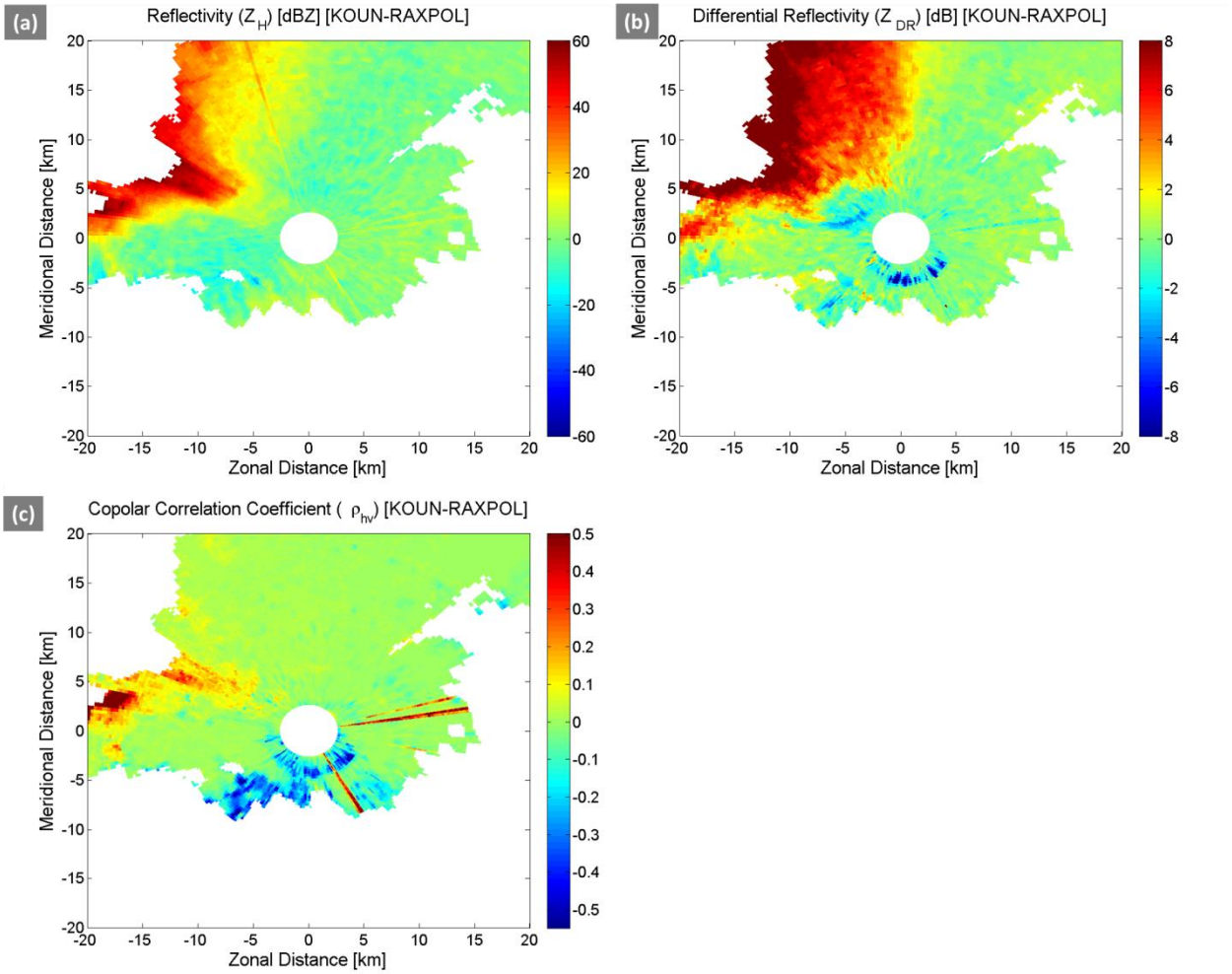


Fig. 7.7. Difference fields of KOUN- RaXPol radar data for (a) Z_H, (b) Z_{DR}, and (c) ρ_{hv}. Difference fields are calculated from the 5.3° elevation scan of KOUN WSR-88D data at 0020:08 UTC and 5.0° elevation scan of RaXPol data at 0020:35 UTC. The grid spacing is 250 m x 1.1°.

The effects of attenuation and differential attenuation at X-band are seen in Z_H and Z_{DR}, respectively (noted by large, positive values in the difference field). The attenuation is most noticeable through the heavy precipitation core to the northwest of the radar. Total extinction of the X-band data is even seen in this area when compared to the S-band data (Fig. 7.5). One thing that is unusual is that prior to the noticeable effects of differential attenuation, there is an area of negative difference in Z_{DR} (i.e., Z_{DR} at S-band is lower than at X-band). This could be due to

resonance scattering effects from hail. In the same area, it is seen that there is an area of positive difference in ρ_{hv}. This is not surprising result based on the sensitivity of ρ_{hv} to distributions of wet hail at X-band when compared to S-band (Fig. 7.4c).

Further investigation on the sensitivity of ρ_{hv} at X-band can be done by applying the HCA from Chapter 5 to the KOUN PPI scan (Fig 7.8). The HCA results can then be plotted as a function of S-band Z_H and ρ_{hv} difference (Fig. 7.9).

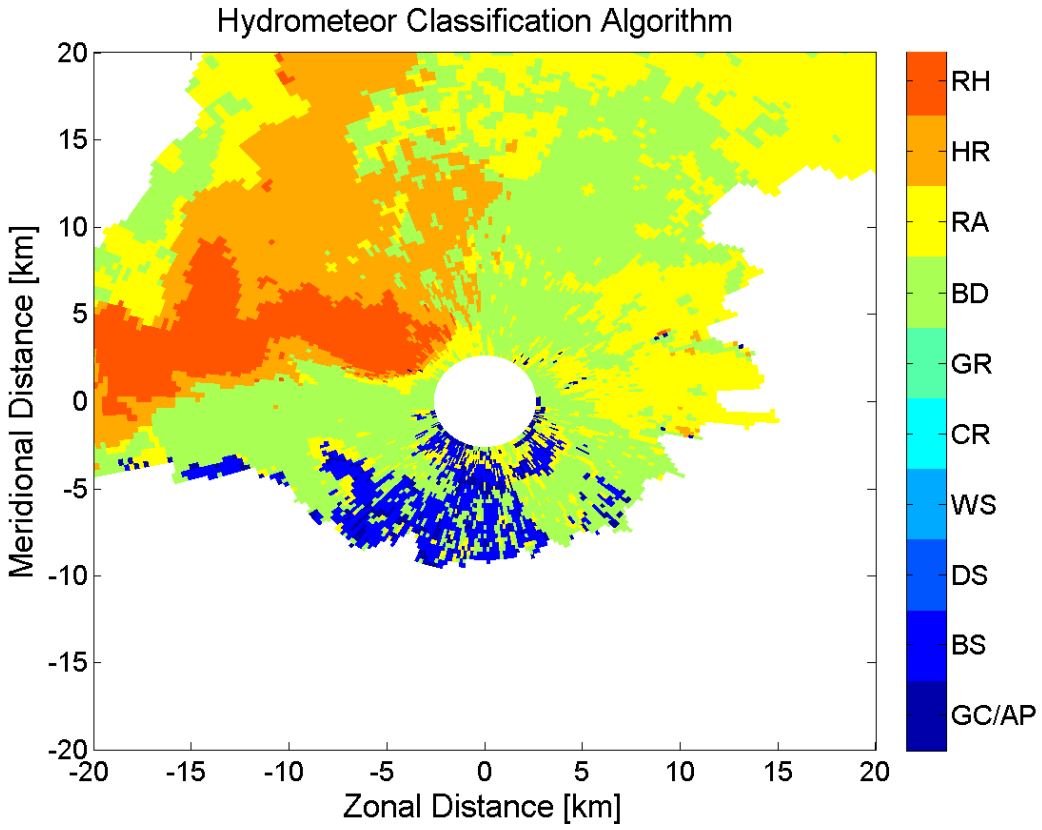


Fig. 7.8. HCA applied to 5.3° elevation scan of KOUN WSR-88D data at 0020:08 UTC.

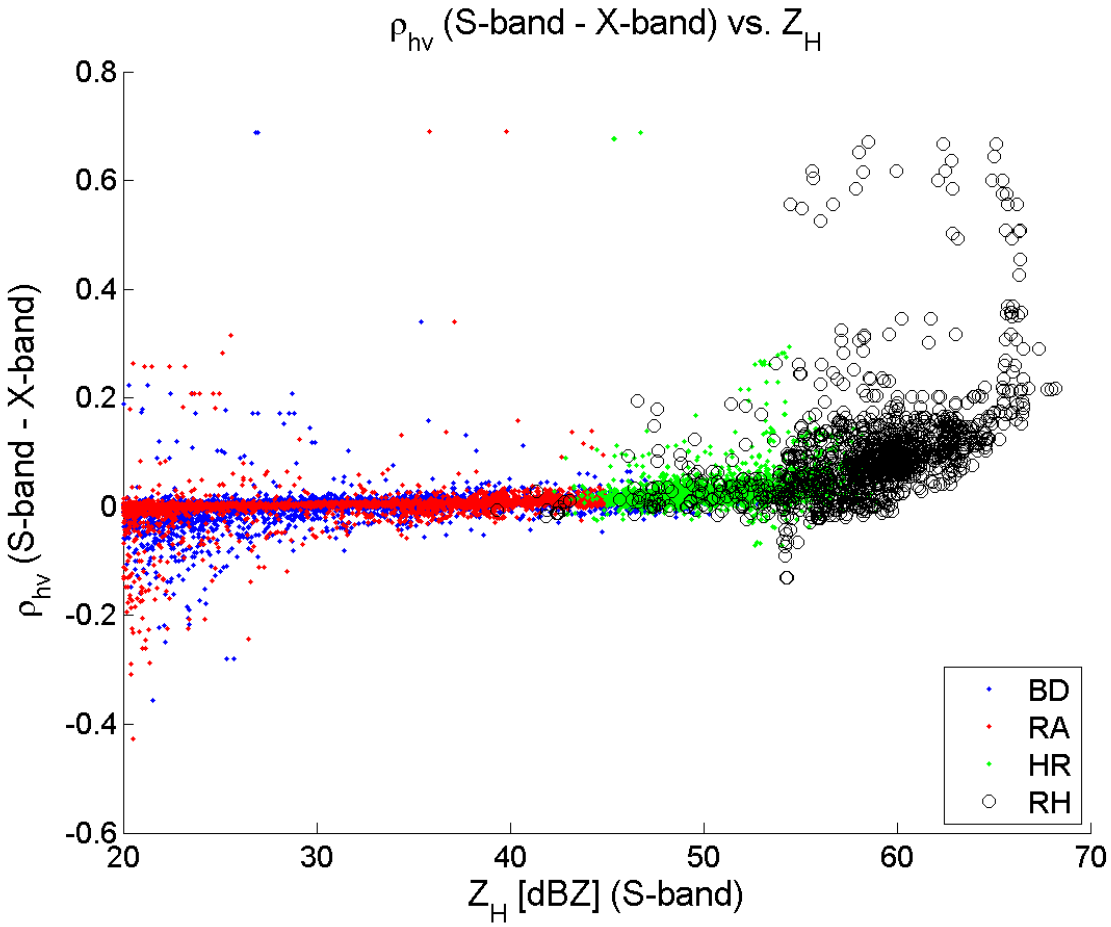


Fig. 7.9. HCA results from Figure 7.8 plotted as a function of S-band Z_H and ρ_{hv} difference between KOUN and RaXPol.

This provides clear evidence on the sensitivity of ρ_{hv} to distributions of wet hail at X-band when compared to S-band. These results are actually in reasonable agreement with the S-band and X-band numerical-scattering solutions for wet hail using the T-Matrix method (Fig.7.3c). Note that while the outlier values around 0.6 to 0.7 are within the realm of possibilities calculated by the T-matrix method, some of these could be due to nonuniform beam-filling and/or three-body scattering (as described in the previous chapter). These could result in a significant reduction of ρ_{hv} in the X-band radar data.

7.5 Summary

A dual-frequency comparison was done between the S-band KOUN PRD and the X-band RaXPol PRD using nearly simultaneous PPI scans in time and space. Advection correction was applied to KOUN PRD to further legitimize the comparison between the two data. Once on the same grid, difference fields between the S-band PRD and X-band PRD were calculated. When an HCA was applied, it was seen that there is increased sensitivity to wet hail distributions for ρ_{hv} at X-band. This reduction in ρ_{hv} is attributed to increased variance of δ due to resonance effects. These results also seem reasonable based on T-Matrix scattering results. Unsurprisingly, the results also show the significant effects of attenuation and differential attenuation at X-band. The benefit of ρ_{hv} when compared to Z_H and Z_{DR} is that it is immune to attenuation (as long as there is not complete extinction of the signal).

Chapter 8 : Variational Retrieval with a Parameterized Operator[6]

An observation-based variational retrieval of rain microphysics from PRD has been developed through the use of derived parametrized polarimetric observation operators and a nonlinear, iterative solution in this chapter. Applied to the downburst case, it is another method beyond the HCA in Chapter 5 that utilizes scattering theory to determine the presence of mixed-phase precipitation. If there are nonrain hydrometeors present (e.g., hail) anywhere in the azimuth, there will not be retrieval or an unrealistic solution due to contamination within the azimuth. These results will be compared to the HCA within this chapter. The variational retrieval also has application beyond the analysis of the downburst by providing a method for the optimal retrieval of rain precipitation microphysics.

8.1 Introduction to Observation-Based Retrievals

Observation-based radar retrievals utilize radar data to retrieve rain microphysics information. Basic retrievals use empirical formulas to calculate rain microphysics information on a gate-by-gate basis (e.g., Z-R relationship for rain rate) without accounting for statistics of the observation errors. Advanced techniques such as Optimal Interpolation (OI) (Eliassen 1954; Gandin 1963) and variational methods (Lorenc 1986), which have been used for data assimilation (DA) in numerical weather prediction (NWP), can be utilized in observation-based retrievals to account for these statistics. Early studies on radar observation-based retrievals using variational methods focused on retrievals of three-dimensional wind fields from Doppler velocity observations (Gao et al. 1999; Gao et al. 2001; Laroche and Zawadzki 1994; Qiu and Xu 1992;

[6]Adapted from: Mahale, V. N., G. Zhang, M. Xue, J. Gao, and H. D. Reeves, 2019: Variational retrieval of rain microphysics and related parameters from polarimetric radar data with a parameterized operator. *J. Atmos. Oceanic Technol.*, conditionally accepted.

Sun et al. 1991). Hogan (2007), Cao et al. (2013), and Yoshikawa et al. (2014) used radar hydrometer related observations to optimally retrieve microphysics information by accounting for background and/or observation errors (i.e., spatial covariance is taken into account).

A variational method utilizes forward observation operators. A forward observation operator (or forward model) is a transformation, based on physical laws, which converts NWP model state variables to observations (Kalnay 2003). Rodgers (2000) states that "the heart of a successful and accurate retrieval method is the forward model". Throughout the literature, the forward observation operators are simply called observation operators. The best observation operators must include relevant physics, are numerically efficient, and have easily calculated first derivatives (i.e., the Jacobian) (Rodgers 2000).

An observation-based radar retrieval is beneficial if it can be easily used in convective scale NWP to improve model microphysics parameterization and weather forecasts. Single moment and double moment microphysics parameterization schemes are commonly used in high-resolution convective scale NWP models (e.g., Lin et al. 1983; Milbrandt and Yau 2005; Morrison et al. 2005). In convective-scale NWP model simulations with single-moment microphysics, rain-water mixing ratio (q_r) is the only prognostic variable for hydrometeor physics. In double-moment microphysical parameterization schemes, both q_r and the number concentration (N_t) are predicted. N_t and q_r can be converted to water content ($W=\rho_a q_r$, where ρ_a is air density) and mass/volume-weighted diameter (D_m), which are related to the drop-size distribution (DSD) for rain (i.e., W and D_m can be considered "related parameters" to describe rain microphysics). They are also considered "physical parameters" because they describe physical quantities. They can be utilized to calculate other microphysical quantities such as rainfall rate. This motivates us to use parameterized polarimetric forward observation operators

that link NWP model state variables and radar observed quantities for an observation-based retrieval. The goal is to link the prognostic physics variables of N_t and q_r to the PRD by retrieving W and D_m.

8.2. Derivation of Parameterized Polarimetric Radar Forward Observation Operators

The DSD is the fundamental description of rain microphysics (Zhang 2016). Therefore, a DSD model will be utilized to derive the observation operators. The DSD is defined as the number of drops in a unit volume for each unit diameter bin. It is a function of equivalent drop diameter, D, and is expressed as expressed as $N(D)$ (# m^{-3} mm^{-1}). D is the diameter of a sphere that has an equivalent volume to an oblate spheroid. The raindrops are assumed to be spheroids that become more oblate as their size increases. In this study, the two-parameter exponential distribution will be used for the derivation of the observation operators:

$$N(D) = N_0 \exp(-\Lambda D) \tag{8.1}$$

where N_0 (m^{-3} mm^{-1}) is the intercept parameter and Λ (mm^{-1}) is the slope parameter. These are often called "DSD parameters".

For a two-parameter DSD model, the model physics parameters N_t and q_r can be converted to W and D_m. Therefore, the state variables chosen for the observation operators are W and D_m. Note that W and D_m can be derived using existing DSD retrievals that retrieve N_0 and Λ; however, the advantage is these are physical parameters, which tend to be Gaussian distributed. Non-physical parameters are less likely to have a Gaussian distribution. N_0 and Λ do not have a Gaussian distribution (e.g., Zhang 2016).

The first state variable, W [g m^{-3}], is derived using the definition of the volume of a sphere ($V = D^3\pi/6$) and the third DSD moment:

$$W = \frac{\pi}{6}\rho_w \int_0^{D_{max}} D^3 N_0 \exp(-\Lambda D) dD \tag{8.2a}$$

$$= \frac{\pi}{6} \times 10^{-3} N_0 \Lambda^{-4} \ \gamma(\Lambda D_{max}, 4) \tag{8.2b}$$

where ρ_w is the density of water and γ is the incomplete gamma function.

As previously noted, W is directly related to q_r as $W=\rho_a q_r$.

The second state variable, D_m [mm], is derived using the ratio of the fourth and third DSD moments:

$$D_m = \frac{\int_0^{D_{max}} D^4 N_0 \exp(-\Lambda D) dD}{\int_0^{D_{max}} D^3 N_0 \exp(-\Lambda D) dD} \tag{8.3a}$$

$$= \frac{1}{\Lambda} \ \frac{\gamma(\Lambda D_{max}, 5)}{\gamma(\Lambda D_{max}, 4)} \tag{8.3b}$$

N_t is related to N_0 by the zeroth DSD moment:

$$N_t = \int_0^{D_{max}} N_0 \exp(-\Lambda D) dD \tag{8.4a}$$

$$= \frac{N_0}{\Lambda} \ \gamma(\Lambda D_{max}, 1) \tag{8.4b}$$

The relationship of D_m to q_r and N_t can be derived by first solving for N_0 from (8.2) and Λ from (8.4). By substituting N_0 into the equation for Λ, the following equation for Λ is found:

$$\Lambda = \left(\frac{\frac{\pi}{6}\rho_w N_t \gamma(\Lambda D_{max}, 4)}{\rho_a q_r \gamma(\Lambda D_{max}, 1)} \right)^{1/3} \tag{8.5}$$

Therefore, using the definition of D_m from (3), D_m is related to q_r and N_t by the following relationship:

$$D_m = \frac{\gamma(\Lambda D_{max}, 5)}{\gamma(\Lambda D_{max}, 4)} \left(\frac{\rho_a q_r \gamma(\Lambda D_{max}, 1)}{\frac{\pi}{6} \rho_w N_t \gamma(\Lambda D_{max}, 4)} \right)^{\frac{1}{3}} \tag{8.6}$$

The dual-polarized radar variables used for the derivation of the observation operators are the horizontal radar reflectivity factor in linear units (Z_h), differential reflectivity (Z_{DR}=10log$_{10}$(Z_{dr}), where Z_{dr} is in linear units), specific differential phase (K_{DP}), and ρ_{hv}.

The K_{DP} observation operator will be applied through the use of Φ_{DP}. Φ_{DP} is the total differential phase, which is the sum of the differential backscattering phase and differential propagation phase (or differential phase). It is assumed that contributions of differential backscattering phase are negligible at S-band for rain. With the assumption that differential backscattering phase is negligible, Φ_{DP} is assumed to only be an estimate of the differential propagation phase, which is the integral of the specific differential phase over the propagation path. Therefore, Φ_{DP} is directly related to K_{DP} by the following:

$$\phi_{DP}(r) = 2 \int_0^r K_{DP}(l) dl \tag{8.7}$$

Φ_{DP} is used in the variational retrieval instead of K_{DP} because it is a direct quantity that is estimated by radars.

The derivation of the observation operators is a three-step process. The first step is to calculate N(D) for a range of D_m using a normalized W of 1 g m^{-3} and assuming an exponential distribution (i.e., Z_h and K_{DP} are normalized so that W is 1 g m^{-3} and D_m only varies). For this derivation, D_m will range from 0.05 to 5 mm.

The second step is to calculate Z_h, $Z_{dr,}$ K_{DP}, and ρ_{hv} by using the S-band scattering amplitudes calculated with the T-matrix method and using the $N(D)$ values from the first step.

The T-matrix method (Waterman 1971) is a numerical-scattering solution. This was the same method used to calculate ρ_{hv} for hail in the previous chapter.

For the scattering amplitude calculations, it is assumed that raindrops will fall with their major axis aligned horizontally (i.e., canting angle mean and standard deviations are zero). It has been found that the true standard deviation for the canting angles for raindrops is somewhere between 0° to 10° (e.g., Bringi and Chandrasekar 2001; Ryzhkov et al. 2002). Ryzhkov et al. (2002) found the assumption of no canting angle only results in a slight overestimation (< 6%) in some PRD, so this is a reasonable assumption. The axis ratios of the raindrops assume the following relationship (Brandes et al. 2002):

$$\gamma = 0.9551 + 0.0251D - 0.03644D^2 + 0.005303D^3 - 0.002492D^4 \quad (8.8)$$

where γ is the ratio of the semiminor and semimajor axes.

The third step is to use a polynomial function to fit the calculated Z_h, $Z_{dr,}$ K_{DP}, and ρ_{hv} to D_m. Because a normalized W of 1 g kg^{-1} was used in the calculation, W will be multiplied by the polynomial for Z_h and $K_{DP.}$ These will cancel for Z_{DR} and ρ_{hv} because they are ratios.

As a result, here are the derived parametrized polarimetric radar forward observation operators for rain:

$$Z_h \approx W\left(-0.3078 + 20.87D_m + 46.04{D_m}^2 - 6.403{D_m}^3 + 0.2248{D_m}^4\right)^2 \quad (8.9)$$

$$Z_{dr} \approx 1.019 - 0.1430D_m + 0.3165{D_m}^2 - 0.06498{D_m}^3 + 0.004163{D_m}^4 \quad (8.10)$$

$$K_{DP} \approx W\left(0.00926 - 0.0870D_m + 0.1994{D_m}^2 - 0.02824{D_m}^3 + 0.001772{D_m}^4\right) \quad (8.11)$$

$$\rho_{hv} \approx 0.9987 + 0.008289D_m - 0.01160{D_m}^2 + 0.03513{D_m}^3 - 0.0003187{D_m}^4 \quad (8.12)$$

or in logarithmic units for Z_H and Z_{DR}:

$$Z_H \approx 10\log_{10}\left[W\left(-0.3078 + 20.87D_m + 46.04{D_m}^2 - 6.403{D_m}^3 + 0.2248{D_m}^4\right)^2\right] \quad (8.13)$$

$$Z_{DR} \approx 10\log_{10}\left(1.019 - 0.1430D_m + 0.3165{D_m}^2 - 0.06498{D_m}^3 + 0.004163{D_m}^4\right) \quad (8.14)$$

Figure 8.1 plots all the observation operators from (8.9)-(8.14). These observation operators include relevant physics, are numerically efficient (i.e., polynomials), and are able to easily calculate the first derivative. Note that these calculated polarimetric variables are intrinsic values that do not consider propagation and error effects (e.g., attenuation and sampling errors) and are only valid for S-band radar data.

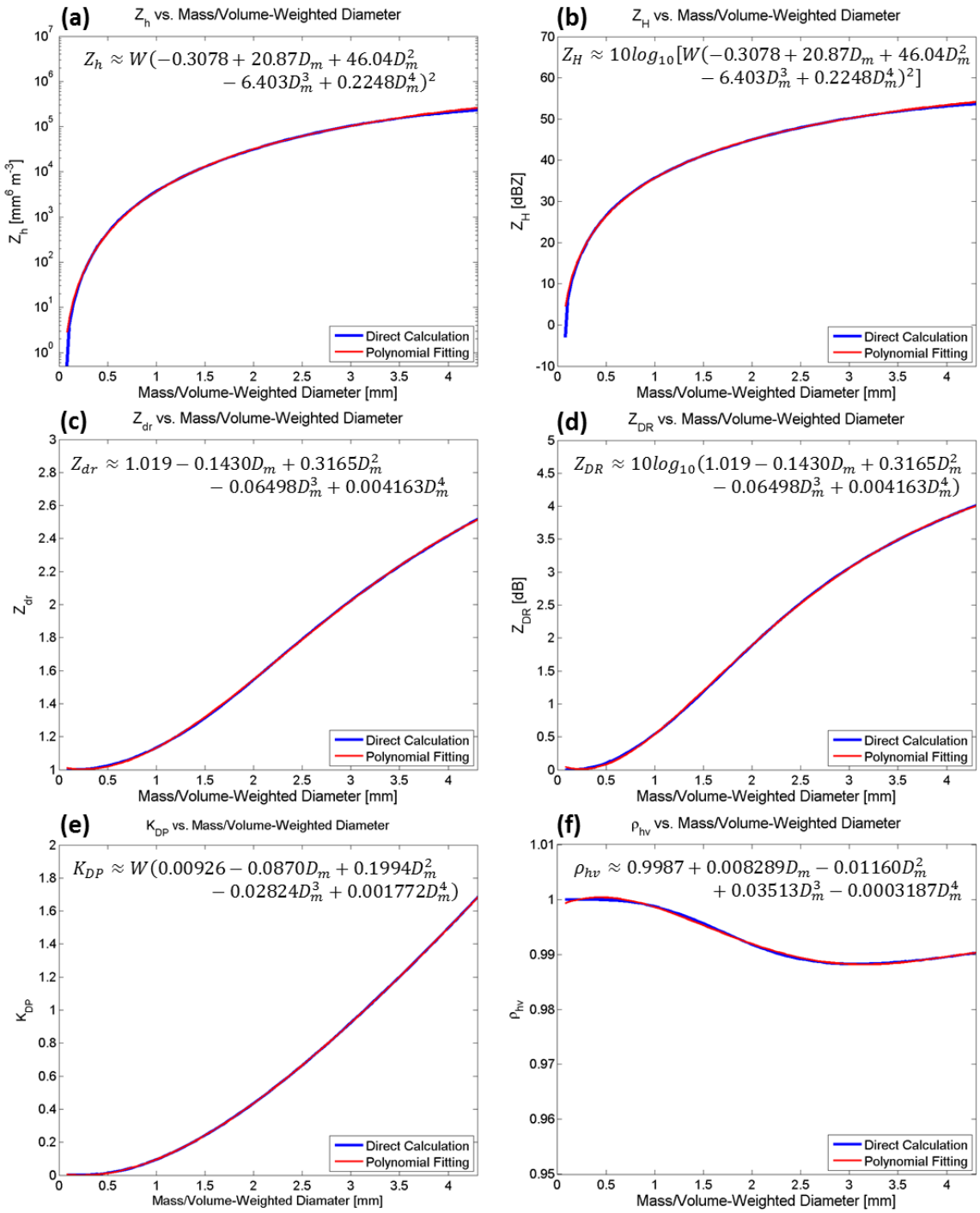


Fig. 8.1. The fitted parameterized polarimetric forward observation operators compared to direct calculations from T-matrix method for (a) Z_h, (b) Z_H, (c) Z_{dr}, (d) Z_{DR}, (e) K_{DP}, and (f) ρ_{hv}. These are normalized for W of 1 g m^{-3}. The equation on each panel is the derived observation operator.

8.3 Variational Retrieval Method

The solution to an observation-based variational retrieval is an optimal analysis field that minimizes a cost function (Lorenc 1986):

$$J(\mathbf{x}) = (\boldsymbol{x} - \mathbf{x_b})^T \mathbf{B}^{-1} (\mathbf{x} - \mathbf{x_b}) + [\boldsymbol{y} - H(\mathbf{x})]^T \mathbf{R}^{-1} [\boldsymbol{y} - H(\mathbf{x})] \quad (8.15)$$

The convention here follows vector-matrix form, which is the notation used by the data assimilation community (e.g., Huang 2000; Ide 1997; Kalnay 2003). The uppercase bold letters represent matrices and the lowercase bold represent vectors in this convention.

The cost function (J) is the distance between the analysis ($\mathbf{x}$) and the background ($\mathbf{x_b}$) weighted by the inverse of the background error covariance ($\mathbf{B}$) plus the distance of the analysis ($\mathbf{x}$) to the observations ($\mathbf{y}$) weighted by the inverse of the observation error covariance ($\mathbf{R}$) (Kalnay 2003). H is the observation operator.

The solution for an observation-based OI retrieval is (Kalnay 2003):

$$\mathbf{x}_a = \mathbf{x}_b + \mathbf{W}[\mathbf{y} - H(\mathbf{x}_\mathrm{b})] \quad (8.16a)$$

$$\mathbf{W} = \mathbf{B}\mathbf{H}^T(\mathbf{R} + \mathbf{H}\mathbf{B}\mathbf{H}^T)^{-1} \quad (8.16b)$$

where $\mathbf{W}$ is the optimal weight matrix and $\mathbf{H}$ is the Jacobian, or linear approximation of H.

The assumption with the OI solution is that background is a reasonable approximation of the true analysis, so that the solution of the analysis is equal to the background values plus small increments (Kalnay 2003). The OI solution is usually not solved iteratively (i.e., it is solved explicitly), and is equivalent to the three-dimensional variational assimilation (3DVAR) solution that is found by minimizing the cost function (8.15).

For moderately nonlinear problems, the Gauss-Newton iterative method can find the solution (Rodgers 2000):

$$\mathbf{x}_{i+1} = \mathbf{x}_b + \mathbf{W}[\mathbf{y} - H(\mathbf{x}_i) + \mathbf{H}_i(\mathbf{x}_i - \mathbf{x}_\mathrm{b})] \quad (8.17)$$

$$\mathbf{W} = \mathbf{B}\mathbf{H}_i^T(\mathbf{R} + \mathbf{H}_i\mathbf{B}\mathbf{H}_i^T)^{-1} \qquad (8.17b)$$

where $\mathbf{H}_i$ and $H(\mathbf{x}_i)$ are updated during each iteration, i.

The Gauss-Newton iterative method is utilized to solve nonlinear least-squares problems (e.g., variational data-assimilation problems) and has been shown to correspond to the incremental four-dimensional variational (4DVAR) assimilation solution (Lawless et al. 2005a, 2005b). For this study, the Gauss-Newton iterative method (8.17) was used to better account for the nonlinearity in the forward operator.

Note that for any variational retrieval, there is an assumption that the background and observation errors have a Gaussian probability distribution, the background and observation errors are uncorrelated, and the background and observations are unbiased (Kalnay 2003). Errors will be introduced in the variational retrieval if these conditions are not met.

A comparison to the OI solution (8.16) is also shown in the Appendix at the end of the chapter. The comparison between both methods is shown because even though most retrieval problems are not truly linear, many still utilize linearization about some prior state even when the observation operator is not truly linear (Rodgers 2000). Therefore, the OI solution is tested because it provides a baseline to compare to Gauss-Newton iterative solution and to see if linearity can be assumed.

To solve an observation-based variational retrieval, the state variables and observations must be defined. As previously noted, the state variables for this observation-based retrieval are W and D_m, forming the state vector $\mathbf{x} = [W; D\text{m}]$. The observations used are Z_H, Z_{DR}, and Φ_{DP}, yielding the observation vector $\mathbf{y} = [Z_H; Z_{DR;}\ \Phi_{DP}]$. ρ_{hv} is not used because of its limited dynamic range for rain at S-band (Fig. 8.1f). ρ_{hv} would not add value to retrieval for pure rain as its error is approximately equal to dynamic range.

For the solution to (8.17)**,** let us look at each term individually. First, assume that it is solved azimuthally and that the number of range gates in one azimuth is n_r. The variational retrieval is solved azimuthally (1-D) to coincide with Φ_{DP} measurements. Therefore, the dimension of state variables is n = $2n_r$ and the dimension of observations is p = $3n_r$. $\mathbf{x}_i$ is an analysis vector at iteration i with dimension n x 1 ($2n_r$ x 1).

$\mathbf{x}_{i+1}$ is an analysis vector with dimension n x 1 ($2n_r$ x 1). It is the concatenate of the analysis vectors of the state variables, W and D_m.

$\mathbf{x}_b$ is a background state vector (also known as the first guess) with dimension n x 1 ($2n_r$ x 1). It is the concatenate of the background vectors of the state variables, W and D_m. For this study, the background state vector is obtained from empirical formulas for W and D_m (Zhang 2016):

$$W = (1.023 \times 10^{-3}) Z_h \times 10^{\,-0.0742 {Z_{DR}}^3 + 0.511 {Z_{DR}}^2 - 1.511 Z_{DR}} \tag{8.18}$$

$$D_m = 0.0657 {Z_{DR}}^3 - 0.332 {Z_{DR}}^2 + 1.090 Z_{DR} + 0.689 \tag{8.19}$$

y is an observation vector with dimension p x 1 ($3n_r$ x 1).

B is a covariance matrix of background errors with dimension n x n ($2n_r$ x $2n_r$). The background error standard deviations used in this study were σ_W = 0.707 g m^{-3} and σ_{Dm} = 1 mm (i.e., the variances are ${\sigma_W}^2$ = 0.5 g^2 m^{-6} and ${\sigma_{Dm}}^2$ = 1 mm^2). The relatively large background error gives more weight to observations, which is a reasonable assumption since this is an observation-based retrieval with no model background. The background covariance assumes a Gaussian correlation model (Huang 2000):

$$b_{ij} = {\sigma_b}^2 \exp\left[-\frac{1}{2}\left(\frac{r_{ij}}{r_L}\right)^2\right] \tag{8.20}$$

where σ_b^2 is the is the background error covariance (σ_W^2 and σ_{Dm}^2), r_{ij} is the distance between the *i*th and *j*th radar gates, and r_L is the spatial decorrelation length. In this study, r_L was set to 1000 m. An increase (decrease) in the spatial decorrelation length results in an increase (decrease) in smoothing of the final analysis. Therefore, the spatial influence of the observations is determined by the background error covariance matrix.

R is a covariance matrix of observations errors with dimension p x p ($3n_r$ x $3n_r$). The observation error standard deviations used in this study were σ_{ZH} = 1 dB, σ_{ZDR} = 0.2 dB, and $\sigma_{\Phi DP}$ = 5°. It is assumed that each observation's error is independent from the other observations. Therefore, **R** is a diagonal matrix.

H is the observation operator that converts state variables in the analysis vector at iteration *i* to observations. These operators (8.11), (8.13), and (8.14) were derived in 8.2.

H is the Jacobian, which contains the partial derivative of each observation operator with respect to the state variables. It has a dimension p x n ($3n_r$ x $2n_r$). These can be calculated analytically by taking the partial derivatives of (8.11), (8.13), and (8.14) with respect to *W* and D_m:

$$\frac{\partial Z_H}{\partial W} = \frac{10}{W\ln(10)} \tag{8.21}$$

$$\frac{\partial Z_H}{\partial D_m} = \frac{20\left(20.87 + 2 * 46.04 D_m - 3 * 6.403 {D_m}^2 + 4 * 0.2248 {D_m}^3\right)}{\ln(10)\left(-0.3078 + 20.87 D_m + 46.04 {D_m}^2 - 6.403 {D_m}^3 + 0.2248 {D_m}^4\right)} \tag{8.22}$$

$$\frac{\partial Z_{DR}}{\partial W} = 0 \tag{8.23}$$

$$\frac{\partial Z_{DR}}{\partial D_m} = \frac{10\left(-0.1430 + 2 * 0.3165 D_m - 3 * 0.06498 {D_m}^2 + 4 * 0.004163 {D_m}^3\right)}{\ln(10)\left(1.019 - 0.1430 D_m + 0.3165 {D_m}^2 - 0.06498 {D_m}^3 + 0.004163 {D_m}^4\right)} \tag{8.24}$$

$$\frac{\partial K_{DP}}{\partial W} = 0.00926 - 0.0870 D_m + 0.1994 {D_m}^2 - 0.02824 {D_m}^3 + 0.001772 {D_m}^4 \tag{8.25}$$

$$\frac{\partial K_{\mathrm{DP}}}{\partial D_{\mathrm{m}}} = W\left(-0.0870 + 2 * 0.1994 D_{\mathrm{m}} - 3 * 0.02824 {D_{\mathrm{m}}}^2 + 4 * 0.001772 {D_{\mathrm{m}}}^3\right) \quad (8.26)$$

The partial derivative of $\partial Z_{\mathrm{DR}}/\partial W$ is zero because Z_{DR} only depends on D_{m}. For the partial derivatives $\partial Z_{\mathrm{H}}/\partial W$, $\partial Z_{\mathrm{H}}/\partial D_{\mathrm{m}}$, and $\partial Z_{\mathrm{DR}}/\partial D_{\mathrm{m}}$, the matrix is diagonal because they have gate-to-gate independence. For $\partial \Phi_{\mathrm{DP}}/\partial W$ and $\partial \Phi_{\mathrm{DP}}/\partial D_{\mathrm{m}}$, the matrix is a lower triangle because Φ_{DP} is defined as two times the summation of K_{DP} up to a given gate:

$$\phi_{\mathrm{DP}}(r_n) = 2\sum_{i=1}^{N} K_{\mathrm{DP}}(r_i)\Delta r_i \quad (8.27)$$

The observation-based variational retrieval is complete when the analysis vector, $\mathbf{x}_{\mathrm{i}}$, converges to a solution. A block diagram of the iteration procedure for the variational retrieval is shown in Figure 8.2. In practice, the number of iterations can be fixed and/or a convergence test applied. If there are nonrain hydrometeors present (e.g., hail) anywhere in the azimuth, there may not be a solution or an unrealistic solution due to contamination within the azimuth (since the retrieval is solved azimuthally). This is because these parametrized polarimetric radar forward observation operators were derived using the T-matrix calculations for rain. Essentially, this can prove the presence of mixed-phased precipitation through a more rigorous, quantitative method based on scattering theory than the HCA as shown in Chapter 5.

To solve this for an entire PPI radar scan (i.e., a single elevation), each azimuth is solved independently. In other words, simply loop through all the azimuths to get a solution for an entire radar elevation.

Verification of the variational retrieval and observation operators were done by conducting experiments on DSD data collected by a disdrometer. The verification results and application on a single azimuth of radar data are shown in the Appendix at the end of the chapter.

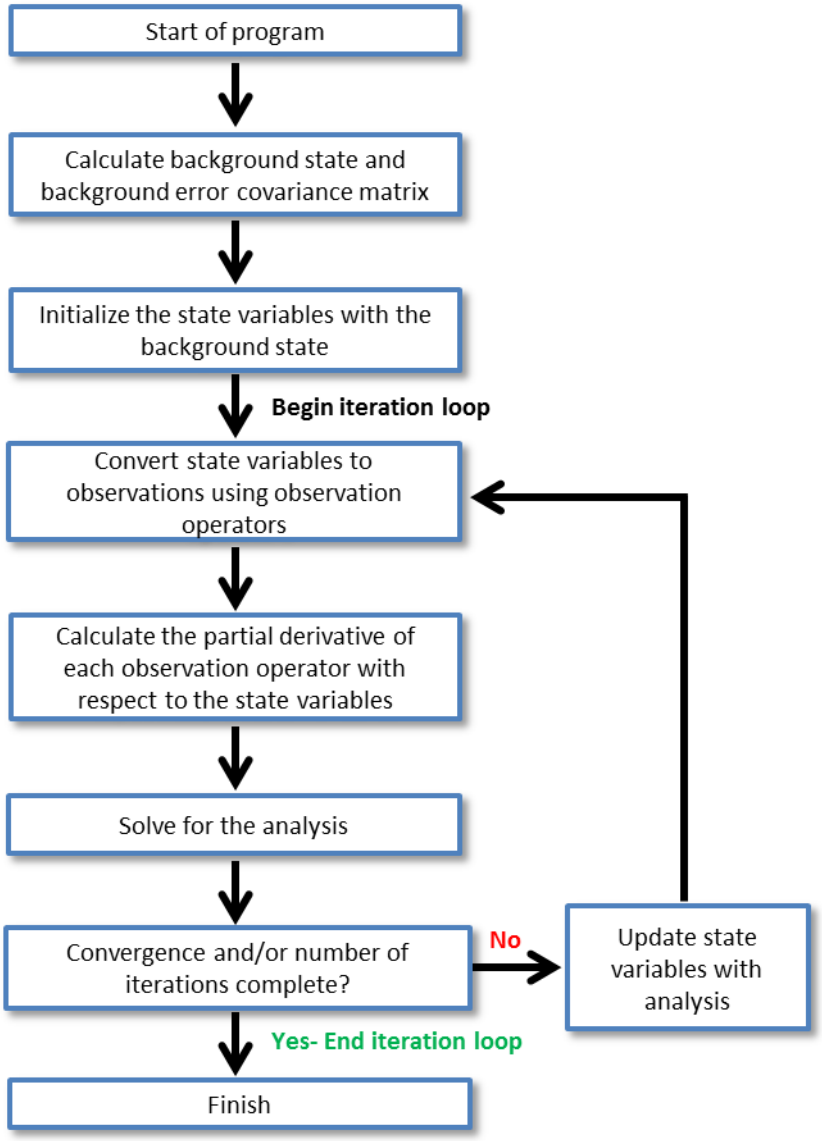


Fig. 8.2. Block diagram of the iteration procedure for the nonlinear variational retrieval for a single azimuth of radar data.

8.4 Variational Retrieval on Downburst Case

The variational retrieval was applied on the entire PPI of radar data from the downburst event by looping through all 360 azimuths. For easy comparison, the KOUN PPI (0020:08 UTC scan at 5.3°) used in the previous chapter was used to test the variational retrieval.

Once D_m and W are obtained using the variational retrieval, the observation operators are used to calculate Z_H and Z_{DR} analyses to assess the observation operators in context to the forward problem; however, instead of calculating Φ_{DP} by adding K_{DP} down radial, the K_{DP} analysis is compared to K_{DP} calculated using the slope of a least squares fit from filtered observations (i.e., algorithm used in the WSR-88D network). In this context, the calculated K_{DP} is considered a derived microphysical quantity. The W and D_m analyses are shown in Figure 8.3 and the Z_H and Z_{DR} observations and analyses are shown in Figure 8.4. The differences between the observations and analyses are also shown (Fig. 8.4e, f). The K_{DP} best-line fit method and analysis are shown in Figure 8.5.

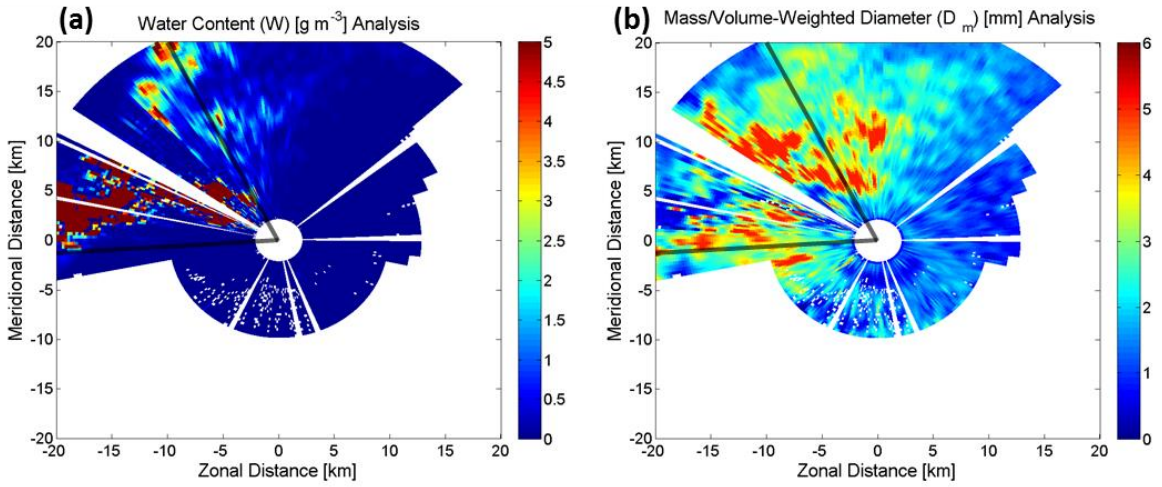


Fig. 8.3. Analysis for (a) W and (b) D_m by applying the variational retrieval using a 5.3° elevation scan of KOUN WSR-88D data from 15 June 2011 at 0020 UTC. The boundaries of the sector with hail contamination are marked by the black lines.

The most evident feature in the analyses is the chaotic and noisy results across the western to northwestern sector of the PPI. Parts of the analyses in this area are unrealistic and the Z_H analysis differs significantly from the observations. There are even some azimuths that are completely void of data in the analyses. In addition to this sector, there are a few other azimuths

that are void of data. These azimuths do not have a solution likely due to low Z_H values and/or the presence of nonmeteorological scatterers (i.e., biological or ground clutter) in the azimuth.

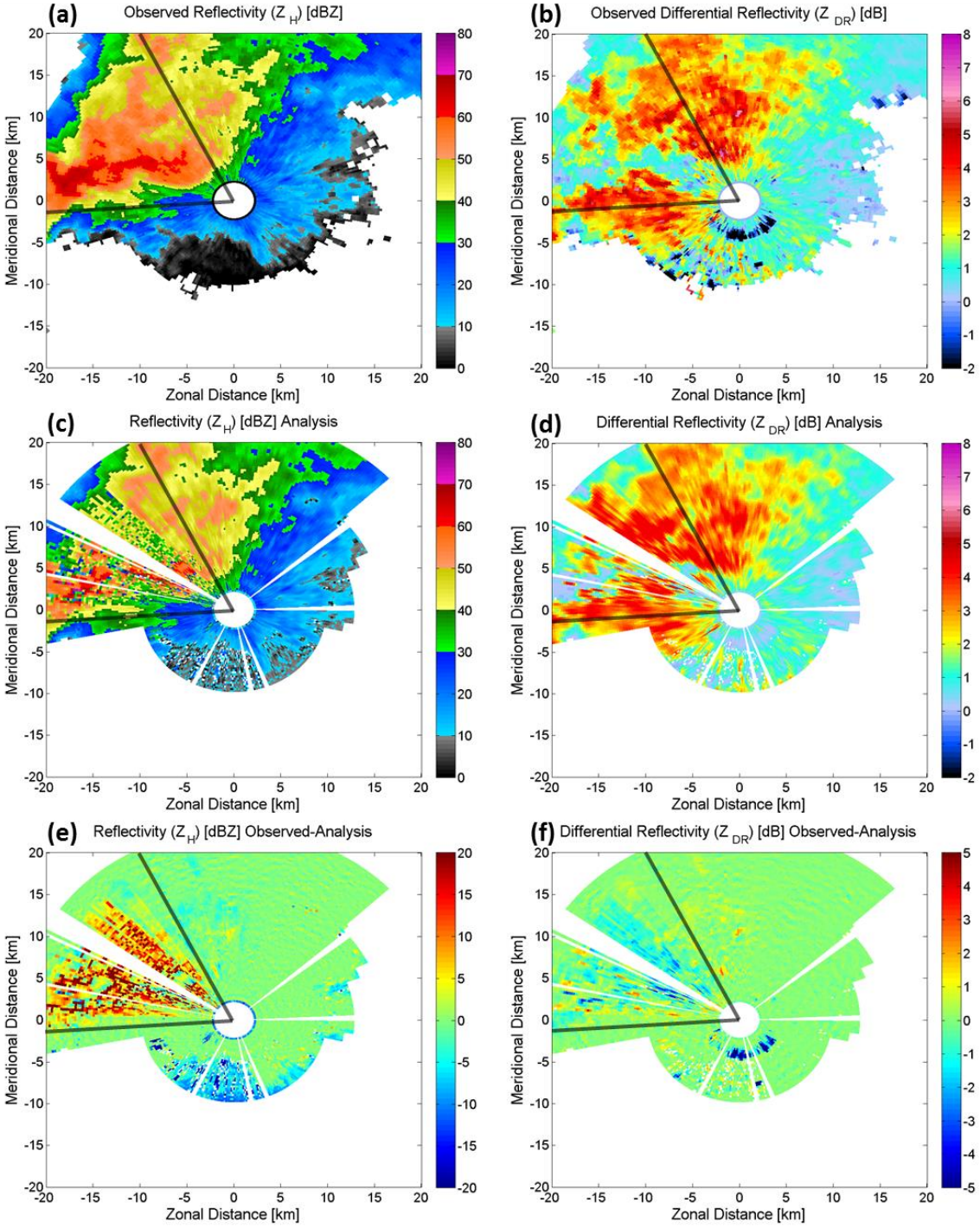


Fig. 8.4. (a) Z_H observations, (b) Z_{DR} observations, (c) Z_H analysis, (d) Z_{DR} analysis, (e) Z_H observations and analysis difference, and (f) Z_{DR} observations and analysis difference using a

5.3° elevation scan of KOUN WSR-88D data from 15 June 2011 at 0020 UTC. The analyses are from applying the variational retrieval.

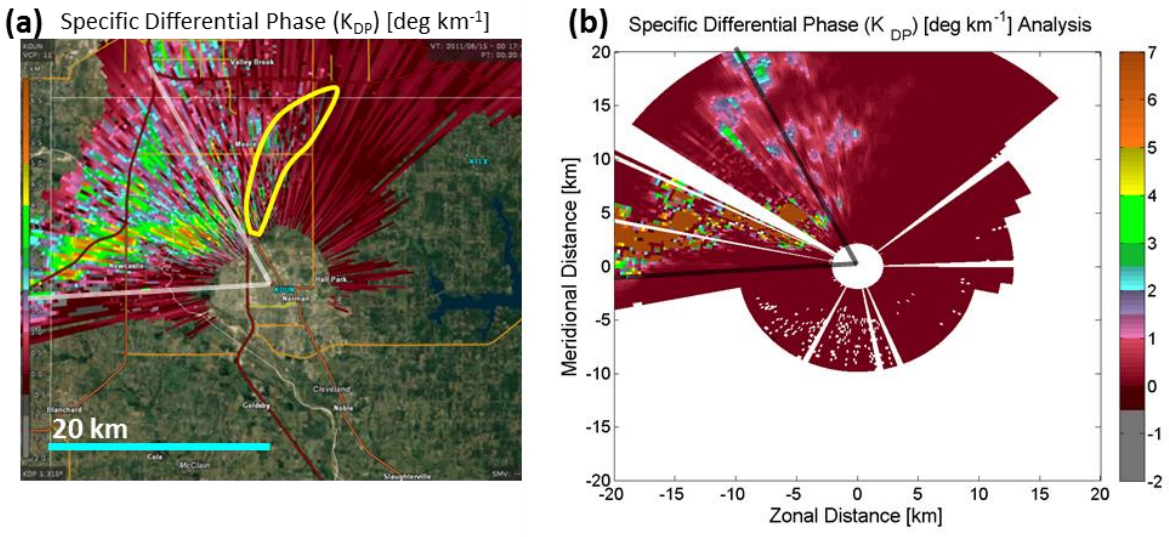


Fig. 8.5. K_{DP} (a) calculated using the slope of a least squares fit and (b) from the variational retrieval using a 5.3° elevation scan of KOUN WSR-88D data from 15 June 2011 at 0020 UTC. The left panel was calculated using GR2Analyst software. The boundaries of the sector with hail contamination are marked by white lines on the left panel and black lines on the right panel. The area highlighted in yellow on the left panel is an area with some negative (unrealistic) K_{DP} values.

Applying the HCA from Chapter 5 provides more insight on why the variational retrieval failed on the western to northwestern sector of the PPI. As shown in Figure 8.6, these radials had radar gates that are classified as RH, which implies there was mixed-phase precipitation on these radials. In addition, as previously mentioned, the HCA also indicates GC/AP and/or BS in some of the other azimuths where no solution was found. These failures are because the observation operators were derived using the T-matrix calculations for *pure rain*.

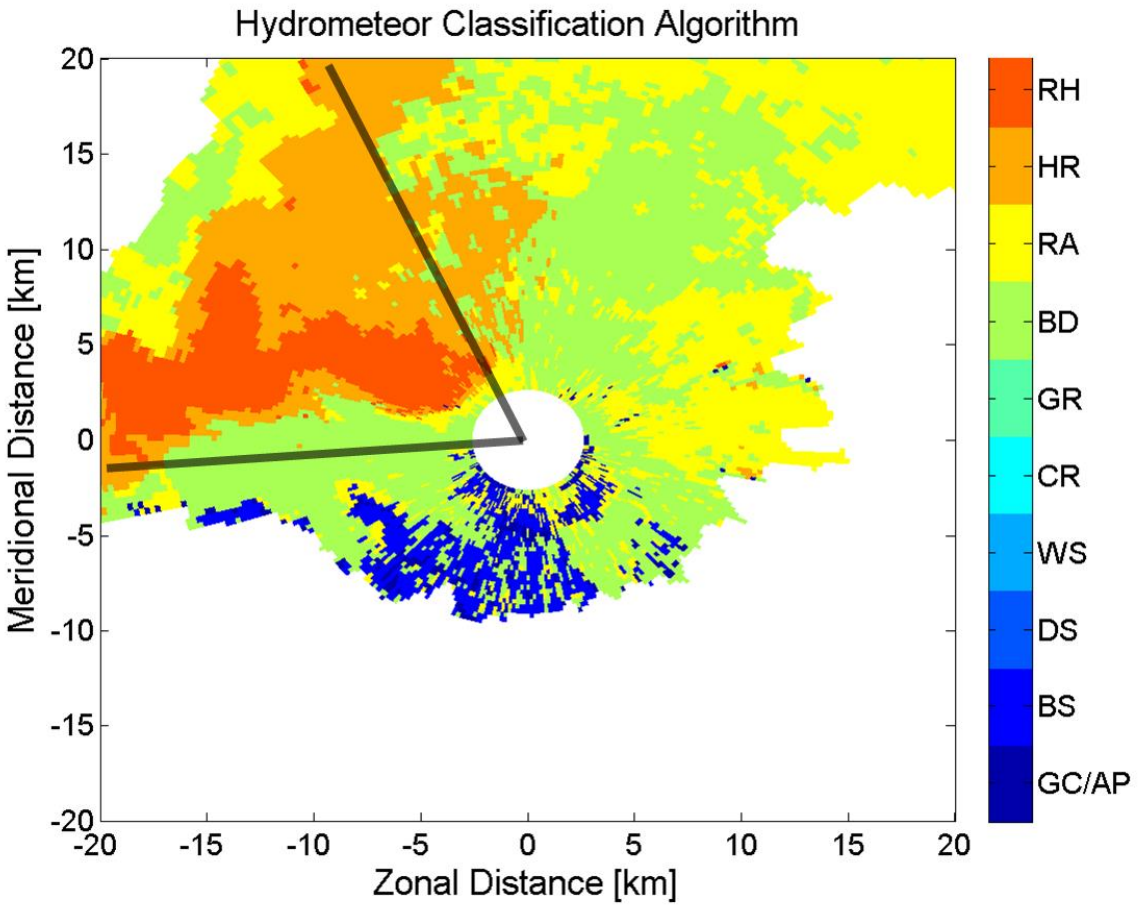


Fig. 8.6. HCA applied to 5.3° elevation scan of KOUN WSR-88D data from 15 June 2011 at 0020 UTC. The boundaries of the sector with hail contamination are marked by the black lines.

On Figures 8.3-8.6, the sector associated with hail contamination is highlighted using the results from the HCA. For operational purposes in the detection of hazardous weather, the failure of the variational retrieval could actually be a tool used to determine where hail is present in a thunderstorm. This would be especially true if the variational retrieval is conducted locally over a set number of simultaneous gates rather than an entire azimuth.

Outside of these areas, the Z_H and Z_{DR} analyses are similar to the observations (Fig. 8.4). The local maxima and minima are near the same locations (with an occasional variation in the magnitude), which results in the same precipitation structure. Some variability in magnitude is

expected because an optimal analysis that utilizes all the information from Z_H, Z_{DR}, and Φ_{DP}. Also, some smoothing occurs because the spatial covariance is taken into account. One noticeable difference is that the peak magnitude of Z_{DR} is tempered when compared to observations. As noted in the single-azimuth experiment, this is because of the dynamic range of D_m that can be calculated through the variational retrieval.

There are also slight discontinuities from azimuth to azimuth. This is likely an artifact from changes in the errors of Φ_{DP} observations from azimuth to azimuth and the subsequent effect on the final Φ_{DP} analysis value. In this study, the Φ_{DP} error distribution is assumed constant across the entire PPI, which may not be the case. The final Φ_{DP} analysis value is dependent on the total sum of W across the entire azimuth. Slight deviations in the final Φ_{DP} analysis value will result in a slight change for the retrieved state variables across the entire azimuth.

8.5. K_{DP} Calculated by Least-squares Fit vs. Analysis

K_{DP} calculated using GR2Analyst and analysis from the variational retrieval are shown in Figure 8.5. GR2Analyst is a radar analysis program that is used operationally to view live or archived Level II radar data. The program calculates K_{DP} similar to the method used by the operational WSR-88D network by finding the slope of a least-squares fit of the filtered Φ_{DP} (Park et al. 2009; Ryzhkov and Zrnić 1996). In addition to least-squares fit, other methods, such as linear programming, have been developed to calculate K_{DP} (e.g., Huang et al. 2017).

In this example, K_{DP} calculated by using a least-squares fit is somewhat noisy and even has some negative values (Fig. 8.5a). This is due to the inherent noisiness of Φ_{DP}. Within areas of pure rain, K_{DP} should always be positive. As previously noted, Φ_{DP} can only monotonically

increase when using the variational retrieval. This is a constraint that comes out of the observation operator. Therefore, negative K_{DP} values cannot exist. Like Z_H and Z_{DR}, Φ_{DP} is smoother and less chaotic in the variational retrieval relative to truth, which allows for smoother K_{DP} (Fig. 8.5b). In addition, this K_{DP} is an optimal analysis that also utilizes information from Z_H and Z_{DR} (in addition to Φ_{DP}). Therefore, it is assumed that K_{DP} estimates are better using the variational retrieval when compared to the least-squares fit method. Better K_{DP} estimates are operationally useful because K_{DP} is better correlated to rainfall rates due to it being unaffected by calibration error and attenuation as well as being more linearly related to rainfall rate (Bringi and Chandrasekar 2001). This gives it utility for quantitative precipitation estimates (QPE).

8.6. Summary

In this chapter, a proposed method for the observation-based variational retrieval of the physical parameters of W and D_m from S-band PRD was developed through the use of parametrized polarimetric radar observation operators and a nonlinear, iterative method.

Applied to the downburst case, it is another method beyond the HCA that utilizes scattering theory to determine the presence of mixed-phase precipitation. Since the observation operators were derived with the assumption of pure rain, the retrieval failed where there was hail contamination. These results match the results of the HCA that was used earlier in the dissertation. Broader applications beyond the analysis of the downburst will be discussed in Chapter 9.

Appendix: Testing the Variational Retrieval on DSD Data and Single Azimuth Radar Data

In this Appendix, the results of several tests using the variational retrieval are shown. The variational retrieval and observation operators are tested by conducting experiments on 2-dimensional video disdrometer (2DVD; Kruger and Krajewski 2002) data collected on 2005 May 13 (Zhang 2015). The 2DVD data are from a quasi-linear convective system (QLCS) that has an estimated storm motion from 16 to 18 m s^{-1} or ~1 km min^{-1}. The 2DVD data are collected for ~4.63 hours; however, only the results for the first 60 min are shown because this is when the leading convective-line of the QLCS passes over the disdrometer and when the most significant increase in Φ_{DP} occurs (i.e., the most notable part of the dataset).

These experiments are conducted on W and D_m that are calculated using the 2DVD data. The goals of the experiments are to investigate the advantages of 1) using the nonlinear solution for the retrieval and 2) including Φ_{DP} observations. In addition, an experiment is conducted to assess the impacts of including random error to observations. These advantages will be discussed in context of the both the retrieval of W and D_m (i.e., the inverse problem) and the estimation of polarimetric radar variables (i.e., the forward problem) to test the observation operators. In other words, the observation operators are tested both going backward from the observations to the state variables and forward from the state variables to observations.

First, the intrinsic or true values for W and D_m are calculated using the 2DVD data. When calculating W and D_m, a 5-point average of the 2DVD data are used to remove noise from the data. Second, Z_H, Z_{DR}, and Φ_{DP} are calculated using the observation operators (8.11), (8.13), and (8.14) and the relationship between Φ_{DP} and K_{DP} (8.27). These calculated polarimetric variables are assumed to be the true observations in these experiments. Third, it is assumed that the time-series of 2DVD data represents a radial of radar data. This is a reasonable assumption because

the storm motion remained nearly steady-state. Based on the storm motion, each minute of 2DVD data represents approximately a 1-km range gate of data. Thus, the entire 60 min of data represents a radial that is 60 km in length. Finally, in all of these experiments, a constant background is calculated using the empirical relationship given in (8.18) and (8.19). The mean of the empirically-derived W and D_m are calculated using the entire radial of data (~4.63 hours). These mean values for W and D_m are used as the constant background.

a. OI vs. Nonlinear

In the first experiment, the OI solution (8.16) is compared to the nonlinear solution (8.17). Both of these solutions only include Z_H and Z_{DR} (Φ_{DP} is not included). The relative advantage of the nonlinear solution over OI is demonstrated in Figure 8.7. For all analyses, the nonlinear solution is closer to the truth. For example, the peak values of W are 0.65 g m^{-3} and 1.58 g m^{-3} for the OI and nonlinear solutions at 20 km, respectively (Fig. 8.7a). The nonlinear solution is closer to the true maximum value of 1.94 g m^{-3}.

For Z_H, there is generally an underestimation of values in the OI solution when compared to the nonlinear solution and truth (Fig. 8.7b). For example, the peak values are ~45 dBZ and ~50 dBZ for the OI and nonlinear solutions at 29 km, respectively. The nonlinear solution is the same as the truth in this case. D_m and Z_{DR} are similar for both the OI and nonlinear solutions with an exception of the peak values (Fig. 8.7c, d). There a slight underestimation on the OI solution at peak values. For example, the true value at 12 km is 3.05 dB for Z_{DR} and 3.00 mm for D_m. This compares to 2.85 dB and 2.80 mm for the OI solution and 3.00 dB and 2.94 mm for the nonlinear solution.

The advantage of the nonlinear solution over OI is also shown by the final value of Φ_{DP}. Since Φ_{DP} is integrated in the along-radial direction, the value at the final gate provides insight on the performance across the entire radial of data. In this experiment, the final value of Φ_{DP} for the OI solution at ~15° is nearly half when compared to the nonlinear solution at ~29° (Fig. 8.7e). The nonlinear solution is very close to the true value, which is 30°. This seems reasonable and intuitive based on the significant underestimation of W across the entire radial with the OI solution.

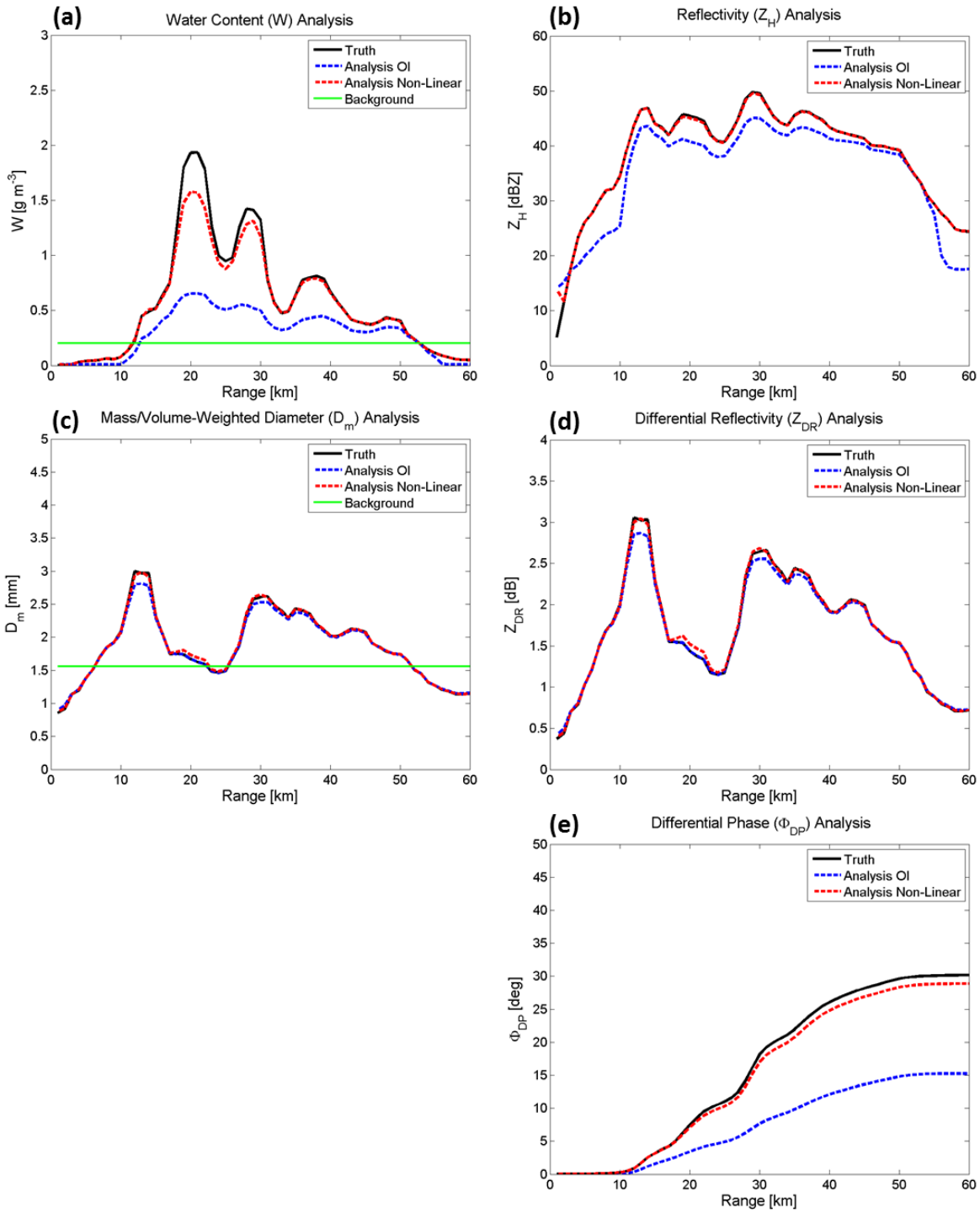


Fig. 8.7. OI analysis and nonlinear analysis compared to the truth for (a) W, (b) Z_{H}, (c) D_{m}, (d) Z_{DR}, and (e) Φ_{DP} using 2DVD data collected on 2005 May 13. The constant background field for W and D_{m} are also shown.

b. Nonlinear without Φ_{DP} vs. Nonlinear with Φ_{DP}

In the second experiment, the nonlinear solution without Φ_{DP} is compared to that with Φ_{DP}. The advantage of including Φ_{DP} in the variational retrieval is shown in Figure 4. The most evident advantage is seen in W, especially with larger values (>1.5 g m^{-3}) (Fig. 8.8a). The peak values of W are 1.58 g m^{-3} and 1.75 g m^{-3} for nonlinear solution without and with Φ_{DP}, respectively. The nonlinear solution with Φ_{DP} is closer to the true maximum value of 1.94 g m^{-3}. For Z_H, D_m, Z_{DR}, the benefits of including Φ_{DP} are negligible (Fig. 8.8b, c, and d). The final value of Φ_{DP} for the nonlinear solution without Φ_{DP} is ~29°, which is close to the nonlinear solution with Φ_{DP} and the truth at ~30° (Fig. 8.8e). When compared to the previous experiment, the final value of Φ_{DP} does not have a significant difference.

Even though most of the analyses show little or no benefit, it is important to note that there is still evidence of some benefit of adding Φ_{DP} in addition to Z_H and Z_{DR} as shown with the increase in the peak W value. This improves results for W that is closer to the true value. In other words, the inclusion of Φ_{DP} is important for the retrieval of larger W values.

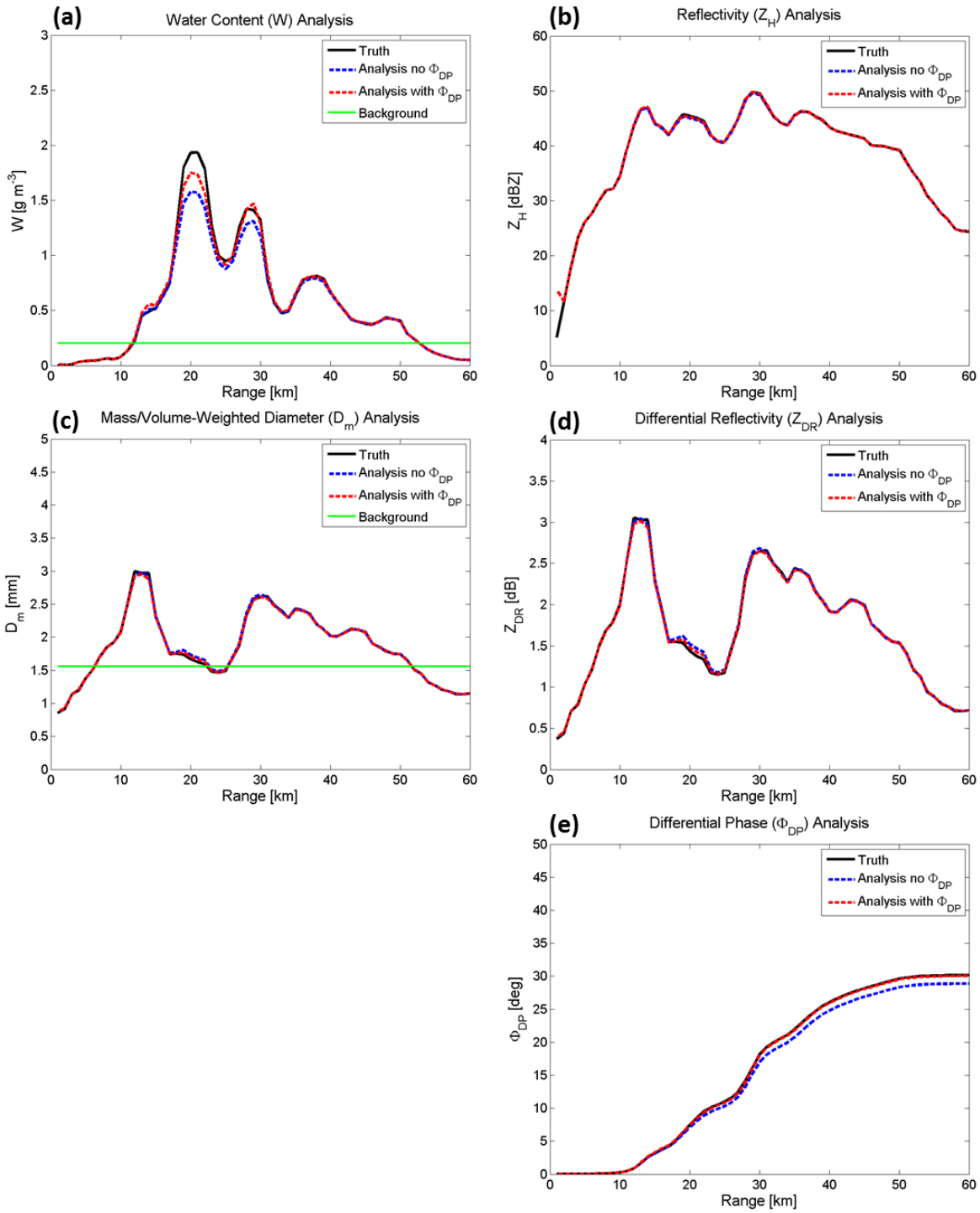


Fig. 8.8. Same panels as Figure 8.7, but with nonlinear analysis without Φ_{DP} and nonlinear analysis with Φ_{DP} compared to the truth.

c. Simulated Observations

In the third experiment, the nonlinear solution with Φ_{DP} is compared to the nonlinear solution with Φ_{DP} with random error added to the observations. Adding random error may result in worse retrievals, which is an important consideration since true radar observations include random error. The random errors included are ±1 dBZ for Z_H, ±0.2 dB for Z_{DR}, and ±5° for Φ_{DP}. These values were chosen because they are used in the covariance matrix of observations errors, as described previously in the chapter.

As shown in Figure 8.9, this experiment demonstrates that the nonlinear variational retrieval still provides a reasonable solution even with random error in the observations. This is especially true when looking at the solution as a whole. As previously mentioned, the best way to assess this is by looking at the final Φ_{DP} value because Φ_{DP} is an integrated quantity. The final value of Φ_{DP} with random error is the same as truth (~30°) (Fig. 8.9e). Therefore, on average, the solution is still reasonable.

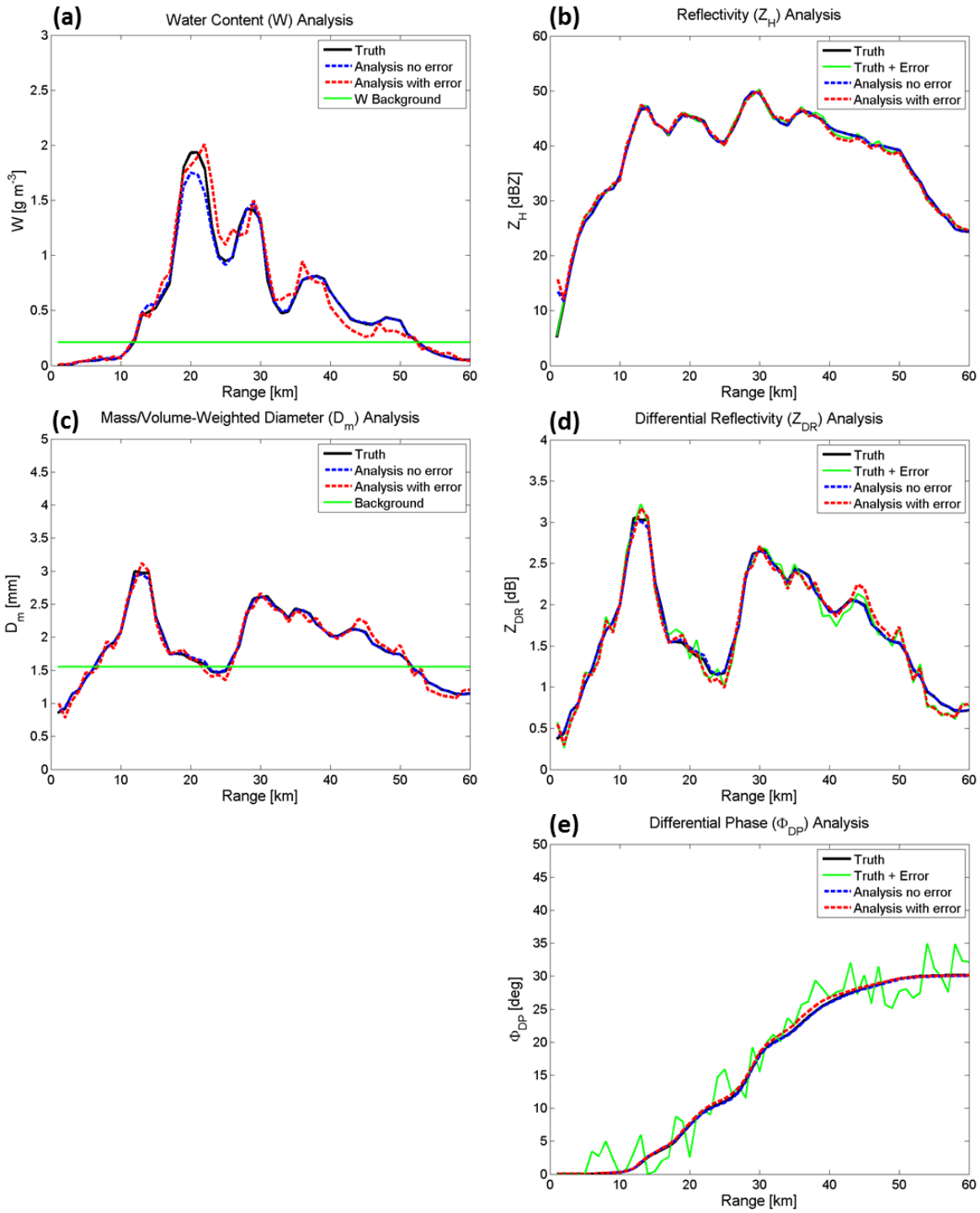


Fig. 8.9. Same panels as Figure 8.7, but with nonlinear analysis without error and nonlinear analysis with random error compared to the truth. The simulated observation (truth + random error) for Z_H, Z_{DR}, and Φ_{DP} are also shown.

d. Summary of 2DVD Experiments

Overall, these experiments demonstrate the advantages of using the nonlinear solution and including Φ_{DP} observations when conducting a variational retrieval using the derived observation operators. The OI method does not provide a good solution when compared to the truth. The assumption with the OI method is that background is a reasonable approximation of true analysis (Kalnay 2003). In these experiments, a constant background is utilized. Therefore, in many cases, the background may not be a reasonable approximation to the true analysis.

It is also demonstrated that the advantage of using the nonlinear solution is more significant than including Φ_{DP} observations. However, including Φ_{DP} observations does add some value, especially for improved peak W estimates. This added value to W does not negatively affect the other variables. Finally, even with the inclusion of random error, a reasonable solution can still be found using the variational retrieval.

In the previous sections, the variational retrieval and observation operators were successfully tested on 2DVD data and simulated observations. The next step is to apply them to real radar data from a single azimuth from the downburst event.

e. Single-azimuth Radar Experiment

The variational retrieval was tested on a single azimuth of radar data before applying it to an entire PPI scan. As previously mentioned, the variational retrieval is solved azimuthally (1-D) to coincide with Φ_{DP} observations. As with the 2DVD data, some assumptions and pre-processing to the data are applied to this experiment. A constant background for W and D_m are calculated using the azimuthal mean of empirical relationship given in (8.18) and (8.19). Also as with 2DVD data, quality-control of the radar data is accomplished through a median filter to

reduce the noise in the data. In addition, some constraints are placed on the radar data. The Z_H minimum is set to 10 dBZ, Z_{DR} is limited to 0.1 to 6 dB, and only positive values of Φ_{DP} are allowed. These constraints are based on the bounds of the observation operators as shown in Figure 1. Finally, a simple attenuation correction is also implemented to the radar data using the differential phase (DP) attenuation correction procedure (Bringi et al. 1990) with coefficients derived in Zhang (2016).

In this experiment, an azimuth (~3.5°) with moderate Z_H (~30 to 50 dBZ) and high ρ_{hv} (>0.98) values is chosen. Based on these observations, the assumption is that only raindrops associated moderate rainfall are present in this azimuth with no hail contamination. This makes it an ideal azimuth to test the variational retrieval. Once W and D_m are solved using the variational retrieval, the observation operators are used to calculate Z_H, Z_{DR} and Φ_{DP} analyses as in the 2DVD experiments.

The W, D_m, Z_H, Z_{DR}, and Φ_{DP} analyses for the single azimuth are shown in Figure 8.10. For comparison, the empirical relationships (8.18) and (8.19) are used to calculate W and D_m. The empirical relationships only depend on Z_H and Z_{DR} and do not account for $\Phi_{DP.}$ Even so, the empirical relationships can be used to qualitatively assess the results of the variational retrieval. The observed values for Z_H, Z_{DR}, and Φ_{DP} are shown as a comparison as well.

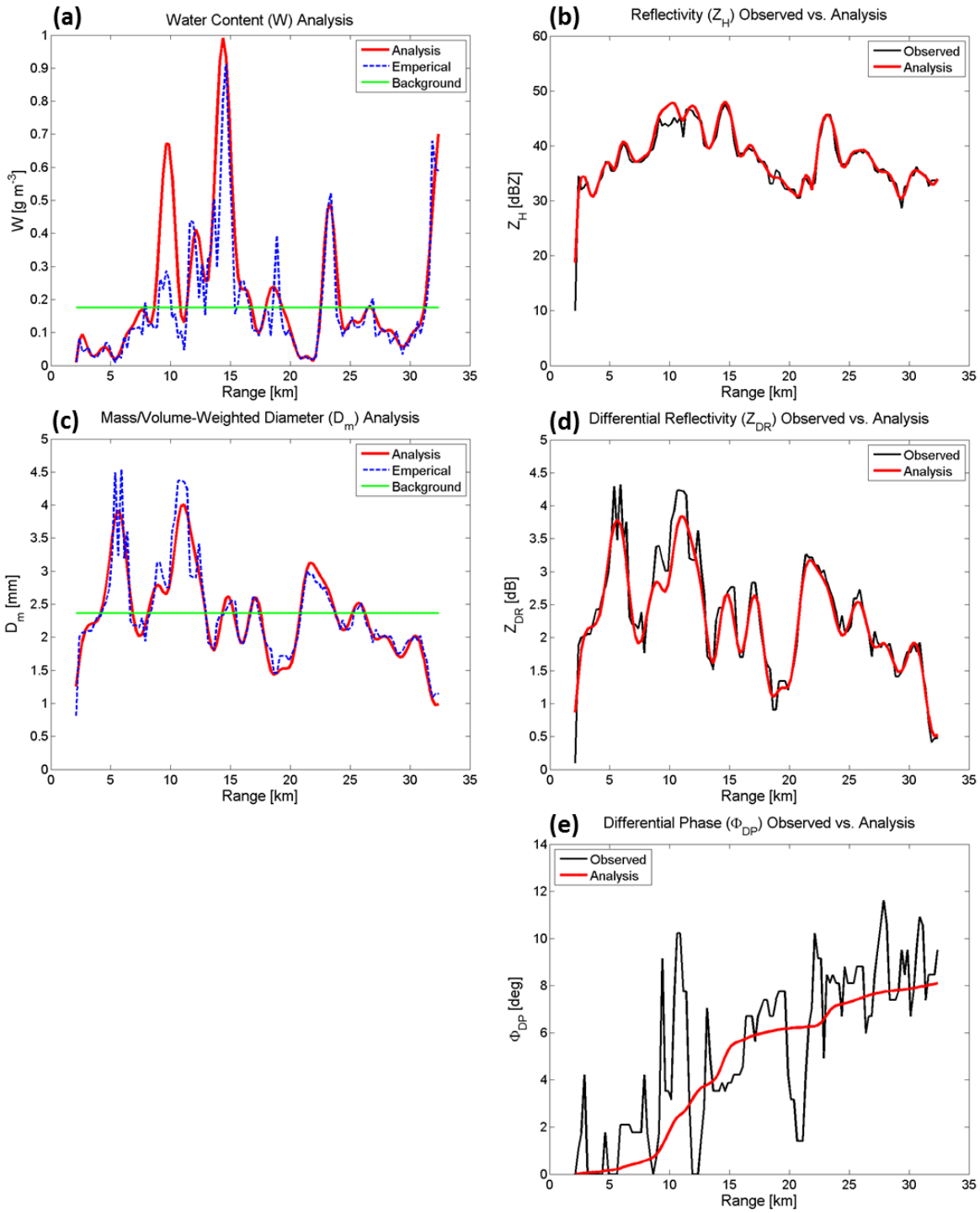


Fig. 8.10. Analysis for (a) W, (b) Z_H, (c) D_m, (d) $Z_{DR,}$ and (e) Φ_{DP} by applying the variational retrieval on a single azimuth of 5.3° elevation scan of KOUN WSR-88D data from 15 June 2011 at 0020 UTC. The observed values for Z_H, $Z_{DR,}$ and Φ_{DP} are plotted for comparison. The empirical relationship and constant background field for W and D_m are shown as well.

For W, the variational retrieval is smoother than the empirical relationship (Fig. 8.10a). This is reasonable because the variational retrieval takes account for the spatial covariance, which is a function of the spatial decorrelation length. The variational retrieval would be less (more) smooth with a smaller (larger) spatial decorrelation length. The local maxima and minima for W are at approximately the same range; however, the magnitudes of these maxima and minima are sometimes different. For example, at ~9 to 10 km range, the maximum magnitude of the difference between the two W values is 0.43 g m^{-3}.

This range is also where there is a noticeable difference between the Z_H analysis and observations (Fig. 8.10b). At the same range, the maximum magnitude of the difference between Z_H analysis and observations is 3.8 dB. The Φ_{DP} observations are essentially increasing W values beyond simply what the Z_H values would suggest in this range, which results in larger Z_H values in the analysis to keep it consistent with the Z_H observation operator. If the $\sigma_{\Phi DP}$ was increased (decreased), the W values in this range would decrease (increase) because of decreasing (increasing) influence of Φ_{DP} with more (less) weight given to Z_H. Outside of this range, the Z_H analysis is fairly close to the Z_H observations (albeit smoother).

For the D_m analysis (Fig. 8.10c), the variational retrieval is smoother than the empirical relationship as well and the peak values are less than the empirical relationship at a range of ~6 km and ~11 km. This occurs because the observation operators, and more specifically the T-Matrix calculations, have a smaller dynamic range for D_m. Consequently, the reduction of D_m also results in a coincident reduction in Z_{DR} as well (Fig. 8.6d). Outside these areas, the Z_{DR} analysis is fairly close to the Z_{DR} observations.

When comparing W with Φ_{DP} at this range (Fig. 8.10a, e), it is evident that the Φ_{DP} has a positive impact in modulating W. The Φ_{DP} analysis has a relatively steep slope in this range (i.e.,

relatively large K_{DP}), which is why W is greater than in the empirical relationship that does not have the contribution from Φ_{DP}.

It is also noteworthy that the Φ_{DP} analysis can only monotonically increase when using the variational retrieval (Fig. 8.10e). This is because only positive K_{DP} values are allowed in the observation operator. As shown, Φ_{DP} observations are noisy and chaotic when compared to Z_H and Z_{DR} observations, which is why $\sigma_{\Phi DP}$ is relatively large when compared to σ_{ZH} and σ_{ZDR}. The variational retrieval provides a method to calculate a smoother, monotonically increasing Φ_{DP} while accounting for the Z_H and Z_{DR} observations. This is the characteristic that would be expected for Φ_{DP} in a pure-rain azimuth with no hail contamination at S-band.

In addition, because the Φ_{DP} analysis can only monotonically increase with range, Φ_{DP} observations serve as a constraint for the variational retrieval. This is because the final Φ_{DP} analysis value is dependent on the total sum of W across the entire azimuth. The other two observations, Z_H and Z_{DR}, are independent from gate-to-gate.

Overall, the single-azimuth experiment on an area of moderate rainfall was successful. The locations of local maxima and minima for W, D_m, Z_H, and Z_{DR} are similar to either the empirical formula or the observations with some differences in magnitude. These differences can be accounted for mostly with the addition of Φ_{DP} observations (in the case of W and Z_H) and the limitation of T-Matrix calculations used in the observation operators (in the case of D_m and Z_{DR}). Finally, these results demonstrate that the variational retrieval has utility in calculating a smoother, monotonically increasing (more physically-representing) Φ_{DP}.

Chapter 9 : Summary, Conclusions, and Future Work

9.1 Summary and Conclusions

The characterization and analysis of the dynamics and microphysics of a significant, wet downburst was conducted using various observations and analysis methods in this dissertation. The downburst was a macroburst in size with surface winds in excess of 35 m s^{-1} (>80 mph) and hailstones in excess of 4 cm diameter. Surface observations from the Oklahoma Mesonet measured a 6.6-hPa pressure rise that was coincident with an intense peak rain rate of 213 mm hr^{-1} at the center of the downburst. The downburst was unique due to the combination of its size, longevity, and intense precipitation rate.

For the first time documented, an HCA was applied to PRD to gain further understanding of the microphysical evolution of a downburst (Chapter 5). The HCA analyses were utilized to develop a conceptual model that characterizes the hydrometeor evolution of the parent downburst thunderstorm. Through the analyses, it was seen that graupel aloft made a transition to a nearly all rain and hail mixture. This large area of mixed rain and hail eventually descended to the ground, causing the downburst. Increased Z_{DR} and decreased ρ_{hv} at the bottom of this mixed-phase precipitation core were assumed to be due to the increased presence of melting hailstones. This observation indicated that melting of hailstones contributed to some of the negative buoyancy in the downburst.

The mixed-phase precipitation was coincident with a vertical velocity of ~-20 m s^{-1}, which was found through dual-Doppler analysis. Using this value and Mesonet observations, it was estimated that the thermodynamic part had a much greater contribution to the surface mesohigh than the dynamic part.

Rapid-scan radar data from RaXPol captured the quick expansion of the downburst as it moved to the east-southeast toward Norman (Chapter 6). Through analysis of the RaXPol data, the downburst was found to have grown from a microburst at ~2.1 km horizontal scale to a macroburst at ~6.4 km in less than 7 min. As the downburst expanded, its near-surface horizontal winds intensified from 23 m s^{-1} to 42 m s^{-1}.

The rapid-scan observations also captured the development of features such as a horizontal rotor, vertical vortices, multiple gust front heads, and an elevated nose on the leading edge of the gust front. The horizontal rotor may have split the hail core into two segments as indicated by reduced ρ_{hv} separating around the rotor and a localized Z_H minimum collocated with the rotor. Along the leading edge of the gust front, there was a line of small vertical vortices. There was a slight reduction in ρ_{hv} and Z_{DR} along with enhanced σ_v associated with these vortices. These vertical vortices may have corresponded to small gustnadoes. There were also three distinct gust front heads, each with a localized wind maximum, behind the initial gust front. There were three wind shifts $\geq 15°$ observed by the Mesonet that may have corresponded to these gust front heads. The elevated nose was at ~75 m ARL, which resulted in a 2 to 3 min lag from the most intense winds being measured at the surface.

RaXPol also captured several descending surges of mixed-phase precipitation cores aloft, indicated by a reduction in ρ_{hv}. These descending cores provided a continued stream of precipitation loading and melting hail, which may have aided in the continued expansion and intensity of the downburst.

The presence of mixed-phase precipitation was substantiated through a dual-frequency comparison between KOUN and RaXPol (Chapter 7) and the use of a variational retrieval (Chapter 8). From the dual-frequency comparison, it was seen that there is increased sensitivity

to wet hail for ρ_{hv} at X-band when compared to S-band. This reduction in ρ_{hv} is attributed to increased variance of δ due to resonance effects. The comparison also demonstrated the benefits of ρ_{hv} at X-band when compared to Z_H and Z_{DR} due to its immunity to attenuation.

Finally, when applied to the downburst case, the variational retrieval was another method beyond the HCA that utilizes scattering theory to determine the presence of mixed-phase precipitation (Chapter 8). Since the observation operators were derived with the assumption of pure rain, the retrieval failed where there was hail contamination. These results matched the results of the HCA

Using the results from this study, some conclusions can be inferred on the dynamics of the downburst. As noted, the primary driving mechanisms for the downward motion due to buoyancy in downbursts are 1) thermal buoyancy through evaporation and/or melting of hydrometeors and 2) precipitation loading.

From back of the envelope calculations (Chapter 4), it appeared that thermal buoyancy may have played a slightly larger role in the downburst than precipitation loading; however, these terms were not steady-state during the duration of the downburst event. In reality, the magnitudes of these terms likely varied during the downburst event.

Initially, thermal buoyancy may have dominated with a dry subcloud layer and a high LCL height. The potential for thermal buoyancy may have decreased toward the latter part of the downburst event with the decreasing evaporation due to the environment becoming more saturated. From the RaXPol data, it was seen that as the downburst grew in size and intensity that there was an increase in the stream of descending mixed-phase precipitation well-behind the gust front. This implies precipitation loading may have had more of an effect during this part of the downburst event as the environment may have been closer to saturation. However, mixed-phase

precipitation may have also contributed to negative thermal buoyancy from melting hail since melting could still occur even if the environment was saturated. From the KOUN data it was seen that there was some melting of hail near the surface.

Therefore, it can be speculated that on average, both thermal buoyancy and precipitation loading may have had approximately the same order of magnitude effect on the downburst's downward acceleration with perhaps varied degrees of influence through the evolution of the downburst. In the developing stage of the downburst, thermal buoyancy through evaporation may have dominated. At the latter stages, descending surges of mixed-phase precipitation provided a continued source of *both* precipitation loading and melting hail that aided in the continued expansion, intensity, and longevity of the downburst.

9.2 Broader Impacts and Future Work

There are some operational considerations that came out of this study. It was shown that important precursors (i.e., rapid hail growth aloft) of the developing downburst was evident with up to 30-min lead time before surface wind gust, suggesting the important value of PRD for nowcasting and warning of severe downburst events. This especially is important when the environment is very favorable for downbursts (as was the case in this study).

This study also demonstrates the importance of high-resolution, rapid-scan volumetric radar observations in capturing spatiotemporal evolution of downbursts. This is an important consideration when evaluating future radar systems for operational use in the detection of rapidly-changing hazardous weather.

Finally, the variational retrieval also has broader impacts beyond the scope of the project and even downbursts. The simple observation operators used in the variational retrieval are

advantageous because they include relevant physics, are numerically efficient, and have easily calculated first derivatives. These parameters can be easily assimilated to NWP because are directly related to the prognostic physics variables. The variational method develops a framework that utilizes proven techniques from the data assimilation community. While the background state may not provide a significant advantage for 1-D (azimuth) retrieval, this method is generalized so that it can be expanded to larger retrieval problems such as a 2-D or 3-D gridded retrieval that may result in an underdetermined problem (in which case a background field is necessary).

Future research on the variational retrieval includes deriving the observation operators for other radar frequencies (e.g., X- and C-band) and incorporating observation operators for other hydrometer types such as hail. The inclusion of other hydrometeors is important for operational use, including the assessment of thunderstorms that may potentially produce wet downbursts. Essentially, if other hydrometeors are accounted for, this method would result in a more quantitative HCA.

References

Atkins, N. T., and R. M. Wakimoto, 1991: Wet microburst activity over the southeastern United States: Implications for forecasting. *Wea. Forecasting*, **6,** 470-482.

Atlas, D., C. W. Ulbrich, and C. R. Williams, 2004: Physical origin of a wet microburst: Observations and theory. *J. Atmos. Sci.,* **61,** 1186-1195.

Bluestein, H. B., C. C. Weiss, and A. L. Pazmany, 2003: Mobile Doppler radar observations of a tornado in a supercell near Bassett, Nebraska, on 5 June 1999. Part I: Tornadogenesis. *Mon. Wea. Rev.,* **131,** 2954-2967.

Brandes, E. A., and K. Ikeda, 2004: Freezing-level estimation with polarimetric radar. *J. Appl. Meteor.,* **43,** 1541-1553.

Brandes, E. A., G. Zhang, and J. Vivekanandan, 2002: Experiments in rainfall estimation with a polarimetric radar in a subtropical environment. *J. Appl. Meteor.,* **41,** 674-685.

Bringi, V. N., and V. Chandrasekar, 2001: *Polarimetric Doppler Weather Radar: Principles and Applications.* Cambridge University Press, 636 pp.

Bringi, V. N., V. Chandrasekar, N. Balakrishnan, and D. S. Zrnić, 1990: An examination of propagation effects in rainfall on radar measurements at microwave frequencies. *J. Atmos. Oceanic Technol.,* **7,** 829-840.

Brock, F. V., K. C. Crawford, R. L. Elliott, G. W. Cuperus, S. J. Stadler, H. L. Johnson, and M. D. Eilts, 1995: The Oklahoma Mesonet: A technical overview. *J. Atmos. Oceanic Technol.,* **12,** 5-19.

Cao, Q., G. Zhang, and M. Xue, 2013: A variational approach for retrieving raindrop size distribution from polarimetric radar measurements in the presence of attenuation. *J. Appl. Meteor. Climatol.*, **52,** 169-185.

Charba, J., 1974: Application of gravity current model to analysis of squall-line gust front. *Mon. Wea. Rev.*, **102,** 140-156.

Doswell, C. A., III, 1985: The operational meteorology of convective weather. Vol. II: Storm scale analysis. NOAA Tech. Memo. ERL ESG-15, 240 pp.

Droegemeier, K. K., and R. B. Wilhelmson, 1987: Numerical smulation of thunderstorm outflow dynamics. Part I: Outflow sensitivity experiments and turbulence dynamics. *J. Atmos. Sci.*, **44,** 1180-1210.

Eliassen, A., 1954: Provisional report on calculation of spatial covariance and autocorrelation of the pressure field, 12 pp.

Emanuel, K. A., 1994: *Atmospheric Convection.* Oxford University Press, 883 pp.

Fu, D., and X. Guo, 2007: Numerical study on a severe downburst-producing thunderstorm on 23 August 2001 in Beijing. *Adv. in Atmos. Sci.* , **24,** 227-238.

——, 1978: *Manual of downburst identification for project NIMROD.* SMRP Rep. 156, University of Chicago, 104 pp.

——, 1981: Tornadoes and downbursts in the context of generalized planetary scales. *J. Atmos. Sci.*, **38,** 1511-1534.

——, 1985: *The downburst: microburst and macroburst.* SMRP Rep. 210, University of Chicago, 122 pp.

——, 1986: *DFW microburst on August 2, 1985.* SMRP Rep. 217, University of Chicago, 154 pp.

Fujita, T. T., and F. Caracena, 1977: An analysis of three weather-related aircraft accidents. *Bull. Amer. Meteor. Soc.*, **58,** 1164-1181.

Fujita, T. T., and H. R. Byers, 1977: Spearhead echo and downburst in the crash of an airliner. *Mon. Wea. Rev.*, **105,** 129-146.

Fujita, T. T., and R. M. Wakimoto, 1981: Five scales of airflow associated with a series of downbursts on 16 July 1980. *Mon. Wea. Rev.*, **109,** 1438-1456.

Gandin, L., 1963: *Objective Analysis of Meteorological Fields.* Gidromet, Leningrad, 285 pp.

Gao, J., M. Xue, A. Shapiro, and K. K. Droegemeier, 1999: A variational method for the analysis of three-dimensional wind fields from two Doppler radars. *Mon. Wea. Rev.*, **127,** 2128-2142.

Gao, J., M. Xue, A. Shapiro, Q. Xu, and K. K. Droegemeier, 2001: Three-dimensional simple adjoint velocity retrievals from single-Doppler radar. *J. Atmos. Oceanic Technol.*, **18,** 26-38.

Giangrande, S. E., J. M. Krause, and A. V. Ryzhkov, 2008: Automatic designation of the melting layer with a polarimetric prototype of the WSR-88D radar. *J. Appl. Meteor. Climatol.*, **47,** 1354-1364.

Goff, R. C., 1976: Vertical structure of thunderstorm outflows. *Mon. Wea. Rev.*, **104,** 1429-1440.

Hall, M. P. M., J. W. F. Goddard, and S. M. Cherry, 1984: Identification of hydrometeors and other targets by dual-polarization radar. *Radio Sci.*, **19,** 132-140.

Harimaya, T., 1976: The embryo and formation of graupel. *J. Meteor. Soc. Japan*, **54,** 42-51.

Hjelmfelt, M. R., 1988: Structure and life cycle of microburst outflows observed in Colorado. *J. Appl. Meteor.*, **27,** 900-927.

Hogan, R. J., 2007: A variational scheme for retrieving rainfall rate and hail reflectivity fraction from polarization radar. *J. Appl. Meteor. Climatol.*, **46,** 1544-1564.

Houser, J. L., H. B. Bluestein, and J. C. Snyder, 2015: Rapid-scan, polarimetric, Doppler radar observations of tornadogenesis and tornado dissipation in a tornadic supercell: The "El Reno, Oklahoma" storm of 24 May 2011. *Mon. Wea. Rev.*, **143,** 2685-2710.

Houze, R. J., 2014: *Cloud Dynamics.* 2nd ed. Academic Press, 496 pp.

Hoxit, L. R., C. F. Chappell, and J. Michael Fritsch, 1976: Formation of mesolows or pressure troughs in advance of cumulonimbus clouds. *Mon. Wea. Rev.*, **104,** 1419-1428.

Huang, H., G. Zhang, K. Zhao, and S. E. Giangrande, 2017: A hybrid method to estimate specific differential phase and rainfall with linear programming and physics constraints. *IEEE Trans. Geosci. Remote Sens.*, **55,** 96-111.

Huang, X. Y., 2000: Variational analysis using spatial filters. *Mon. Wea. Rev.*, **128,** 2588-2600.

Ide, K., P. Courtier, M. Ghil, and A. C. Lorenc, 1997: Unified notation for data assimilation: Operational, sequential and variational. *J.Meteor. Soc. Japan*, **75,** 181-189.

Jung, Y., G. Zhang, and M. Xue, 2008: Assimilation of simulated polarimetric radar data for a convective storm using the Ensemble Kalman Filter. Part I: Observation operators for reflectivity and polarimetric variables. *Mon. Wea. Rev.*, **136,** 2228-2245.

Kalnay, E., 2003: *Atmospheric Modeling, Data Assimilation, and Predictability.* Cambridge University Press, 341 pp.

Kessinger, C. J., D. B. Parsons, and J. W. Wilson, 1988: Observations of a storm containing misocyclones, downbursts, and horizontal vortex circulations. *Mon. Wea. Rev.*, **116,** 1959-1982.

Knight, N. C., 1981: The climatology of hailstone embryos. *J. Appl. Meteor.*, **20,** 750-755.

Koch, S. E., 1984: The role of an apparent mesoscale grontogenetic virculation in squall line initiation. *Mon. Wea. Rev.*, **112,** 2090-2111.

Kosiba, K., J. Wurman, Y. Richardson, P. Markowski, P. Robinson, and J. Marquis, 2013: Genesis of the Goshen County, Wyoming, Tornado on 5 June 2009 during VORTEX2. *Mon. Wea. Rev.*, **141,** 1157-1181.

Kumjian, M. R., and A. V. Ryzhkov, 2008: Polarimetric sgnatures in supercell thunderstorms. *J. Appl. Meteor. Climatol.*, **47,** 1940-1961.

Kumjian, M. R., S. M. Ganson, and A. V. Ryzhkov, 2012: Freezing of raindrops in deep convective updrafts: A microphysical and polarimetric model. *J. Atmos. Sci.*, **69,** 3471-3490.

Kuster, C. M., P. L. Heinselman, and T. J. Schuur, 2016: Rapid-update radar observations of downbursts occurring within an intense multicell thunderstorm on 14 June 2011. *Wea. Forecasting*, **31,** 827-851.

Lamb, D., and J. Verlinde, 2011: *Physics and Chemistry of Clouds.* Cambridge University Press, 584 pp.

Laroche, S., and I. Zawadzki, 1994: A variational analysis method for retrieval of three-dimensional wind field from single-Doppler radar data. *J. Atmos. Sci.*, **51,** 2664-2682.

Lawless, A. S., S. Gratton, and N. K. Nichols, 2005a: An investigation of incremental 4D-Var using non-tangent linear models. *Quart. J. Roy. Meteor. Soc.*, **131,** 459-476.

——, 2005b: Approximate iterative methods for variational data assimilation. *Int. J. Numer. Methods Fluids*, **47,** 1129-1135.

Lee, B. D., and R. B. Wilhelmson, 1997: The numerical simulation of nonsupercell tornadogenesis. Part II: Evolution of a family of tornadoes along a weak outflow boundary. *J. Atmos. Sci.*, **54,** 2387-2415.

Lim, S., V. Chandrasekar, and V. N. Bringi, 2005: Hydrometeor classification system using dual-polarization radar measurements: Model improvements and in situ verification. *IEEE Trans. Geosci. Remote Sens.*, **43,** 792-801.

Lin, Y.-L., R. D. Farley, and H. D. Orville, 1983: Bulk parameterization of the snow field in a cloud model. *J. Climate Appl. Meteor.*, **22,** 1065-1092.

Liu, H., and V. Chandrasekar, 2000: Classification of hydrometeors based on polarimetric radar measurements: Development of fuzzy logic and neuro-fuzzy systems, and in situ verification. *J. Atmos. Oceanic Technol.*, **17,** 140-164.

Loney, M. L., D. S. Zrnić, J. M. Straka, and A. V. Ryzhkov, 2002: Enhanced polarimetric radar signatures above the melting level in a supercell storm. *J. Appl. Meteor.*, **41,** 1179-1194.

Lorenc, A. C., 1986: Analysis methods for numerical weather prediction. *Quart. J. Roy. Meteor. Soc.*, **112,** 1177-1194.

Mahale, V. N., G. Zhang, and M. Xue, 2014: Fuzzy logic classification of S-Band polarimetric radar echoes to identify three-body scattering and improve data quality. *J. Appl. Meteor. Climatol.*, **53,** 2017-2033.

Markowski, P., and N. Dotzek, 2010: Comments on "Proposed conceptual taxonomy for proper identification and classification of tornado events". *Wea. Forecasting*, **25,** 338-340.

Marquis, J., Y. Richardson, J. Wurman, and P. Markowski, 2008: Single- and dual-Doppler analysis of a tornadic vortex and surrounding storm-scale flow in the Crowell, Texas, supercell of 30 April 2000. *Mon. Wea. Rev.*, **136,** 5017-5043.

McCann, D. W., 1994: WINDEX—A new index for forecasting microburst potential. *Wea. Forecasting*, **9,** 532-541.

McPherson, R. A., and Coauthors, 2007: Statewide monitoring of the mesoscale snvironment: A technical update on the Oklahoma Mesonet. *J. Atmos. Oceanic Technol.*, **24,** 301-321.

Melnikov, V. M., and D. S. Zrnić, 2007: Autocorrelation and cross-correlation estimators of polarimetric variables. *J. Atmos. Oceanic Technol.*, **24,** 1337-1350.

Milbrandt, J. A., and M. K. Yau, 2005: A multimoment bulk microphysics parameterization. Part I: Analysis of the role of the spectral shape parameter. *J. Atmos. Sci.*, **62,** 3051-3064.

Morris, D. A., and M. Shafer, 1996: Detailed surface observations during the Lahoma hail and windstorm. *18th Conf. on Severe Local Storms*, San Francisco, CA.

Morrison, H., J. A. Curry, and V. I. Khvorostyanov, 2005: A new double-moment microphysics parameterization for application in cloud and climate models. Part I: Description. *J. Atmos. Sci.*, **62,** 1665-1677.

National Center for Atmospheric Research, 1995: *REORDER Installation and Use Manual for the Unix Version.*

——, 1998: *CEDRIC: Custom Editing and Display of Reduced Information in Cartesian Space.*

National Transportation Safety Board, 1983: Aircraft accident report: Pan American World Airways, Inc., Clipper 759, Boeing 727-235, N4737, New Orleans International Airport, Kenner, Louisiana, July 9, 1982, 113 pp.

National Weather Service, cited 2018: NWS Directives 10-511 WFO Severe Weather Products Specification. [Available online at http://www.nws.noaa.gov/directives/sym/pd01005011curr.pdf.]

NOAA/NCDC, cited 2016: Storm events database. [Available online at http://www.ncdc.noaa.gov/stormevents.]

Office of the Federal Coordinator for Meteorological Services and Supporting Research, 2016: Doppler radar meteorological observations. Part A—System concepts responsibilities and procedures. *Federal Meteorological Handbook No. 11*.

Oklahoma Climate Survey, cited 2016: Mesonet surface observation data. [Available online at https://www.mesonet.org/index.php/site/contact.]

Park, H. S., A. V. Ryzhkov, D. S. Zrnić, and K.-E. Kim, 2009: The hydrometeor classification algorithm for the polarimetric WSR-88D: Description and application to an MCS. *Wea. Forecasting*, **24,** 730-748.

Pazmany, A. L., J. B. Mead, H. B. Bluestein, J. C. Snyder, and J. B. Houser, 2013: A mobile rapid-scanning X-band polarimetric (RaXPol) Doppler radar system. *J. Atmos. Oceanic Technol.*, **30,** 1398-1413.

Proctor, F. H., 1988: Numerical simulations of an isolated microburst. Part I: Dynamics and structure. *J. Atmos. Sci.*, **45,** 3137-3160.

——, 1989: Numerical simulations of an isolated microburst. Part II: Sensitivity experiments. *J. Atmos. Sci.*, **46,** 2143-2165.

Pruppacher, H. R., and D. J. Klett, 2010: *Microphysics of Clouds and Precipitation.* 2nd ed. Springer Netherlands, 954 pp.

Qiu, C.-J., and Q. Xu, 1992: A simple adjoint method of wind analysis for single-Doppler data. *J. Atmos. Oceanic Technol.*, **9,** 588-598.

Richter, H., J. Peter, and S. Collis, 2014: Analysis of a destructive wind storm on 16 November 2008 in Brisbane, Australia. *Mon. Wea. Rev.*, **142,** 3038-3060.

Roberts, R. D., and J. W. Wilson, 1989: A proposed microburst nowcasting procedure using single-Doppler radar. *J. Appl. Meteor.*, **28,** 285-303.

Rodgers, C. D., 2000: *Inverse Methods for Atmospheric Sounding.* World Scientific, 256 pp.

Rotunno, R., and J. Klemp, 1985: On the rotation and propagation of simulated supercell thunderstorms. *J. Atmos. Sci.*, **42,** 271-292.

Rotunno, R., J. B. Klemp, and M. L. Weisman, 1988: A theory for strong, long-lived squall lines. *J. Atmos. Sci.*, **45,** 463-485.

Ryzhkov, A., and D. Zrnić, 1996: Assessment of rainfall measurement that uses specific differential phase. *J. Appl. Meteor.*, **35,** 2080-2090.

Ryzhkov, A. V., 2007: The impact of beam broadening on the quality of radar polarimetric data. *J. Atmos. Oceanic Technol.*, **24,** 729-744.

Ryzhkov, A. V., D. S. Zrnic, J. C. Hubbert, V. N. Bringi, J. Vivekanandan, and E. A. Brandes, 2002: Polarimetric radar observations and interpretation of co-cross-polar correlation coefficients. *J. Atmos. Oceanic Technol.*, **19,** 340-354.

Saxion, D. S., and R. L. Ice, 2012: New science for the WSR-88D: Status of the dual-polarization upgrade. *28th Conf. on Interactive Information Processing Systems*, New Orleans, LA.

Scharfenberg, K. A., 2003: Polarimetric radar signatures in microburst-producing thunderstorms. *31st Int. Conf. on Radar Meteorology*, Seattle, WA.

Schlesinger, R. E., 1980: A three-dimensional numerical model of an isolated thunderstorm. Part II: Dynamics of updraft splitting and mesovortex couplet evolution. *J. Atmos. Sci.*, **37,** 395-420.

Simpson, J. E., 1969: A comparison between laboratory and atmospheric density currents. *Quart. J. Roy. Meteor. Soc.*, **95,** 758-765.

Skinner, P. S., C. C. Weiss, J. L. Schroeder, L. J. Wicker, and M. I. Biggerstaff, 2011: Observations of the surface boundary structure within the 23 May 2007 Perryton, Texas, supercell. *Mon. Wea. Rev.*, **139,** 3730-3749.

Snyder, J. C., H. B. Bluestein, G. Zhang, and S. J. Frasier, 2010: Attenuation correction and hydrometeor classification of high-resolution, X-band, dual-polarized mobile radar measurements in severe convective storms. *J. Atmos. Oceanic Technol.*, **27,** 1979-2001.

Snyder, J. C., H. B. Bluestein, V. Venkatesh, and S. J. Frasier, 2013: Observations of polarimetric signatures in supercells by an X-Band mobile Doppler radar. *Mon. Wea. Rev.*, **141,** 3-29.

Snyder, J. C., A. V. Ryzhkov, M. R. Kumjian, A. P. Khain, and J. Picca, 2015: A Z_{DR} column detection algorithm to examine convective storm updrafts. *Wea. Forecasting*, **30,** 1819-1844.

Srivastava, R. C., 1985: A simple model of evaporatively driven downdraft: Application to microburst downdraft. *J. Atmos. Sci.*, **42,** 1004-1023.

——, 1987: A model of intense downdrafts driven by the melting and evaporation of precipitation. *J. Atmos. Sci.*, **44,** 1752-1774.

Straka, J. M., and D. S. Zrnić, 1993: An algorithm to deduce hydrometeor types and contents from multiparameter radar data. *26th Conf. on Radar Meteorology*, Norman, OK.

Straka, J. M., D. S. Zrnić, and A. V. Ryzhkov, 2000: Bulk hydrometeor classification and quantification using polarimetric radar data: Synthesis of relations. *J. Appl. Meteor.*, **39,** 1341-1372.

Stull, R., 2017: *Practical Meteorology: An Algebra-based Survey of Atmospheric Science.* University of British Columbia, 926 pp.

Sun, J., D. W. Flicker, and D. K. Lilly, 1991: Recovery of three-dimensional wind and temperature fields from simulated single-Doppler radar data. *J. Atmos. Sci.*, **48,** 876-890.

Suzuki, S.-i., T. Maesaka, K. Iwanami, R. Misumi, S. Shimizu, and M. Maki, 2010: Multi-parameter radar observation of a downburst storm in Tokyo on 12 July 2008. *SOLA*, **6,** 53-56.

Tanamachi, R. L., and P. L. Heinselman, 2016: Rapid-scan, polarimetric observations of central Oklahoma severe storms on 31 May 2013. *Wea. Forecasting*, **31,** 19-42.

Tuttle, J. D., V. N. Bringi, H. D. Orville, and F. J. Kopp, 1989: Multiparameter radar study of a microburst: Comparison with model results. *J. Atmos. Sci.*, **46,** 601-620.

Vivekanandan, J., D. S. Zrnic, S. M. Ellis, R. Oye, A. V. Ryzhkov, and J. Straka, 1999: Cloud microphysics retrieval using S-band dual-polarization radar measurements. *Bull. Amer. Meteor. Soc.*, **80,** 381-388.

Wakimoto, R. M., 1982: The life cycle of thunderstorm gust fronts as viewed with Doppler radar and rawinsonde data. *Mon. Wea. Rev.*, **110,** 1060-1082.

——, 2001: Convectively driven high wind events. *Severe Convective Storms, Meteor. Monogr.*, C. A. Doswell, Ed., Amer. Meteor. Soc., 255-298.

Wakimoto, R. M., and V. N. Bringi, 1988: Dual-polarization observations of microbursts associated with intense convection: The 20 July Storm during the MIST Project. *Mon. Wea. Rev.*, **116,** 1521-1539.

Wakimoto, R. M., and J. W. Wilson, 1989: Non-supercell tornadoes. *Mon. Wea. Rev.*, **117,** 1113-1140.

Wakimoto, R. M., C. J. Kessinger, and D. E. Kingsmill, 1994: Kinematic, thermodynamic, and visual structure of low-reflectivity microbursts. *Mon. Wea. Rev.*, **122,** 72-92.

Warning Decision Training Division, cited 2018: Radar and Applications Course. Office of Chief Learning Officer. [Available online at https://training.weather.gov/wdtd/courses/rac/documentation/rac18-all.pdf.]

Waterman, P. C., 1971: Symmetry, unitarity, and geometry in electromagnetic scattering. *Phys. Rev.*, **3,** 825-839.

Whiton, R. C., P. L. Smith, S. G. Bigler, K. E. Wilk, and A. C. Harbuck, 1998: History of operational use of weather radar by U.S. weather services. Part II: Development of operational Doppler weather radars. *Wea. Forecasting*, **13,** 244-252.

Wienhoff, Z. B., and Coauthors, 2018: Applications of a spatially variable advection correction technique for temporal correction of dual-Doppler analyses of tornadic supercells. *Mon. Wea. Rev.*, **146,** 2949-2971.

Wilson, J. W., and R. M. Wakimoto, 2001: The discovery of the downburst: T. T. Fujita's contribution. *Bull. Amer. Meteor. Soc.*, **82,** 49-62.

Wilson, J. W., R. D. Roberts, C. Kessinger, and J. McCarthy, 1984: Microburst wind structure and evaluation of Doppler radar for airport wind shear detection. *J. Climate Appl. Meteor.*, **23,** 898-915.

Wurman, J., K. Kosiba, P. Markowski, Y. Richardson, D. Dowell, and P. Robinson, 2010: Finescale single- and dual-doppler analysis of tornado intensification, maintenance, and dssipation in the Orleans, Nebraska, supercell. *Mon. Wea. Rev.*, **138,** 4439-4455.

Yoshikawa, E., V. Chandrasekar, and T. Ushio, 2014: Raindrop size distribution (DSD) retrieval for X-band dual-polarization radar. *J. Atmos. Oceanic Technol.*, **31,** 387-403.

Zhang, G., 2016: *Weather Radar Polarimetry.* CRC Press, 304 pp.

Zrnic, D. S., and A. V. Ryzhkov, 1999: Polarimetry for weather surveillance radars. *Bull. Amer. Meteor. Soc.*, **80,** 389-406.

Zrnić, D. S., 1987: Three-body scattering produces precipitation signature of special diagnostic value. *Radio Sci.*, **22,** 76-86.